Direct growth and characterization of graphene layers on insulating substrates

D I S S E R T A T I O N

zur Erlangung des akademischen Grades

Doctor rerum naturalium (Dr. rer. nat.)
im Fach Physik

eingereicht an der
Mathematisch-Naturwissenschaftlichen Fakultät I
Humboldt-Universität zu Berlin

von
Dipl.-Phys. Timo Schumann

Präsident der Humboldt-Universität zu Berlin:
Prof. Dr. Jan-Hendrik Olbertz

Dekan der Mathematisch-Naturwissenschaftlichen Fakultät I:
Prof. Dr. Stefan Hecht

Gutachter:
(i) Prof. Dr. Henning Riechert
(ii) Prof. Dr. Saskia Fischer
(iii) Prof. Dr. Dieter Weiss

eingereicht am: 04.03.2014
Tag der mündlichen Prüfung: 07.10.2014

'The science of today is the technology of tomorrow.'
Edward Teller

'Research is what I'm doing when I don't know what I'm doing.'
Wernher von Braun

Für meine Familie und meine Freunde.

Abstract

This thesis presents an investigation of graphene growth directly on insulating substrates. The graphene films are characterized using a variety of different techniques, including atomic force microscopy, Raman spectroscopy, and grazing-incidence X-ray diffraction. These allowed insight into the morphological, structural, and electrical properties of the graphene layers. Two different preparation methods were employed in this thesis.

The growth of epitaxial graphene on SiC(0001) by surface silicon depletion is presented first. An important parameter in this type of growth is the surface steps present on the SiC substrate. We show that the initial SiC surface step configuration has little influence on the growth process, and the resulting graphene layers. However, the surface steps do impact the magneto-transport properties of graphene on SiC, which is investigated closely and can be explained by a schematic model. The structure of the epitaxial graphene layers is also analyzed, including precise measurements of the lattice constants. Additionally, the growth of graphene on the C-face of SiC is systematically investigated.

Graphene films were also synthesized directly on insulating substrates using molecular beam epitaxy (MBE). This technique holds great potential for the well-controlled synthesis of graphene. With the accurate deposition rates and sub-monolayer thickness control, MBE allows for fundamental studies of the growth process. We demonstrate graphene growth on two different substrates, $(6\sqrt{3} \times 6\sqrt{3})$R30°–reconstructed SiC(0001) and Al_2O_3(0001). The dependence of the morphology and structural quality of the graphene samples on the growth parameters is evaluated and discussed. We find that graphene films grown by MBE consist of nanocrystalline graphene domains with lateral dimensions exceeding 30 nm. The structural quality of the graphene layers improves with increasing substrate temperature during growth. Finally, we show that the nanocrystalline domains of the graphene films possess an epitaxial relation to either substrate, and attribute an observed contraction of the in-plane graphene lattice constant to the presence of point-defects within the film.

Keywords: epitaxial graphene, MBE, QHE, SiC

Zusammenfassung

In dieser Arbeit wird das direkte Wachstum von Graphen auf isolierenden Substraten untersucht. Die hergestellten Schichten werden mittels verschiedener Methoden untersucht, unter anderem Rasterkraftmikroskopie, Ramanspektroskopie und Synchrotron-Röntgendiffraktometrie. Zwei verschiedene Synthetisierungsmethoden kommen hierbei zur Anwendung.

Zuerst wird das Wachstum von epitaktischem Graphen (EG) mittels thermischer Zersetzung von hexagonalen Siliciumcarbid–Oberflächen vorgestellt. Ein Fokus der Untersuchungen liegt hierbei auf den Stufen, welche auf der Substratoberfläche vorhanden sind. Wir zeigen, dass die initiale Oberflächenkonfiguration keinen unmittelbaren Einfluss auf den Wachstumsprozess und die entstehenden Graphenschichten besitzt. Die Stufen beeinflussen jedoch die elektrischen Transporteigenschaften im Quanten-Hall-Regime. Dieses Phänomen wird genauer untersucht und durch ein schematisches Modell erklärt. Die Struktur der epitaktischen Graphenschichten wird analysiert, inklusive präzieser Messungen der Gitterkonstanten. Anschließend werden systematische Untersuchungen über das Wachstum von EG auf Kohlenstoff-terminierten SiC-Oberflächen vorgestellt und diskutiert.

Als zweite Herstellungsmethode wird Molekularstrahlepitaxie (MBE) verwendet. Diese Technik besitzt großes Potential für das kontrollierte Wachstum von Graphen. Aufgrund der genau einstellbaren Depositionsraten und präziser Kontrolle der Schichtdicken, mit Genauigkeiten unter einer Monolage, ist MBE gut für fundamentale Wachstumsstudien geeignet. Wir demonstrieren Wachstum von Graphen auf zwei verschiedenen Substraten, $(6\sqrt{3} \times 6\sqrt{3})\mathrm{R}30^\circ$–rekonstruiertes SiC(0001) und Al_2O_3(0001) (Saphir). Die Abhängigkeit der Morphologie und der strukturellen Qualität der Proben von den Wachstumsbedingungen wird untersucht. Wir zeigen, dass die Graphenschichten aus nanokristallinen Domänen bestehen, deren laterale Abmessungen 30 nm überschreiten. Die strukturelle Qualität der Graphenschichten nimmt mit zunehmender Substrattemperatur zu. Schließlich wird gezeigen , dass die Graphendomänen eine epitaktische Beziehung zu ihrem jeweiligen Substrat besitzen und dass eine beobachtete Reduzierung der Gitterparameter durch die Existenz von Punktdefekten zu erklären ist.

Stichworte: epitaktisches Graphen, MBE, QHE, SiC

Publications

T. Schumann, T. Gotschke, F. Limbach, T. Stoica and R. Calarco, *Selective-area catalyst-free MBE growth of GaN nanowires using a patterned oxide layer*, Nanotechnology **22**, 9, 095603, (2011).

T. Gotschke, T. Schumann, F. Limbach, T. Stoica, and R. Calarco, *Influence of the adatom diffusion on selective growth of GaN nanowire regular arrays*, Appl. Phys. Lett. **98**, 10, 103102, (2011).

T. Schumann, T. Gotschke, F. Limbach, T. Stoica, and R. Calarco, *Cathodoluminescence spectroscopy on selectively grown GaN nanowires*, Proc. SPIE 7939, 793903 (2011).

M. H. Oliveira Jr., T. Schumann, M. Ramsteiner, J. M. J. Lopes, and H. Riechert, *Influence of the silicon carbide surface morphology on the epitaxial graphene formation*, Appl. Phys. Lett. **99**, 11, 111901 (2011).

T. Schumann, K.-J. Friedland, M. H. Oliveira Jr., A. Tahraoui, J. M. J. Lopes, and H. Riechert, *Anisotropic quantum Hall effect in epitaxial graphene on stepped SiC surfaces*, Phys. Rev. B. **85**, 23, 23502 (2012).

M. H. Oliveira Jr., T. Schumann, F. Fromm, R. Koch, M. Ostler, M. Ramsteiner, T. Seyller, J. M. J. Lopes, and H. Riechert, *Formation of high-quality quasi-free-standing bilayer graphene on SiC(0001) by oxygen intercalation upon annealing in air*, Carbon **52**, 83-89 (2013).

M. H. Oliveira Jr., T. Schumann, R. Gargallo-Caballero, F. Fromm, T. Seyller, M. Ramsteiner, A. Trampert, L. Geelhaar, J. M. J. Lopes, and H. Riechert, *Mono- and few-layer nanocrystalline graphene grown on Al_2O_3(0001) by molecular beam epitaxy*, Carbon **56**, 339-350 (2013).

P. Santos, T. Schumann, M. H. Oliveira Jr., J. M. J. Lopes, and H. Riechert, *Acousto-electric transport in epitaxial monolayer graphene on SiC*, Appl. Phys. Lett. **102**, 22, 221907 (2013).

T. Schumann, M. Dubslaff, M. H. Oliveira Jr., M. Hanke, F. Fromm, T. Seyller, L. Nemec, V. Blum, M. Scheffler, J. M. J. Lopes, and H. Riechert, *Structural investigation of nanocrystalline graphene grown on $(6\sqrt{3} \times 6\sqrt{3})$ R30°–reconstructed SiC surfaces by molecular beam epitaxy*, New J. Phys. **15**, 12, 123034 (2013).

T. Schumann, M. Dubslaff, M. H. Oliveira Jr., M. Hanke, J. M. J. Lopes, and H. Riechert, *Effect of buffer layer coupling on the lattice parameter of epitaxial graphene on SiC(0001)*, Phys. Rev. B **90**, 4, 041403(R) (2013).

J.M. Wofford, M.H. Oliveira, T. Schumann, B. Jenichen, M. Ramsteiner, U. Jahn, S. Fölsch, J.M.J. Lopes, H. Riechert, *Molecular beam epitaxy of graphene on ultra-smooth nickel: growth mode and substrate interactions*, New J. Phys. **16**, 093055, (2014).

Conference presentations

T. Schumann, T. Gotschke, T. Stoica, F. Limbach, and R. Calarco, *Selective MBE-growth of GaN nanowires on patterned substrates* (talk), Spring Meeting of the Deutsche Physikalische Gesellschaft (DPG), Regensburg, Germany, Mar. 2010

T. Schumann, M. H. Oliveira Jr., M. Ramsteiner, R. Hey, J. M. J. Lopes, L. Geelhaar, and H. Riechert, *Wachstum von nanokristallinem Graphen auf Saphir(0001) mittels Feststoffquellen-MBE* (talk), Deutscher MBE-Workshop 2011, Berlin, Germany, Okt. 2011

T. Schumann, K.-J. Friedland, M. H. Oliveira Jr., J. M. J. Lopes, and H. Riechert, *Anisotropic quantum Hall effect in graphene on stepped SiC(0001) surfaces* (talk), Spring Meeting of the Deutsche Physikalische Gesellschaft (DPG), Berlin, Germany, Mar. 2012

T. Schumann, K.-J. Friedland, M. H. Oliveira Jr., A. Tahraoui J. M. J. Lopes, and H. Riechert, *Anisotropic quantum Hall effect in graphene on stepped SiC(0001) surfaces* (talk), Graphene 2012, Brussels, Belgium, Apr. 2012

M. H. Oliveira Jr., T. Schumann, F. Fromm, R. Koch, M. Ostler, M. Ramsteiner, T. Seyller, J. M. J. Lopes, and H. Riechert, *Formation of high-quality quasi-free-standing bilayer graphene on SiC(0001) by oxygen intercalation upon annealing in air* (poster), Graphene Week 2012, Delft, Netherlands, Jun. 2012

T. Schumann, M. Dubslaff, M. H. Oliveira Jr., M. Hanke, F. Fromm, T. Seyller, J. M. J. Lopes, and H. Riechert, *Synthesis of graphene on* $(6\sqrt{3} \times 6\sqrt{3})R30^\circ$ *reconstructed SiC surfaces by molecular beam epitaxy* (talk), Spring Meeting of the Deutsche Physikalische Gesellschaft (DPG), Regensburg, Germany, Mar. 2013

T. Schumann, I. Shteinbuk M. H. Oliveira Jr., J. M. J. Lopes, and H. Riechert, *Synthesis of epitaxial graphene on C-face SiC: influence of growth conditions* (poster), Spring Meeting of the Deutsche Physikalische Gesellschaft (DPG), Regensburg, Germany, Mar. 2013

T. Schumann, M. Dubslaff, M. H. Oliveira Jr., M. Hanke, F. Fromm, T. Seyller, J. M. J. Lopes, and H. Riechert, *Synthesis of graphene on* $(6\sqrt{3} \times 6\sqrt{3})R30^\circ$ *reconstructed SiC surfaces by molecular beam epitaxy* (poster), Material Research Society (MRS) Spring Meeting, San Francisco, USA, Apr. 2013

T. Schumann, M. H. Oliveira Jr., R. Gragallo-Caballero, M. Dubslaff, M. Hanke, F. Fromm, T. Seyller, M. Ramsteiner, A. Trampert, L. Geelhaar, J. M. J. Lopes, and H. Riechert, *Direct growth of mono- and few-layer nanocrystalline graphene on* Al_2O_3*(0001) and SiC(0001) substrates by molecular beam epitaxy* (talk), Graphene Week 2013, Chemnitz, Germany, Jun. 2013

T. Schumann, M. H. Oliveira Jr., K.-J. Friedland, J. M. J. Lopes, and H. Riechert, *Influence of step edges in epitaxial graphene on quantum transport properties and their further utilization for the growth of graphene nanoribbons* (poster), 6th NTT-BRL school/International Symposium on Nanoscale Transport and Technology, Atsugi, Japan, Nov. 2013

Abbreviations

AFM	atomic force microscope/-microscopy
BL	'buffer layer', $\left(6\sqrt{3} \times 6\sqrt{3}\right)$R30°–reconstruction of hexagonal SiC(0001) surfaces
BLG	bilayer graphene
CVD	chemical vapor deposition
DFT	density functional theory
EG	epitaxial graphene
FWHM	full width at half maximum
GID	grazing incidence X-ray diffraction
GNR	graphene nano ribbon
HB	Hall bar
HOPG	highly oriented pyrolytic graphite
L_a	lateral size
LEED	low energy electron diffraction
LL	Landau level
MBE	molecular beam epitaxy
MLG	monolayer graphene
PDI	Paul-Drude-Institut für Festkörperelektronik
QFBLG	quasi-freestanding bilayer graphene
QHE	quantum Hall effect
QMS	quadropol mass spectrometer
RF	radio frequency
rlu	reciprocal lattice unit
RMS	root mean square
RSM	reciprocal space map
sccm	standard cubic centimeter per minute
SdH	Shubnikov-de Haas
TEM	transmission electron microscope/-microscopy
UHV	ultra-high vacuum
vdP	van-der-Pauw
vdW	van-der-Waals
XPS	X-ray photo electron spectroscopy

Contents

1. Introduction

In the last decades, micro- and nanoelectronics have reached tremendous importance for the modern world. To date, almost all devices are based on the silicon material system, and improvements were obtained by miniaturization and optimization in design. But Si technology has fundamental limits, when structures reach the dimensions of single atoms or molecules.[1] New materials may come to be used which are superior to Si in certain aspects, and may replace or supplement Si for specific applications. Graphene[2] is one promising candidate for future electronic applications due to its outstanding electrical properties; most prominently, its exceptionally high charge carrier mobilities.[3] Moreover, graphene gathered much attention for its versatility. Potential applications include: channel in field-effect transistors,[4] transparent conducting electrodes,[5] sensors,[6] photodetectors,[7] printable inks,[8] and nanoelectromechanical systems (NEMS).[9] Fundamental properties of graphene, some production methods, and potential applications are summarized later in this introduction.

In this work, the growth of graphene directly on insulating substrates is investigated, which may be compatible for future implementation in electronic devices. Two different techniques are employed. The first is growth of epitaxial graphene (EG) on hexagonal SiC by surface Si depletion. This method is already well established in research, and monolayers of graphene with high structural quality can be grown on the Si-face of SiC over large areas.[10,11] However, many questions still remain. This technique is explained in Chapter 3, and experimental results are presented and discussed. One area of emphasis is the impact of surface steps on the growth process and resulting transport properties. In Section 3.2, we analyze the influence of the initial surface step morphology on the growth and the resulting graphene. Subsequently, results from magnetotransport measurements in the quantum Hall regime are shown and discussed (Section 3.3). Grazing incidence X-ray diffraction (GID) measurements are presented in Section 3.4, which gives information about structural properties of graphene layers and allows for precise determination of lattice constants. Finally, after all previous experiments were conducted on graphene grown on Si-face SiC, the feasibility of growing graphene on the C-face is investigated with a systematic study of the influence of the growth parameters and synthesis environment on the morphology and structure of the layers.

The second part of this thesis examines the growth of graphene by molecular beam epitaxy (MBE) (Chapter 4). MBE is widely used in research for growing high-quality semiconductor films (such as nitrides, arsenides, or oxides) and heterostructures with precise thickness control and high structural quality. Two different substrates were employed: reconstructed SiC surfaces which enable quasi-homoepitaxial growth of graphene (Section 4.1), and $Al_2O_3(0001)$ (Section 4.2). We show that this technique is feasible for growing graphene films with a defined number of layers, and that the graphene possesses an epitaxial relation to the substrate. This may lead to direct growth of graphene based heterostructures in the future. The influence of the growth parameters on the resulting structural quality of the film is examined, and we show that the structural quality of the films can be improved by increasing the growth time and the substrate temperature. The films are characterized with a battery of different experimental methods, and the results

are discussed. Finally, the main findings of this work are summarized, and an outlook for future work is given in Chapter 5.

1.1. Graphene the 'wonder material'

Graphene is a single layer of sp^2-bonded carbon atoms arranged in a honeycomb lattice (see Fig. 1.1). It was the first truly 2-dimensional material which could be synthesized and isolated, and hence be deeply investigated. It is currently one of the most promising materials for future applications, as well as a fascinating system for fundamental research. In this introduction, basic properties of graphene are presented, and its potential applications are discussed.

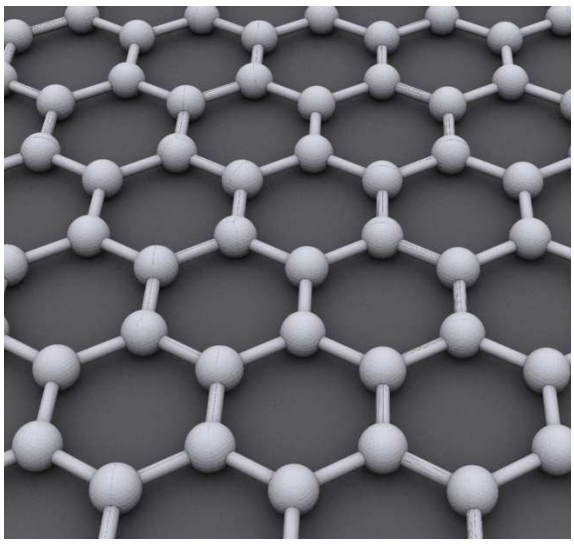

Figure 1.1: Schematic depiction of the honeycomb lattice structure of graphene. The figure was adapted from [12].

Before describing the properties of graphene, the historic development of graphene research will be briefly summarized.

The first theoretical description of single atom thick carbon layers was given in 1947 by Wallace *et al.*,[13] and isolated carbon sheets were first synthesized in 1962 by Boehm *et al.*[14]. They utilized thermal reduction of graphene oxide in solution to prepare one atom thick layers of carbon, but their discovery did not attract significant attention at the time. It was not until 40 years later that graphene became the focus of interest. In 2004, the research group of Andre Geim was the first able to isolate and investigate graphene layers[2,15]. The samples were prepared by the so-called 'exfoliation method' (see Section 1.3) and enabled electrical measurements on graphene flakes with sizes of several μm. For the development of this technique and their related research on graphene, Andre Geim and Konstantin Novoselov were awarded the Nobel Prize in Physics in 2010.

This relatively simple preparation method lead to a huge increase of interest, since research groups all over the world were now able to produce and investigate graphene samples. This high interest is also reflected by the number of scientific publications related to graphene research, as depicted in Fig. 1.2. Inspired by the extraordinary properties of graphene, new methods to produce the material were developed in the hope of enabling graphene to play an important role in future every-day applications. A summary of some synthesis methods is presented in Section 1.3.

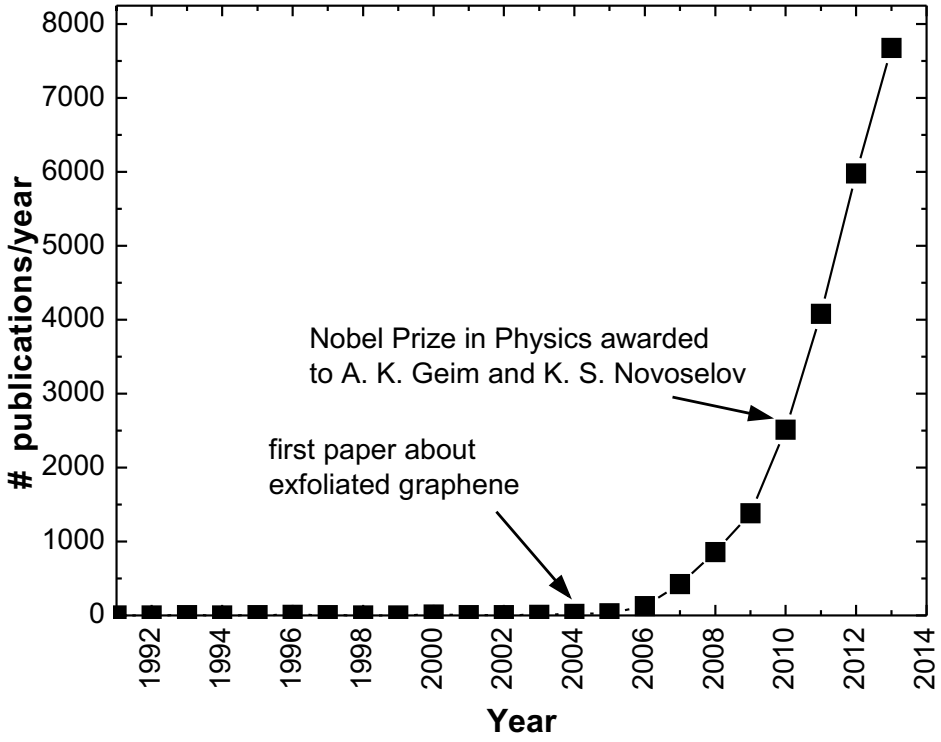

Figure 1.2: Number of publications (article, proceeding paper, review or letter) with the title containing 'graphene' per year. Source: Thomas Reuters *Web of Science*,[16] as of 21.02.2014.

1.2. Properties of graphene

In this section, some fundamental properties of graphene are presented. Since the research on graphene is so diverse, it is impossible to address every aspect in detail. The reader is thus referred to the mentioned references for additional information.

Graphene is a real two-dimensional, one atom thick crystal built of sp^2-hybridized carbon.[17] Its unit cell consists of two C atoms, arranged in a hexagonal honeycomb lattice [see Fig. 1.3 (a)]. The two atoms in the unit cell form the equivalent sublattices **A** and **B**. The two lattice vectors $\mathbf{a}_1$ and $\mathbf{a}_2$ can be written as[18]

$$\mathbf{a}_1 = \frac{a_{\text{C-C}}}{2}\begin{pmatrix}3\\ \sqrt{3}\end{pmatrix}, \mathbf{a}_2 = \frac{a_{\text{C-C}}}{2}\begin{pmatrix}3\\ -\sqrt{3}\end{pmatrix}, \tag{1.1}$$

where $a_{\text{C-C}}$ denotes the carbon–carbon bond length and is about 1.42 Å.[18] Theoretical calculations give a value for the length of the lattice vectors (and therefore the graphene's lattice constant) of about 2.461 Å,[19,20] which is the same as bulk graphite.[21]

The positions of the three nearest neighbors of each carbon atom are given by the vectors[18]

$$\boldsymbol{\delta}_1 = \frac{a_{\text{C-C}}}{2}\begin{pmatrix}1\\ \sqrt{3}\end{pmatrix}, \boldsymbol{\delta}_2 = \frac{a_{\text{C-C}}}{2}\begin{pmatrix}1\\ -\sqrt{3}\end{pmatrix}, \boldsymbol{\delta}_3 = -a_{\text{C-C}}\begin{pmatrix}1\\ 0\end{pmatrix}. \tag{1.2}$$

In a perfect graphene sheet, all carbon atoms are sp^2-hybridized, with three in-plane σ-orbitals and two out-of-plane π-orbitals, as depicted in Fig. 1.3 (b). This means that each

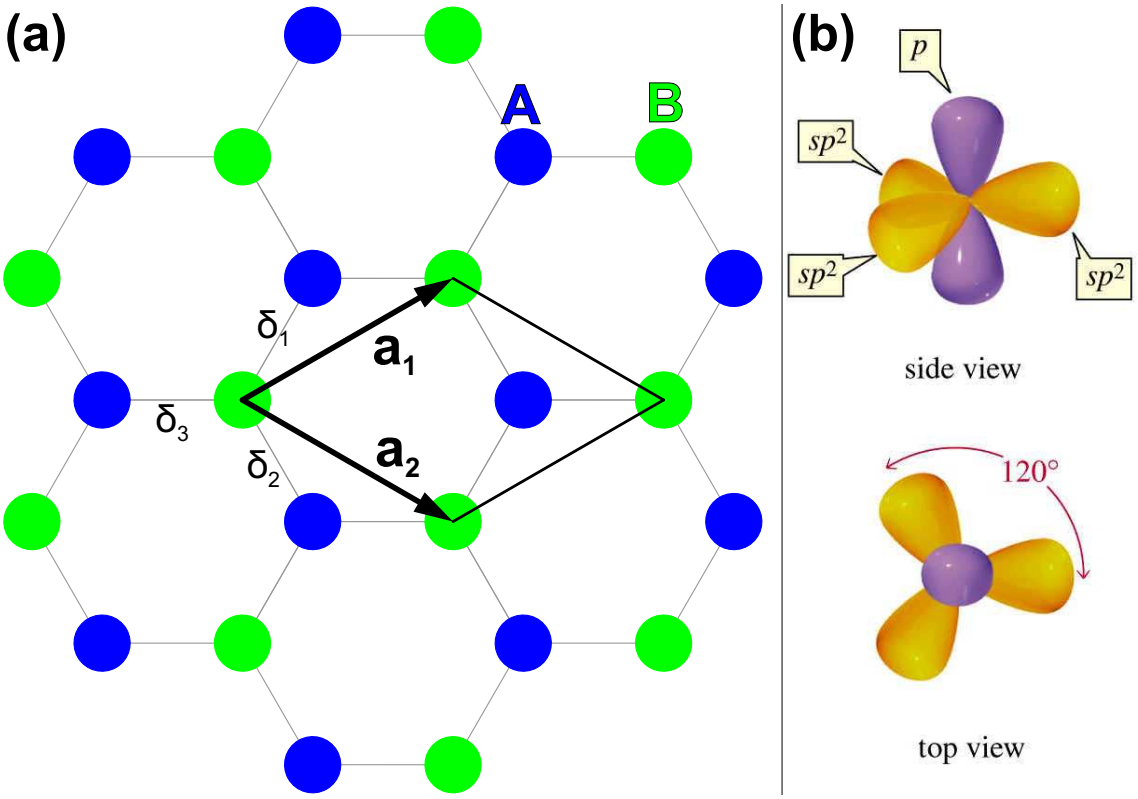

Figure 1.3: (a) Honeycomb lattice structure of graphene, $\mathbf{a_1}$ and $\mathbf{a_2}$ are the lattice unit vectors, and $\delta_{1,2,3}$ are the nearest-neighbor vectors. Atoms in the two different sublattices A and B are depicted in blue and green, respectively. (b) Structure of the sp^2 hybridization with three sp^2- (or σ-) orbitals and two p- (π-) orbitals. (b) was adapted from [24].

carbon atom can form equivalent σ-bonds to each of its three neighboring atoms. The bonding energy of one C-C bond in graphene amounts to 4.93 eV.[22]

These strong σ-bonds are responsible for the extraordinary mechanical properties of graphene. It possesses a breaking strength of $\sim$42 N m^{-1}, and second- and third-order elastic stiffnesses of 340 N m^{-1} and -690 N m^{-1}, respectively. These values correspond to a Young's modulus of E = 1.0·10^{12} Pa (= 1 TPa), third-order elastic stiffness of D = -2.0 TPa, and intrinsic strength of σ_{int} = 130 GPa.[23]

Not only its remarkable mechanical properties make graphene interesting for basic research, as well as for future industrial applications. Graphene also possesses extraordinary electronic properties, which will be presented in the following.

Since graphene possesses a hexagonal primitive unit cell, its Brillouin zone is also hexagonal. It is depicted in Fig. 1.4 (a). The band structure of monolayer graphene, as calculated by *ab initio* and tight-binding approaches, is shown in Fig. 1.4 (b). Detailed descriptions of the calculation methods can be found in References [18, 19, 25]. The K- and K′-points are of special interest, since the band gap is zero at these points, and the π- and π^*- bands touch. These points are also called 'Dirac points'. Fig. 1.4 (c) shows the respective band structure in a three dimensional representation, with a close-up in (d) of the energy bands close to one of the Dirac points.

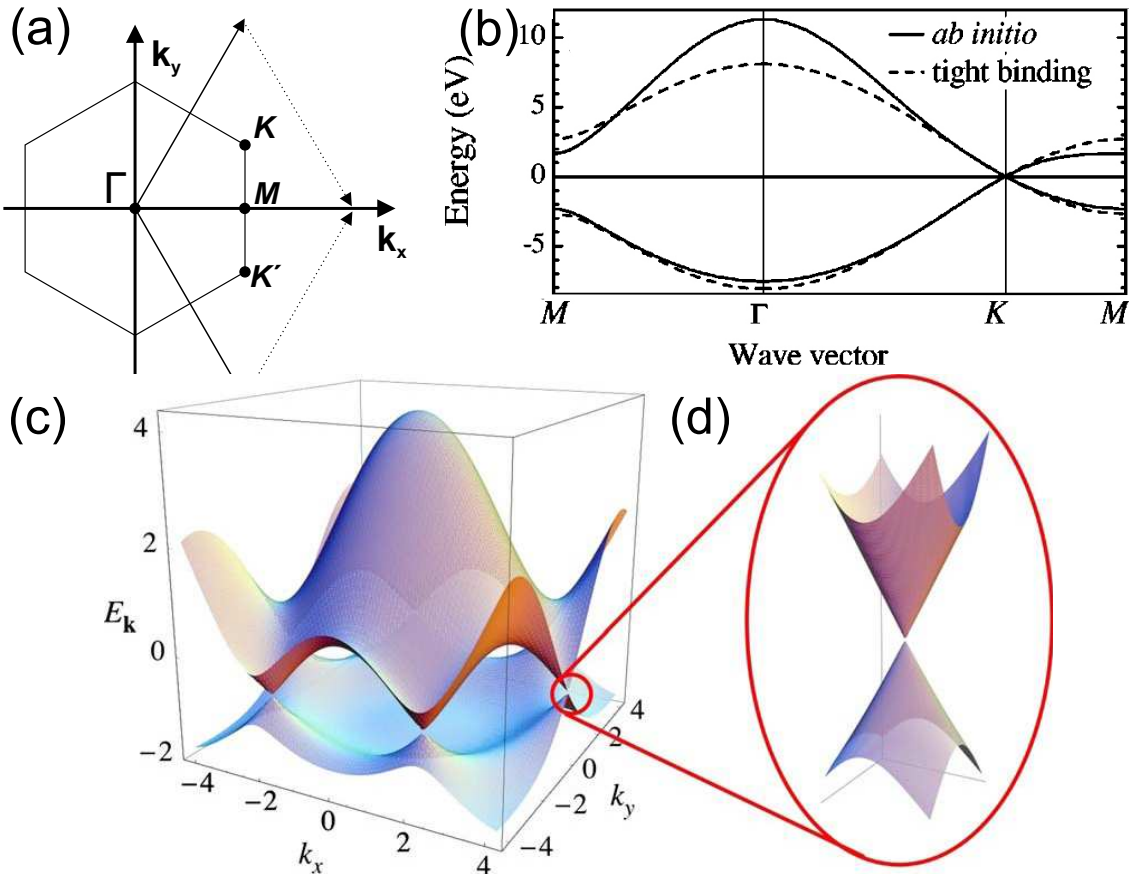

Figure 1.4: (a) First Brillouin zone of graphene, k_i denote the reciprocal lattice vectors, Γ, M, K, and K′ the high symmetry points. (b) *Ab initio* and tight binding calculation of the graphene π and π^* electronic bands (adapted from [19]). (c) Three dimensional representation of the π and π^* bands with (d) a zoom-in of the energy bands close to one of the Dirac points (taken from [18]).

In general, the energy bands of graphene can be expressed as:[13]

$$E_{\pm}(\mathbf{k}) = \pm t\sqrt{3 + f(\mathbf{k})} - t' f(\mathbf{k}), \tag{1.3}$$

with

$$f(\mathbf{k}) = 2\cos\left(\sqrt{3}k_y a\right) + 4\cos\left(\frac{\sqrt{3}}{2}k_y a\right)\cos\left(\frac{3}{2}k_x a\right), \tag{1.4}$$

with $t' \approx 0.1\,\mathrm{eV}$.[26] The plus sign applies to the upper π^*-band, the minus sign to the lower π-band.

In proximity of the **K** and **K′** points, the band structure can be simplified by an approximation. By setting **k** = **K**+**q** (with $\|\mathbf{q}\| \ll \|\mathbf{K}\|$), equation 1.3 can be expressed as[13]

$$E_{\pm}(\mathbf{q}) \approx \pm v_F \|\mathbf{q}\| + O[(\mathrm{q/K})^2]. \tag{1.5}$$

q describes here the momentum relative to the Dirac points and v_F the *Fermi velocity* ($v_F \approx 1.0 \times 10^6\,\mathrm{m/s}$).[27] This approximation leads to the situation that charge carriers close to the Dirac points possess the same energy dependence on their momentum as

relativistic massless Dirac particles, e.g. photons ($E_{\text{photon}} = c \cdot k$). Therefore, the charge carriers in monolayer graphene are often referred to as *Dirac fermions*. The charge carriers in graphene possess extraordinarily high intrinsic mobilities, up to 250 000 cm^2/Vs.[3,28] The highest measured mobilities exceed 40 000 cm^2/Vs, even at room temperature and under ambient conditions.[2,29–31] This property makes graphene an interesting candidate for future electronic applications.

A drawback for the implementation of graphene in today's semiconductor technology is its lack of a band gap, due to the touching of the π-bands. For that reason, graphene is often referred to as *zero band gap semiconductor*. The absence of a band gap is obstructive for its use in transistor devices, since the ratio between currents in ON and OFF states in graphene-based field-effect transistors is too low for logic operations.[32–34] Nevertheless, graphene transistors may be used in devices which do not require high ON/OFF ratios, but rather high-frequency operation, such as transistors for teraherz (THz) radiation emission and/or detection.[4,35]

This problem might be circumvented by utilizing bilayer graphene (BLG). By applying an electric field perpendicular to the BLG, a band gap opens in the BLG. The width of the band gap can be tuned by the strength of the electric field.[36–40]

In monolayer graphene a band-gap might also be opened by lifting the degeneracy of the two sublattices.[41] Theoretical calculations predict that this can be achieved by growing graphene on specific substrates, specifically hexagonal boron nitride (h-BN).[42]

Another possible way to introduce a band gap is to pattern graphene into narrow stripes. Graphene nano ribbons (GNR) with widths in the region of a few nano meters, possess a band gap, which increases with decreasing GNR width. This effect is due to charge carrier confinement. More information on GNRs can be found e.g. in References [43–47]

Additional information and more extensive details on the extraordinary electrical properties of MLG are given in References [18, 48, 49]. For this thesis, electrical measurements on graphene in the quantum Hall regime were conducted. Details on the anomalous integer quantum Hall effect are provided in Section 3.3.

Graphene possesses even more intriguing properties. Comprehensive reviews regarding graphene can be found in References [18, 50–53].

1.3. Preparation methods

In this section, some of the most common preparation methods will be presented, including their advantages and disadvantages. Due to the large variety, the techniques will only be shortly summarized, more detailed information can be found in the references in the respective sections. The main focus lies on methods which allow the preparation of large-area graphene layers. Further methods – e.g. synthesis of graphene flakes in solution – will not be listed, since the main focus of this work lies in the preparation of graphene which might have usability for electronic devices. Additionally, the exfoliation method is described, since it was the technique which first allowed investigation of single graphene sheets on a substrate.

Exfoliation of graphene

Exfoliation was the first technique used to produce high-quality monolayers of graphene and place them on a substrate. *Highly oriented pyrolytic graphite* (HOPG) is usually used as the source material. A strip of adhesive tape[a] is pressed against the block of HOPG, so that thin layers of graphite are released from the HOPG. By repeated folding the tape, the layers are cleaved several additional times, and eventually pressed onto a oxidized silicon wafer. Some flakes remain on the substrate after peeling of the tape and can thus further be investigated. Monolayer flakes can be identified by means of optical or scanning electron microscopy. This method was developed by the group of Andre Geim *et al.*[2] A video in which the preparation is shown can be found in Reference [54].

This method spread quickly in the scientific community since it is comparatively easy to learn and no expensive equipment is required. Graphene flakes with near-perfect structural quality and high carrier mobilities can be produced, however their sizes are limited to the order of few µm.[2] These samples are best suited for basic research, albeit other synthetization methods are needed for the production of large-area graphene for industrial applications.

Chemical vapor deposition on metals

Chemical vapor deposition (CVD) offers another route to produce graphene of reasonably high structural quality on large area substrates.[55] Common metals for the use as substrate are Cu,[56,57] Ni,[58] Pt,[59] Pd,[60] Ru,[61] or Ir.[62] Advantages of the CVD method include its wide use in research and industry, as well as the relatively fast growth rates (order of minutes for monolayer graphene). The structural quality of the resulting monolayer graphene layers can be high when growth is under optimized conditions. However, the growth of continuous few-layer graphene has not yet been demonstrated. This is due to the employment of metal as a substrate, which assist the graphene growth. The metal has a catalytic influence and helps to crack the precursor molecules, though after the growth of the first layer of graphene the metallic substrate is covered. Besides, a post-synthesis transfer step to a (semi-)insulating substrate is required in order to perform electrical measurements or for application purposes. This transfer may degrade the electronic properties of the material, possibly limiting its technological application.

Recently, it has been demonstrated that CVD can also be used to grow graphene directly on non-metallic substrates.[63] However, a high substrate temperature (1400 °C)

[a] The first experiments were performed with tape from the company '*Scotch*', hence this method is commonly referred to as '*Scotch tape method*'.

had to be employed in this process, which is not compatible with standard silicon technology.

Epitaxial growth of graphene by silicon surface depletion of SiC

Surface silicon depletion of SiC substrates is a promising route to produce graphene over large-areas with high structural quality directly on an insulating substrate.[10] For this method, SiC – usually the hexagonal 4H- or 6H-polytype – is annealed at a high temperature in vacuum,[10] or in an Argon[11] or disilane[64] atmosphere. Due to their higher vapor pressure, the Si atoms evaporate at a lower temperature then the C atoms, leaving behind a carbon rich surface.[65] As a first step, a $\left(6\sqrt{3} \times 6\sqrt{3}\right)\mathrm{R}30^\circ$ surface reconstruction is formed, also known as *buffer layer* (BL).[66] This BL is principally isomorphic to graphene, i.e. it possesses the same honeycomb lattice structure and a similar lattice constant (see detailed investigation in Section 4.1). However, about 1/3 of its carbon atoms are covalently bond to the SiC substrate. By continuing the heating, more Si atoms leave the surface and a 'new' BL forms under the first one. The already existing BL decouples from the substrate and hence turns into a graphene layer.

A disadvantage of this technique is that it is limited to SiC as the substrate material. SiC wafers are quite costly at the moment, and are not widely used in current semiconductor technology.

This technique is used in this thesis, and a more detailed description is given in Section 2.1 and Chapter 3.

Molecular beam epitaxy

Molecular beam epitaxy is a technique which is widely used in materials research. It offers the possibilty to synthesize a variety of materials (e.g. III-V semiconductors) on a large variety of templates, and at moderate temperatures (<1000 °C).[67] MBE shows potential to overcome some drawbacks of the methods described above. One of its main advantages is thickness control, which in the context of graphene might enable the precise growth of not only mono- but also few-layer graphene films, as well as the direct growth of heterostructures. Since atomic species are used as the precursor, metallic substrates are not a mandatory requirement, and other technologically relevant substrates may be used. Another advantage of MBE is that *in-situ* methods may be used to directly monitor the films during growth.

This technique is employed in this thesis and will be further described in Section 2.2, while the results of graphene growth by MBE will be presented in Chapter 4.

1.4. Potential applications of graphene

Graphene possesses several different potential applications; a non-exhaustive list will be presented here.

The high strength of graphene can be used for the development of lighter and stronger materials[68] or composites.[69] Notably, a tennis racket, containing graphene attracted public interest.[70] It is also possible to produce free-standing graphene membranes, which can be employed as mechanical oscillators in nanoelectromechanical systems.[9,71]

One layer of graphene absorbs about 2.3% of light in the visible range.[72] Together with its high electrical conductivity and robustness, it may serve as a transparent electrode,[5] such as for touchscreen applications or in solar cells.

Additional applications and a good review can be found in Reference [52]. Tables 1.1, and 1.2 were taken from this publication, and summarize requirements on the material for different electronic and photonic applications.

Application	Drivers	Issues to be addressed
Touch screen	Graphene has better endurance than benchmark materials	Requires better control of contact resistance, and the sheet resistance needs to be reduced (possibly by doping)
E-paper	High transmittance of monolayer graphene could provide visibility	Requires better control of contact resistance
Foldable OLED	Graphene of high electronic quality has a bendability of below 5 mm, improved efficiency due to graphene's work function tunability, and the atomically flat surface of graphene helps to avoid electrical shorts and leakage current	Requires better control of contact resistance, the sheet resistance needs to be reduced, and conformal coverage of three-dimensional structures is needed
High-frequency transistor	No manufacturable solution for InP high-electron-mobility transistor (low noise) after 2021, according to the 2011 ITRS	Need to achieve current saturation, and fT5850 GHz, $f_{\max}$ / 1200 GHz should be achieved
Logic transistor	High mobility	New structures need to resolve the bandgap-mobility trade-off and an on/off ratio larger than 10^6 needs to be achieved

Table 1.1: Electronics applications of graphene, adapted from [52].

Application	Drivers	Issues to be addressed
Tunable fibre mode-locked laser	Graphene's wide spectral range	Requires a cost-effective graphene-transferring technology
Solid-state mode-locked laser	Graphene-saturable absorber would be cheaper and easy to integrate into the laser system	Requires a cost-effective graphene-transferring technology
Photodetector	Graphene can supply bandwidth per wavelength of 640 GHz for chip-to-chip or intrachip communications (not possible with IV or III-V detectors)	Need to increase responsivity, which might require a new structure and/or doping control, and the modulator bandwidth must follow suit
Polarization controller	Current polarization controlling devices are bulky or difficult to integrate but graphene is compact and easy to integrate with Si	Need to gain full control of parameters of high-quality graphene
Optical modulator	Graphene could increase operating speed (Si operation bandwidth is currently limited to about 50 GHz), thus avoiding the use of complicated III-V epitaxial growth or bonding on Si	High-quality graphene with low sheet resistance is needed to increase bandwidth to over 100 GHz
Isolator	Graphene can provide both integrated and compact isolators on a Si substrate, dramatically aiding miniaturization	Decreasing magnetic field strength and optimization of process architecture are important for the products
Passively mode-locked semiconductor laser	Core-to-core and core-to-memory bandwidth increase requires a dense wavelength-division-multiplexing optical interconnect (which a graphene-saturable absorber can provide) with over 50 wavelengths, not achievable with a laser array	Competing technologies are actively mode-locked semiconductor lasers or external mode-lock lasers but the graphene market will open in the 2020s; however, interconnect architecture needs to consume low power

Table 1.2: Possible photonic applications of graphene, adapted from [52].

2. Experimental details

In this chapter, details of the experimental methods employed in this thesis are briefly presented. Additional information on the methods can be found in the references provided.

2.1. Epitaxial graphene formation by surface Si depletion of SiC

This section presents the furnace which is used to produce epitaxial graphene on silicon carbide by surface Si depletion. A schematic is depicted in Fig. 2.1.

The furnace consists of a quartz tube wherein the graphite crucible is located, which holds the SiC substrate. The crucible is held in the middle of the quartz tube by a block of graphite fibers, which also acts as thermal insulation between the high-temperature graphite crucible and the walls of the quartz tube. The graphite crucible is inductively heated by a radio-frequency (RF) coil, positioned around the tube. A heating power of up to $\sim$12 kW is provided by the power supply, which allows heating ramps of $\sim 8\,^{\circ}\mathrm{C/s}$. To avoid these high temperatures from damaging of the tube, two ventilators cool it at the position of the RF-coil. A pyrometer measures the crucible temperature and is pointed to a hole in one site of the crucible. Via a PID control unit, the pyrometer adjusts the output level of the power supply and hence the temperature and ramps of the crucible.

Two different pumps are connected to the reactor; a turbo molecular pump for high-vacuum processes ($\sim 10^{-5}$ mbar) and a membrane pump for reaching a rough vacuum and for higher pressure processes. The membrane pump is connected to the reactor via a control valve, which adjust the pressure inside the quartz tube when a constant inflow of gas is provided. Different gases can be flushed through the reactor, including pure

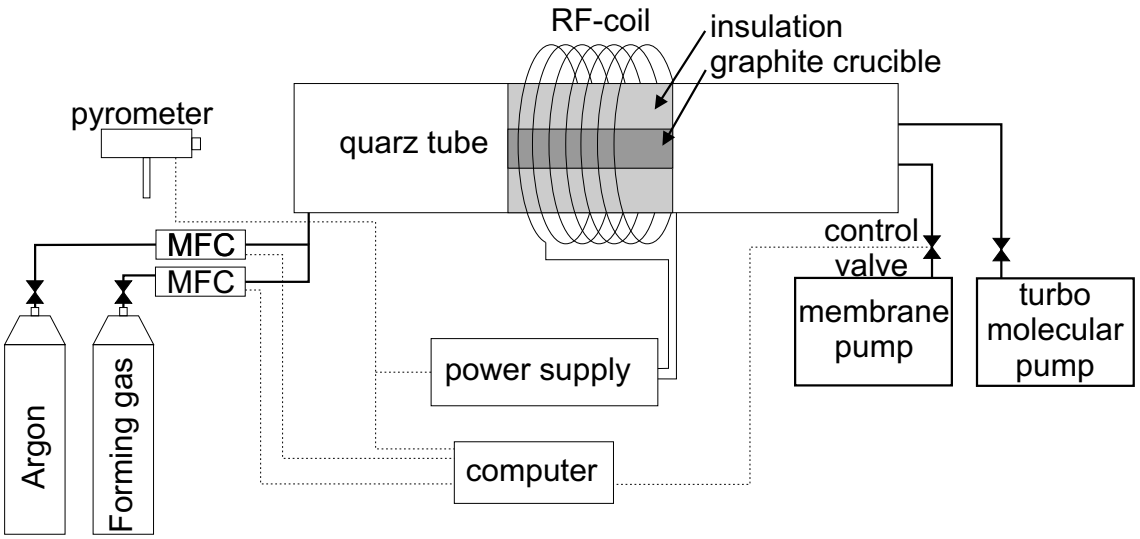

Figure 2.1: Schematic of the furnace used for the synthesis of epitaxial graphene on SiC.

argon and forming gas (FG, 5 at. % H_2 and 95 at. % Ar). The gas fluxes are individually controlled by mass flow controllers (MFC). An additional gas line is connected with the reactor to allow fast venting with nitrogen, which is needed for loading/unloading a sample from the furnace.

All components of the system can be controlled via a computer program (as indicated by the dotted lines in Fig. 2.1). Additional control units which communicate with the actual measuring devices are not depicted in the figure for better visibility. The furnace was designed similar to the system of Prof. Thomas Seyller,[73] who generously provided information for constructing the system.

The typical procedure for preparing epitaxial, monolayer graphene on SiC(0001) is as follows (chemical reactions and the physical background of the synthesis is described in Section 3.1).

The first step is an etching process of the SiC. The chemically cleaned SiC substrates are put in the crucible and loaded into the quartz tube, which is pumped down until a pressure of $\sim 10^{-5}$ mbar is reached. It is then heated up to 800 °C for 15 min to desorb any contaminants from the surface. Subsequently, the reactor is filled with Ar. The Ar flux is held at a constant value by the corresponding gas flow controller. When the process pressure is reached (usually 900 mbar), the control valve adjusts to keep the pressure constant. In the next step, the temperature is increased to the desired process temperature and held there. As soon as the temperature reaches the process value, the flux of Ar is stopped and is replaced by a flux of FG. After the process is finished, heating stops, the flux of FG is turned to zero, a flux of Ar is established, and the reactor cools down. When it reaches room temperature, the control valve closes, the Ar flow stops, the reactor is flushed with N_2 until ambient pressure is reached, and the sample is unloaded.

Before the next step (graphitization by surface Si depletion) starts, the reactor and crucible need to be cleaned. This is achieved by annealing the crucible to 1600 °C for one hour, where the heating is performed partly under vacuum conditions, and partly in an Ar atmosphere.

For the graphene synthesis, the first steps are identical to the ones performed in the H-etching process, but only Ar and no FG is used. After degassing the sample and filling the reactor with Ar, the temperature is again increased to the desired process temperature (usually 1600 °C) and held there until the process is finished. The sample then cools down to room temperature under continuous Ar flux, and can be unloaded for further investigations.

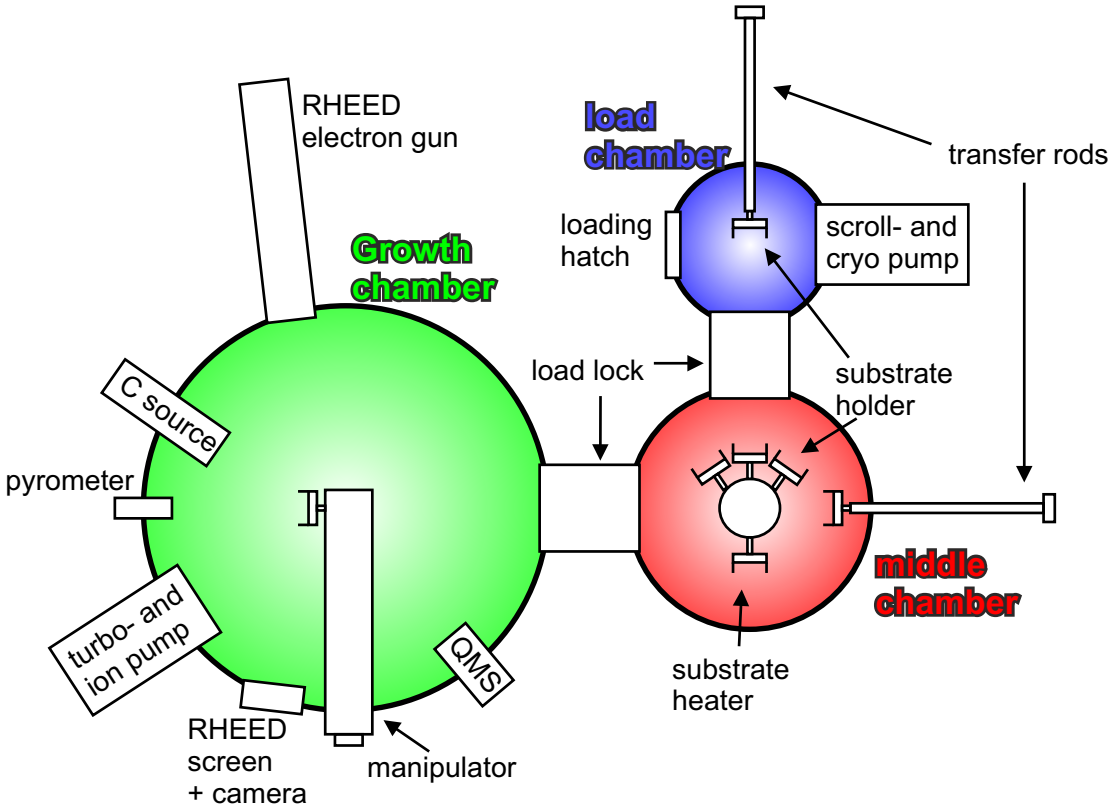

Figure 2.2: Schematic of the employed MBE machine. For better visibility, not all the installed equipment is depicted.

2.2. Molecular beam epitaxy

Molecular beam epitaxy (MBE) is a well established method for the production of epitaxial layers with high purity and high crystalline quality, using directed beams of atomic or molecular species in ultra high vacuum (UHV). In this section, the MBE machine employed and its equipment are briefly described, as well as the standard procedure to grow graphene films. Further general information on this method can be found in References [74–76].

The MBE machine used for this work was manufactured by *Meca 2000*. A schematic is shown in Fig. 2.2, note that only the components relevant for this work are depicted. Additional parts, such as effusion cells, ion sputtering components, or a plasma source, are not shown for the sake of simplicity. Fundamentally, the MBE consists of three separated chambers: the loading chamber, the middle chamber in which samples can be stored and outgassed, and the growth chamber where the actual deposition process takes place.

Prior to the growth, the substrate is chemically cleaned in n-butyl acetate, acetone and isopropanol under ultrasonication to remove any dirt or organic residues from the surface. A 1 µm thick layer of titanium is deposited on the backside of the substrate by sputtering to enable non-contact, radiative heating. The sample is then mounted in the load chamber, which is closed and pumped to a rough vacuum ($\sim 10^{-2}$ mbar) by a scroll pump. Subsequently, the load chamber is further pumped with a cryopump for approximately 20 minutes until a pressure in the order of 10^{-8} mbar is reached, allowing the sam-

ple to be transfered to the middle chamber. The middle chamber is equipped with three sample holders, which are used to store samples in vacuum, and one heatable holder. The sample is transferred to the heated holder and annealed at 350 °C for 30 min to desorb water (originating from atmospheric humidity) from the sample. The middle chamber is pumped via an ion pump, and the base pressure is in the order of $10^{-9} - 10^{-10}$ mbar.

After the sample is outgassed in the middle chamber, it is transferred to the growth chamber and attached to the manipulator. The manipulator was manufactured by *Createc*,[77] and is able to heat substrates via non-contact radiative heating. Substrate temperatures of up to 1200 °C can be reached with this apparatus. The manipulator can be rotated to orient the sample in transfer position (facing the load lock) or in growth position (facing the carbon source). The temperature of the substrate surface is measured by a pyrometer, which faces the sample in growth position.

As the source for the carbon flux we use the *SUKO* solid carbon source, from the company *MBE Komponenten GmbH*.[78] The cell consist of a resistively-heated HOPG filament. The filament reaches temperatures up to 2300 °C, which is sufficient for carbon atoms to sublimate from it. The resulting beam of C atoms can be blocked by a mechanical shutter, which allows exact control of the growth time. The source emits primarily atomic carbon, as confirmed by a quadrupole mass spectrometer (QMS),[79]. The QMS is one of two *in-situ* analysis methods installed in this MBE system. It measures the mass and pressure of the species present in the growth chamber. The second *in-situ* analysis method is a reflective high energy electron diffraction (RHEED) system. Unfortunately, this technique appeared to be unsuitable for monitoring the growth for the samples investigated in this thesis. Therefore I omit any further descriptions of this technique.

Two different pumps are installed at the growth chamber: a turbo-molecular pump, and an ion pump. To further improve the vacuum level in the chamber during growth, it is equipped with a cryo shield. This shield is flushed with liquid nitrogen during growth. Therefore, atoms or molecules present in the chamber which impinge on the walls are likely to condense and stick there, further improving the vacuum. The base pressure in the (cold) growth chamber is in the order of 10^{-11} mbar. During the growth process, sections of the chamber heat up considerably due to the high temperatures of the carbon source and manipulator. This results in a pressure increase to $10^{-8} - 10^{-9}$ mbar during growth.

After the growth is finished, the manipulator cools down and the sample is either stored in the middle chamber or transferred to the load chamber and unloaded for further *ex-situ* analysis.

2.3. Raman spectroscopy

Raman spectroscopy is a powerful and widely used tool for investigating samples with a non-contact, non-destructive method. The basic concept of Raman spectroscopy will be presented in this section, followed by a more detailed discussion on its use in graphene research. More information regarding this technique, and especially for its employment in graphene research, can be found in References [80–85].

The Raman effect[86] is an interaction between electro-magnetic waves (photons) and matter, in which a lattice vibration (phonon) is excited (Stokes scattering) or annihilated (anti-Stokes scattering). When acquiring a Raman spectrum, the sample is illuminated with monochromatic light, and the reflected light is detected. The majority of the reflected photons have undergone elastic scattering (Rayleigh scattering) and therefore possess the same wavelength (or energy) as the incident light. A small fraction of the photons is inelastically scattered, and thus possess an different energy than the incident photons. This difference in energy corresponds to the energy of a lattice vibration (phonon) which either has been excited or annihilated. Therefore, it is possible to gain insight into the energy of the phonon spectrum of the investigated sample. Especially for the investigation of graphene, Raman spectroscopy also gives insight into other properties, such as defects,[81,87] strain,[88–90] or charge carrier concentration.[91]

Graphene possesses different fundamental phonon modes. Only those modes which are Raman active are thus observed and relevant in experiments conducted for this thesis, will be discussed at this point. Fig. 2.3 (a) displays a representative Raman spectrum of pristine (defect-free) graphene. The spectrum is dominated by the so-called G-line at $\sim$1590 cm^{-1}, and the double-resonant 2D-line at $\sim$2700 cm^{-1}.

Fig. 2.3 (b) shows a Raman spectrum of defective graphene. The appearance drastically changes in comparison to the spectrum of pristine graphene, including the addition of

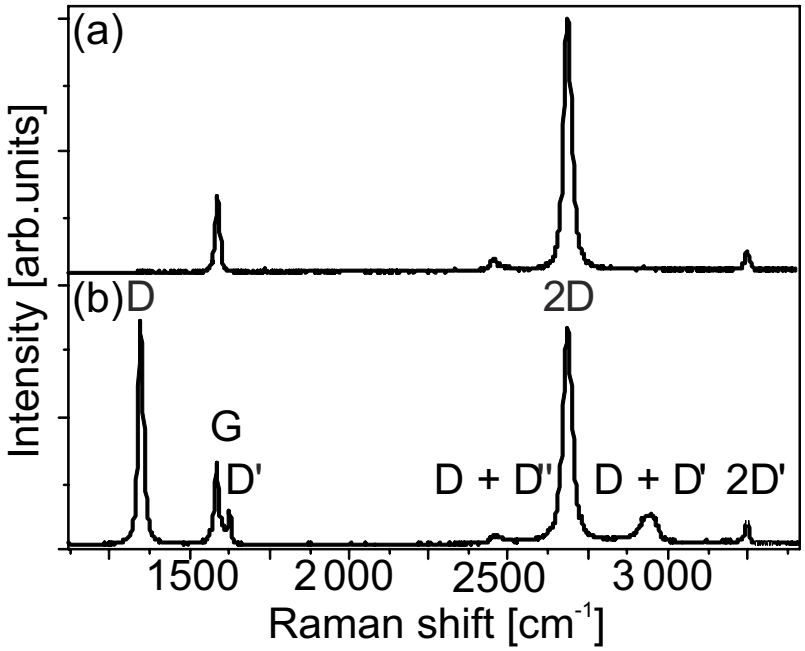

Figure 2.3: Raman spectra of (a) pristine and (b) defective monolayer graphene. The figure was adapted from [85].

new peaks. Only the G- and 2D-lines, and the defect-induced D- and D′-lines will be discussed here, more detailed treatments can be found in the references cited above.

The G-peak corresponds to the double-degenerate iTO (transversal optical) and LO (longitudinal optical) phonon mode (E_{2g} symmetry) at the center of the Brillouin zone, **Γ**.[84] A real-space depiction of this lattice vibration is shown in Fig. 2.4 (a) and it is illustrated in K-space in Fig. 2.4 (b). This fundamental mode appears in all Raman spectra from materials which contain sp^2-hybridized carbon.

The D-line is a consequence of interaction between electrons, phonons and the electronic band structure of graphene. It is schematically depicted in Fig. 2.4 (d). The incoming photon excites an electron near the Dirac point, which is then inelastically scattered by a phonon from the Dirac point **K** to **K'**. The backscattering of electrons is an elastic

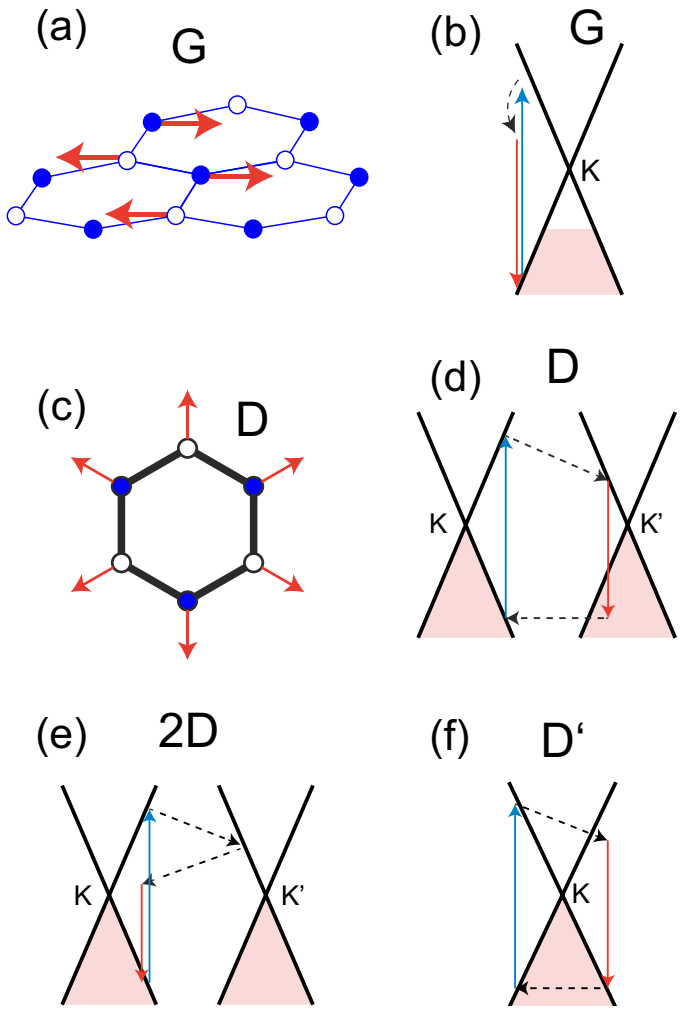

Figure 2.4: Schematic depictions of the processes of some Raman active modes in graphene. (a) Lattice vibration of the G mode in real space, and (b) the same process in k-space. (c) Atom displacement of the D mode in real space, and (d) schematic process in k-space. (e) Double resonant scattering process of the 2D mode, depicted in k-space, and (f) the process leading to the D′-peak. Note that for (d)–(e), different possibilities in the order of the scattering processes exist (e.g. excitation – defect scattering – phonon scattering – relaxation). Only one possibility is depicted here, for all combinations see Fig. 2 in Reference [85].

scattering process which requires a defect in the graphene lattice. In real space, the lattice vibration associated with the D-line is described as a 'breathing mode' of the hexagonal carbon ring [see Fig. 2.4 (c)]. In both depictions (real- and reciprocal-space) it is readily apparent, that the existence of a D-peak in a Raman spectrum requires the presence of defects and/or boundaries of graphene domains.

The same is not true for the overtone of the D-peak, the 2D-peak. In the case of the 2D-peak, both scattering events are inelastic and involve phonons, from the **K** to the **K'** point and back. The energy shift linked with the 2D mode is roughly twice that of the D mode. This is a double-resonant process, since the energy of the incident light (in the visible range) can match the energetic difference between the valence and the conduction band near **K**. Also, since this mode relies on the presence of the Dirac cones at the **K** point, it can be taken as a fingerprint of monolayer graphene.

Since the 2D-peak originates from interactions of electrons and phonons with the electronic band structure of graphene, the shape of the 2D-peak reflects any changes in the band structure. This is especially the case if the film does not consist of monolayer gra-

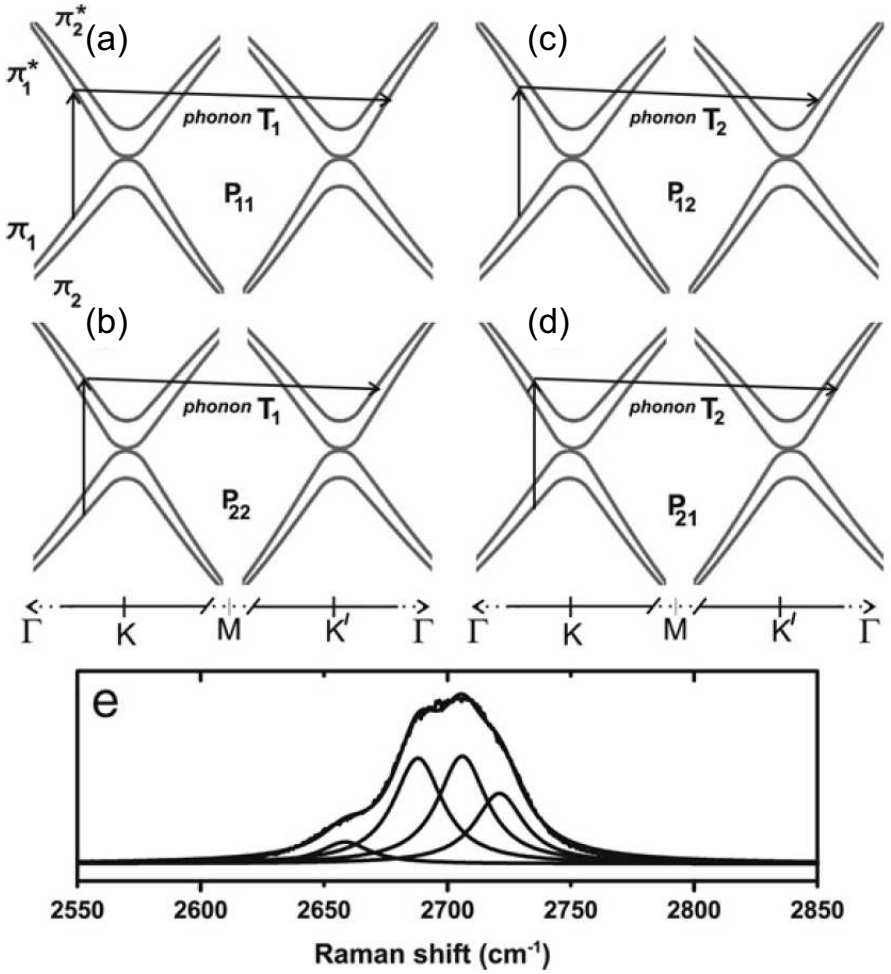

Figure 2.5: Schematic view of the electron dispersion of bilayer graphene (BLG) near the **K** and **K'** points. The four double resonant processes are indicated: (a) P_{11}, (b) P_{22}, (c) P_{12}, and (d) P_{21}. (e) The measured Raman 2D-peak of bilayer graphene for 2.41 eV laser energy, consisting of four Lorentzians. The figure was reproduced from [84].

phene, but rather bilayer graphene (BLG). In case of BLG, the band structure at the **K**-points changes from single Dirac cones, splitting into double parabolic bands π_1 and π_2. π_1 and $\pi_1^\star$ touch at the **K**-points, as shown in Fig. 2.5, making BLG also a zero-band-gap semiconductor. Due to the double bands, four different double resonant processes exist, labeled P_{ij}, as indicated in Fig. 2.5 (a)–(d). 'i' and 'j' denote the respective π-band at **K** and **K**′ from (or to) which the electrons are scattered. The phonons involved in each of the four different processes possess slightly different energies, hence the resulting 2D-peak is composed of four separated Lorentzians.

The D′ mode can be regarded as an analogue of the D mode, but instead of scattering an electron from one Dirac cone to another, it is scattered within the same Dirac cone [see Fig. 2.4 (d)]. A double resonant 2D′-line also exists at higher wavenumbers, with an analogous origin as the 2D-mode.

As mentioned above, information about the structural quality of graphene can be obtained from its Raman spectra. The D-peak, as well as the D′-peak, are indications for a defective graphene film. These may be point defects (vacancies, sp^3-hybridized C, or impurity atoms) or one-dimensional defects (e.g. grain boundaries or line dislocations). The average domain size of a polycrystalline graphene film can be deduced from the (integrated) intensity ratios I_D/I_G and $I_{D'}/I_G$. The ratios are proportional to the inverse of the graphene domain size.[92,93] The size of the crystalline domains can be estimated, from both the D- and D′-peaks, using the empirical relation:

$$L_a(\mathrm{nm}) = \frac{C}{E_l^4}\left(\frac{I}{I_G}\right)^{-1}, \tag{2.1}$$

where I denotes the D or D′-peak intensity, E_l the excitation laser energy (in eV) and C is an empirically determined constant that assumes the value of 560 for the D-peak, and 160 for D′-peak. This method is imperfect, and can yield a discrepancy in the values of L_a if the intensity ratios do not obey following relation:[94]

$$\frac{I_D}{I_{D'}} = \frac{I_D}{I_G}\frac{I_G}{I_{D'}} = \frac{560}{160} = 3.5. \tag{2.2}$$

As shown by Venezuela *et al.*[95] and Eckmann *et al.*,[87] this ratio depends on the kind of defect responsible for activation of the modes. For several of the samples investigated in this thesis (see Chapter 4), this requirement is not fulfilled and the sizes of L_a calculated with different methods vary considerably. Since the model on which Equation 2.1 relies only takes into account grain boundaries as defects, the values obtained by this equation yields a lower limit for the actual graphene domain sizes.

The widths of the peaks (usually given as 'full width at half maximum', FWHM) are also a benchmark for the quality of a graphene film. Several factors may contribute to the broadening of the Raman peaks, such as crystalline domain size, point defects, disorder, inhomogeneous strain, and/or doping. Particularly, one can employ the width of the peaks of the different Raman modes to calculate the domain sizes, L_a, using an alternative method.[93] When the graphene domain is smaller than the phonon mean free path, the lifetime, τ, of phonons is inversely proportional to the domain size. Since the FWHM values are determined by τ (i.e. FWHM$\propto 1/\tau$), there is proportionality between the

FWHM and the domain size. The width of the Raman peaks can in this case be written as:

$$\mathrm{FWHM} = A + \frac{B}{L_a}, \tag{2.3}$$

where L_a is again the average domain size and the empirical constants A and B assume different values depending on the peak used for the calculations.[93] This model also only takes grain boundaries into account, and therefore also yields a lower limit for L_a.

In this work, all Raman spectra were recorded with a commercial system by the company *Horiba / Jobin-Yvon*. The 482.4 nm line (2.81 eV) of a Kr^+ ion laser by the company *Coherent* was employed as light source. The laser spot is focused at the sample surface via microscope optics, with a spot size of about 1 µm.

2.4. Electrical characterization

To gain insight on the electrical properties, such as charge carrier density and -mobility, electrical measurements were performed on the graphene films. In this work, the charge carrier type, density, and mobility of graphene samples were investigated via magneto-transport measurements. Two different sample layouts were employed: patterning the graphene into Hall bar structures, or measuring the unpatterned sample in van-der-Pauw (vdP) geometry.[96] Both techniques rely on the Hall effect,[97] which is described in Appendix A (together with the quantum Hall effect).

VdP measurements are conducted in an apparatus which consists of a small electromagnet, which can create magnetic fields of up to 1 T. Samples can be cooled with liquid nitrogen, and thus measurements can be conducted at room temperature and at 77 K. Samples in Hall bar geometry can also be measured in this system, but for measurements requiring higher precision or magnetic fields, an alternative system was employed.

For measurements of the QHE at low temperatures, a cryostat from the company *Oxford Instruments* was used. It consists of a He^3 cryostat and a superconducting electromagnet. With this system magneto transport measurements at a base temperature of 300 mK and at magnetic fields of up to 14 T could be performed.

2.5. Grazing-incidence synchrotron X-ray diffraction

Grazing-incidence synchrotron X-ray diffraction (GID) measurements have been conducted in order to gain insight into structural properties of the graphene layers grown here.

Synchrotron radiation was employed since it offers high intensities together with a high brilliance within the X-ray band. The experiments were performed at the ID10 beamline of the *European Synchrotron Radiation Facility* (ESRF, Grenoble, France). General details and descriptions of synchrotron radiation and related techniques can be found in References [98, 99].

The technique of grazing-incidence diffraction was used in order to perform diffraction measurements on the lattice planes of graphene. The incident X-ray beam has a shallow angle of incidence α_i with respect to the substrate surface, which is below the angle of total reflectance for the substrate. Therefore, the evanescent waves are exponentially damped within the substrate, which makes this measurement technique sensitive only to the surface structures of the sample. The scattering geometry for GID is depicted in Fig. 2.6.

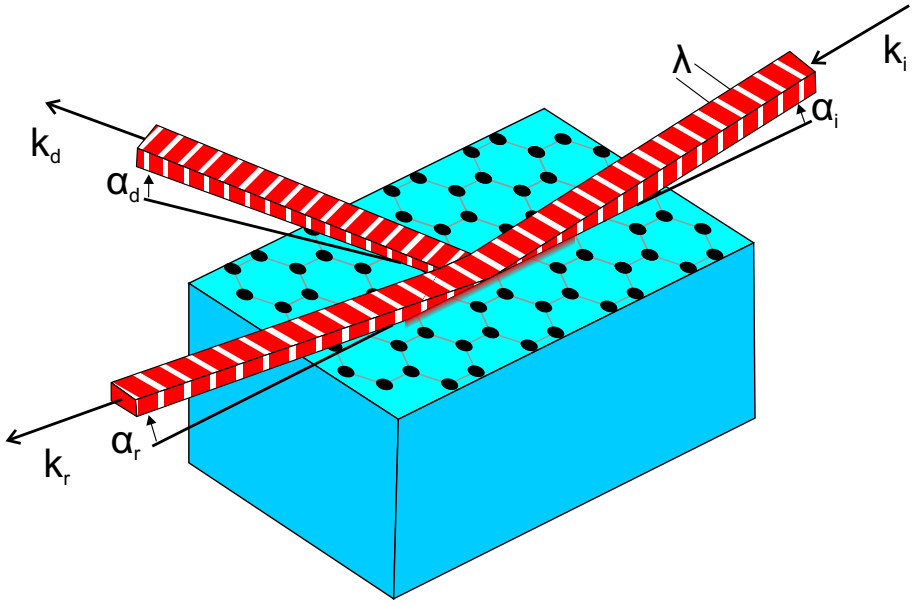

Figure 2.6: Scattering geometry for a GID measurement. k denotes the respective wave vector, α the angle between the beam and the substrate and λ the wavelength of the x-ray radiation. The subscripts i, r, and d denote the incident, reflected and diffracted beam, respectively. Adapted from [100]

The direction of the incoming beam is fixed, while the sample and the detector are rotated in a 1:2 ratio to perform $\Theta - 2\Theta$-scans. To gain information on the in-plane rotation of the lattices, ω-scans are performed by rotating the sample with fixed detector position. Only diffraction from in-plane lattices was investigated, therefore the angle of incidence α_i and the angle of detection α_d were fixed.

3. Epitaxial graphene on SiC

The synthesis of epitaxial graphene (EG) on silicon carbide (SiC) substrates by surface Si depletion is a promising technique to produce large-area and high-quality graphene directly on an insulating substrate. In this chapter, the experimental procedure used to prepare the samples discussed in this work is described, and results are presented.

3.1. Synthesis of epitaxial graphene on SiC by surface Si depletion

SiC is a wide-bandgap semiconductor which exists in various polytypes. For the production of epitaxial graphene, 3C- (cubic), 4H- and 6H-SiC (hexagonal) are the most commonly used polytypes. The structures of these polytypes are shown in Fig. 3.1. Their bandgap varies between 2.3 eV (cubic) and 3.3 eV (hexagonal).[101] In this work, only the hexagonal polytypes are used; more specific the Si-terminated (0001) face. Growth on C-face SiC ($000\bar{1}$) is presented and discussed in Section 3.5. Due to its lower cost, n-doped SiC is used for most samples, but for electric measurements undoped (and hence semi-insulating) SiC substrates were used. Various relevant properties of SiC are summarized in Table 3.1.

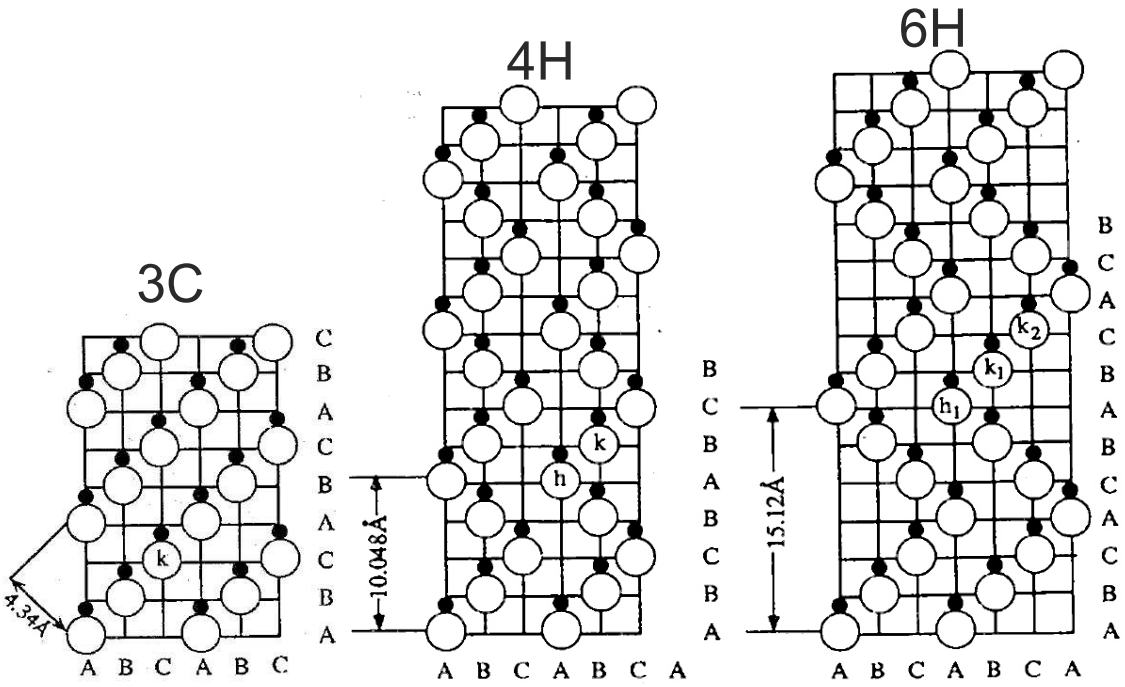

Figure 3.1: 3C-, 4H- and 6H-Sic polytypes. Si atoms are depicted by open circles, C atoms by filled ones. The letters (A, B, C) denote the stacking order of the Si-C bilayers. The figure is adapted from [101].

Polytype	**3C**	**4H**	**6H**
Crystal structure	zink blende (cubic)	wurtzite (hexagonal)	wurtzite (hexagonal)
a_{SiC} [Å]	4.36	3.073	3.073
c_{SiC} [Å]	–	10.05	15.12
Bandgap [eV]	2.3	3.2	3.0

Table 3.1: Properties of SiC. The values are taken from [102].

3.1.1. H-etching of SiC

The first step in the experimental procedure is the chemical cleaning of the $1\times1\,cm^2$ large SiC substrates under ultrasonication. First for 10 minutes in n-butylacetat, followed by 5 minutes in acetone and 5 minutes in methanol or isopropanol. Finally, the sample is dipped in deionized water and blow-dried using high-purity nitrogen. This cleaning is performed in order to remove dirt and organic substances from the surface.

Subsequently, the sample is loaded in the RF-heated furnace (described in Section 2.1) and the reactor is pumped for $\sim$10 – 15 minutes until a pressure on the order of 10^{-5} mbar is reached. Then, the furnace heats up the graphite crucible with the sample to 800 °C in order to desorb contaminations and water from the sample surface.

In the next step, a hydrogen etch is performed. The reactor is filled with Ar until a pressure P of 900 mbar is reached and a flux ϕ_{Ar} of 500 sccm (standard cubic cm per minute) is established. Afterward, the temperature T is increased (by default to 1400 °C). As soon as the temperature reaches the desired value, the flow of Ar is stopped, a flux of forming gas (FG, consisting of 5 at.% H_2 and 95 at.% Ar) is established, and the temperature is held at this temperature for Δt = 15 minutes.

The objective of this etching process is to remove scratches in the SiC surface, which might be present even after the chemical and mechanical polishing performed by the manufacturer, and to form a regular stepped surface.[103,104] This stepped surface results from a miscut of the wafer, which prevents the formation of a perfectly flat surface in which only one crystal face is present. The following chemical reaction takes place during the etching process:[103]

$$\begin{aligned} SiC(s) &\rightarrow Si(l) + C(s) \\ 2C(s) + H_2(g) &\rightarrow C_2H_2(g) \\ Si(l) &\rightarrow Si(g) \end{aligned} \tag{3.1}$$

(s), (l) and (g) denote here the aggregate state solid, liquid or gaseous, respectively. More detailed discussions of the etching process can be found in the References [103–105]. An atomic force microscopy (AFM) image of an etched SiC surface is presented in Fig. 3.2. The surface terraces posses widths of $\sim$1 µm and step heights of $\sim$0.75 nm in between them. This corresponds to half the height of the 6H-SiC unit cell, or three Si-C bilayers.

After the etching process is completed, the RF-heating stops, the flow of forming gas is stopped, a flow of pure Ar is established again, and the reactor cools down to room temperature. In order to remove any possible contaminations from the reactor which might result from the etching process, the reactor is heated up to 1600 °C under Argon flow for $\sim$60 minutes without any sample loaded.

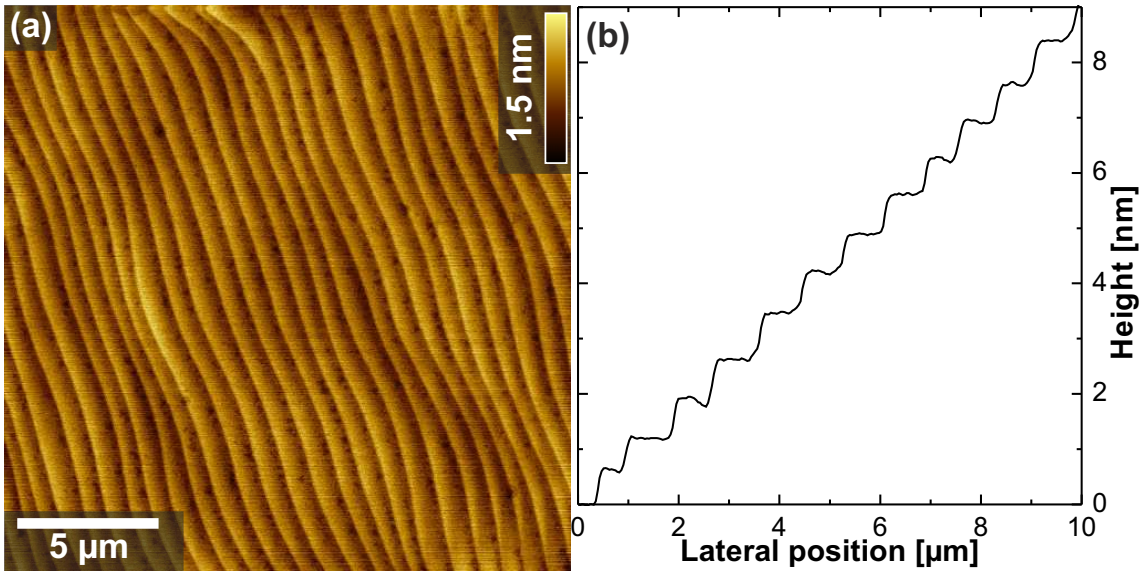

Figure 3.2: (a) AFM image and (b) surface profile of an H_2-etched SiC surface.

3.1.2. Surface graphitization process

The next step performed is the actual EG growth process. The values given here were found to yield the highest quality graphene. Any samples prepared using different parameters are noted. Otherwise, the growth parameters described below were applied.

First, the sample is loaded in the reactor and a vacuum is established. The sample is then outgassed for 15 min at 800 °C in vacuum in order to desorb contaminations from the surface. Subsequently, the reactor is filled with Ar up to a pressure of 900 mbar with a gas flux of 500 sccm. Once the pressure and flux are stable, the RF-coil inductively heats up the crucible and the sample to 1600 °C, and holds the temperature for 15 min. Afterward, the sample cools down (under Ar flux) to room temperature and the process is complete.

Fundamentally, the growth process exploits the fact that silicon has a higher vapor pressure than carbon (or carbon containing components) in the SiC substrate.[106] Therefore, the Si atoms desorb first from the sample surface upon annealing, leaving the C atoms behind, leading a carbon rich surface to emerge, until eventually graphene is formed.

This process was first utilized to produce graphene layers by the group of de Heer in 2004,[10] although surface graphitization of SiC has been observed before.[107] It should be noted that the process was first performed in vacuum, not in an Ar atmosphere. The reason for using Ar will be discussed later.

During sample annealing, primarily Si leaves the SiC crystal,[106] leaving a carbon-rich surface behind. This SiC(0001) surface goes through different phases.[107,108] Low-energy electron diffraction (LEED) patterns, illustrating the different phases, are shown in Fig. 3.3. A more detailed discussion about SiC surface reconstructions can be found e.g. in [109].

Fig. 3.3 (a) shows a 3×3 reconstruction which forms by heating the SiC substrate under a flux of Si. Since this step is not performed in our system, the 3×3 reconstruction does not necessarily develop. Fig. 3.3 (b) shows a $(\sqrt{3} \times \sqrt{3})$R30°–reconstruction. The 'R30°' means, that the reconstruction is rotated by 30° with respect to the SiC substrate. This reconstruction goes through a mixed state [Fig. 3.3 (c)], eventually evolving into a $(6\sqrt{3} \times$

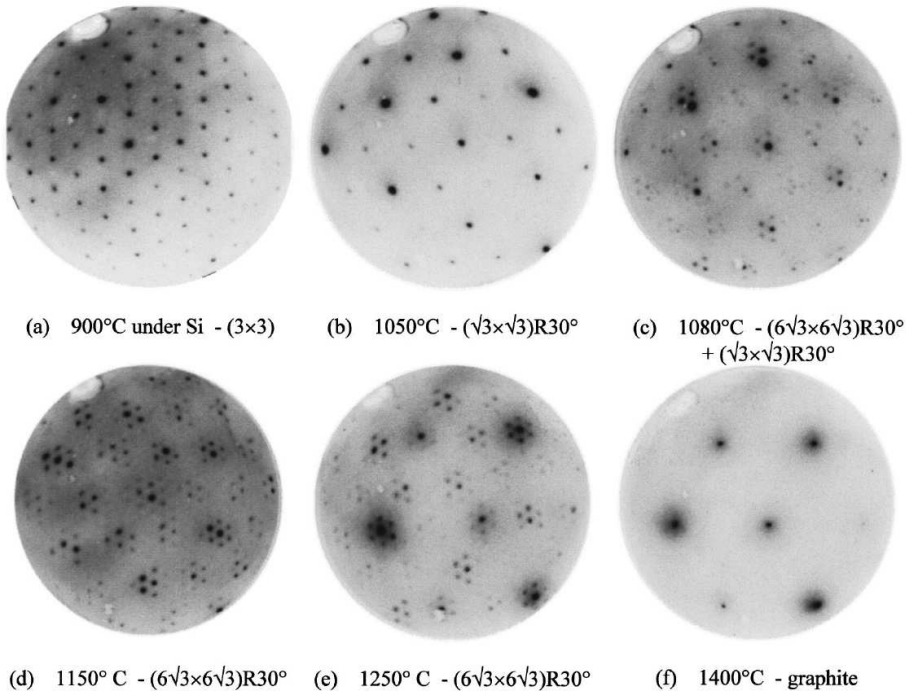

Figure 3.3: LEED images of different surface reconstruction of the SiC surface during the growth process of epitaxial graphene. The image is taken from [107].

$6\sqrt{3})$R30°–reconstruction. This $(6\sqrt{3} \times 6\sqrt{3})$R30°–reconstruction is basically isomorphic to graphene (i.e. it possesses the same honeycomb lattice as graphene and a similar lattice constant). The major difference is that $\sim 1/3$ of the C atoms are in a sp^3–configuration and covalently bound to the SiC substrate.[110] This surface reconstruction (sometimes abbreviated as '$6\sqrt{3}$') is also known as 'buffer layer'(BL)[66] or 'zero layer graphene' (0-LG).[111] By adjusting the growth parameters (i.e. using a lower temperature and Ar flux), it is possible to form only this buffer layer on the SiC surface. This will be further discussed in Section 4.1.

The growth process is schematically depicted in Fig. 3.4. The growth of the epitaxial graphene is not evenly distributed over the complete SiC substrate. Since the Si and C atoms tend to be more weakly bonded in the vicinity of step edges, Si desorbs from these areas more rapidly compared to terraces. This leads graphene to nucleate at step edges first. The schematic in Fig. 3.4 is not to scale; the terraces are actually 100–1000 times broader than the step edges, depending on the miscut of the SiC substrate. Additionally, the effect of step-bunching is not included. Its effect is discussed later, when the influence of step edges on the growth is investigated in detail (see Section 3.2).

Fig. 3.4 (a) shows the stepped SiC surface prior to graphene growth. In Fig. 3.4 (b), the growth process has started. Si atoms sublimate from the SiC surface, initially at the step edges where the buffer layer first forms (yellow in Fig. 3.4), expanding until it forms a closed layer covering the surface. Upon further annealing, more Si atoms leave the surface, and the BL grows from the step edges over the upper terrace.[112] Subsequently, additional Si atoms leave the surface and a 'new' buffer layer forms underneath the existing one. The 'old' BL delaminates from the SiC and becomes a layer of graphene. The covalent bonds to the SiC substrate break and all C atoms in the graphene layer are in a

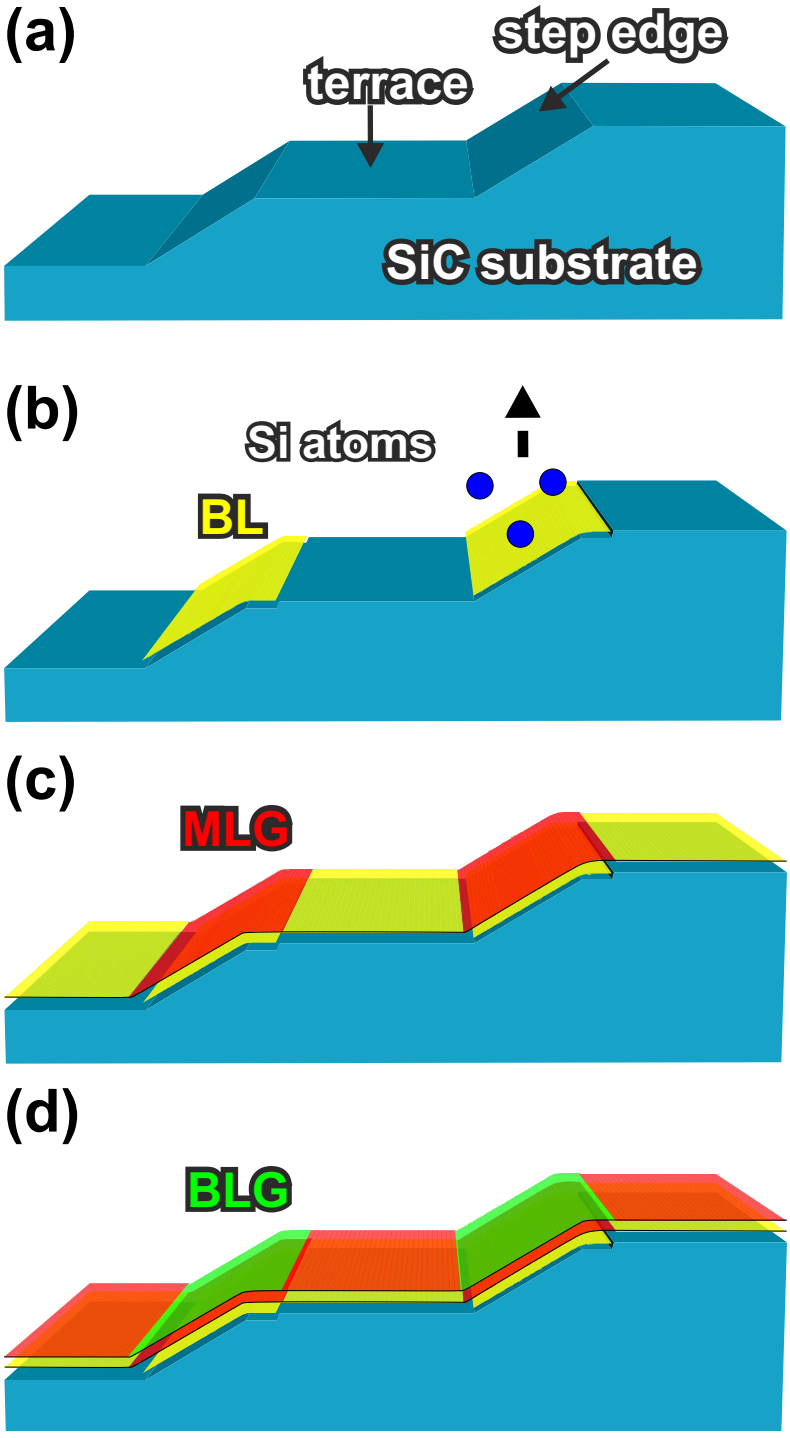

Figure 3.4: Schematic depiction of the growth process of epitaxial graphene through Si depletion of SiC surfaces. Note that the dimensions of terraces and step edges are not to scale, and effects on the surface morphology are not depicted. BL denotes the buffer layer, MLG monolayer graphene, and BLG bilayer graphene. (a) SiC substrate. (b) Nucleation of the buffer layer (yellow) by Si sublimation starts at the step edges. (c) The complete surface is covered by a layer of carbon. At the step edges, a 'new' BL forms out beneath the 'old' one, turning it into graphene (red). (d) The growth continues, the complete surface is covered with graphene, while at the step edges, bilayer graphene (green) already exist.

sp^2 configuration, the graphene sheet is attached to the BL/SiC substrate only by van der Waals forces.[107,113]

The schematic depicted in Fig. 3.4 is simplified, since the SiC step edges are not stationary during the growth process. As Si leaves the surface, the SiC wafer slowly disintegrates, leading to surface morphology changes. Approximately three Si-C bilayers have to disintegrate to provide enough carbon to form one graphene layer.[114] Most strikingly, significant step bunching occurs; the initial steps 'flow' over the surface as graphene is formed, bunch together, and form higher steps with larger terraces in between.[112,115,116]

The atmosphere in which epitaxial graphene formation is conducted has a tremendous influence on the graphene's quality. In our system, the process is not carried out in vacuum, but in an Ar atmosphere close to ambient pressure (usually 900 mbar). This technique was first published by Emtsev *et al.*[11] Compared with the growth in vacuum, the utilization of Ar improves the quality of the graphene layers greatly. The key factor is the higher temperature during the growth process allowed by the Ar. The temperature for the growth in vacuum is usually ∼1200 – 1400 °C, while it is ∼1600 °C in Ar. The presence of Ar at a relative high pressure reduces the Si evaporation rate because of finite Si-backscattering by the Ar atoms.[117] The higher temperature increases the diffusion of surface species, allowing ordering processes to take place more efficiently. AFM images comparing epitaxial graphene grown in vacuum and Ar are shown in Fig. 3.5.

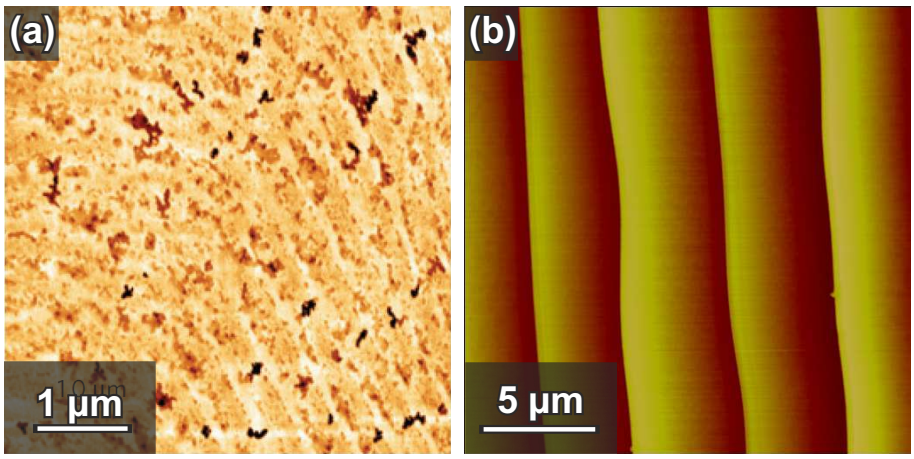

Figure 3.5: AFM images of epitaxial graphene synthesized in vacuum and Ar. (a) Growth in vacuum at a temperature of 1280 °C. The image was taken from [11]. (b) Growth in a 900 mbar Ar atmosphere at 1600 °C.

The surface roughness is much higher in the case of the preparation in vacuum. This is accompanied by a non-uniform distribution of graphene, with different numbers of graphene layers across one terrace.[11] On the other hand, the sample synthesized in Ar possesses an atomically smooth surface covered with monolayer graphene. Bilayer graphene has formed during the growth process only at the step edges. Additionally, the electrical transport characteristics improve using an Ar atmosphere. The electron mobility rises from ∼500 – 800 cm^2/Vs (vacuum) to ∼1000 – 4000 cm^2/Vs (Ar). Details on these transport measurements are presented in Section 3.3.

The structural quality of the graphene layers can be investigated by means of Raman spectroscopy, as described in 2.3. A representative spectrum is shown in Fig. 3.6, which was recorded using a microscope with a 100× objective with spatial resolution of 1 µm. The 482.5 nm line of a Kr^+ laser was used for excitation. Since the SiC substrate possesses

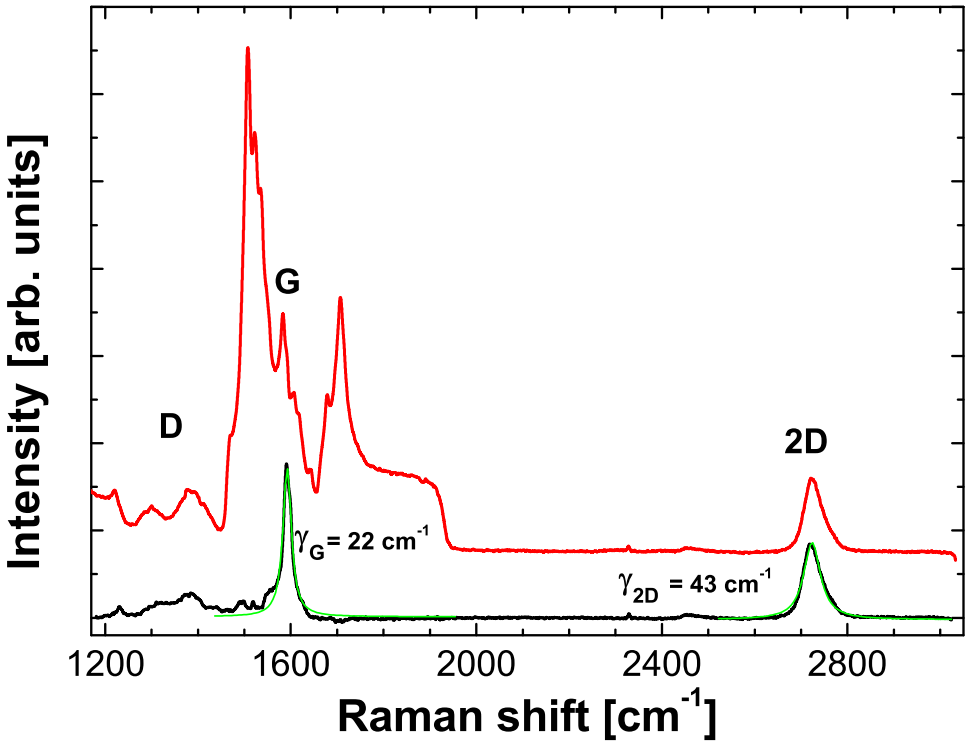

Figure 3.6: Representative Raman spectra taken at the terrace of epitaxial graphene on SiC. The upper curve (red) shows the spectrum before, the lower curve (black) after SiC background subtraction. Lorentzian-shaped peaks fitted to the G- and 2D-peaks are shown in green.

Raman active modes in the same spectral region as graphene, the SiC background must be subtracted.

The G- and 2D-peaks are clearly resolved in the spectrum after background subtraction. The G- and 2D-peak can each be fitted by a single Lorentzian (shown in green in Fig. 3.6), which means that the graphene is likely composed of a single layer. The observed intensity in the region of $\sim$1200 – 1400 cm^{-1} is due to the underlying buffer layer, and not to a defect-related D-peak. It is possible to detach the buffer layer from the SiC substrate and convert it into an additional layer of graphene (details can be found in Reference [118], and will shortly be discussed in Section 3.4). If this detachment is performed, the BL signal vanishes to a large extent, and only a small D-peak is visible. Since a healing of defects during the detachment process is highly unlikely, one can assume that the intensity of the D peak is equally low prior to the intercalation process, and that the acquired signal hence originates from the buffer layer. Details of the BL's Raman spectra are discussed in Section 4.1 or in References [66, 119].

We also investigate the electrical characteristics of the graphene layers. This is usually done at low temperatures, since the used SiC substrates are typically n-doped with nitrogen donors which freeze out at a temperature of 50 K.[120] Therefore, a temperature below 50 K is required to probe transport through only the graphene. The epitaxial graphene is n-doped with a carrier concentration on the order of 10^{12} cm^{-2}, with carrier mobilities on the order of 1000 cm^2/Vs (room temperature) up to 4000 cm^2/Vs (low temperatures). The mobility is decreased at room temperature due to interaction of the electrons with

substrate phonons.[121] When compared with exfoliated graphene flakes, the graphene discussed here has a relatively high carrier concentration and low mobility. This results from its interaction with the BL. As mentioned, the BL is partially bound to the SiC substrate, and dangling bonds from the substrate also exist underneath the BL. This induces disorder and a relative high carrier concentration which are partly transferred to the graphene layer. Further details regarding electrical measurements can be found in Section 3.3.

3.1.3. Synthesis of the buffer layer

As mentioned above, the BL is a $(6\sqrt{3} \times 6\sqrt{3})$R30°–reconstruction of the SiC(0001) surface, which forms upon annealing due to surface Si depletion.

During the growth of epitaxial graphene on SiC, the BL appears on the surface as an intermediate state. However, it is also possible to only synthesize a bare BL. For the preparation of the BL, the first steps (cleaning and H-etching, see 3.1.1) are identical to the preparation of EG on SiC. The surface graphitization takes place in a 900 mbar Ar atmosphere with a flux of 100 sccm, at a temperature of 1450 °C, and the annealing time is 15 min. A representative AFM image is shown in Fig. 3.7 (a), while Fig. 3.7 (b) shows a measurement with higher magnification taken on a single surface terrace.

Similar to the growth of EG, step bunching takes place during growth which results in larger terraces and steps with heights of ∼10 nm. The terraces are atomically flat with a root-mean-square (rms) roughness of about 0.8 Å when measured on a single terrace. This value is likely limited by the AFM used, and thus should be regarded as an upper limit.

The existence of a continuous BL over the entire surface was proven by Raman spectroscopy. The BL has a specific Raman signature in the same spectral region as graphene. It is composed of two broad and intense features at ∼1320 cm^{-1} and at ∼1560 cm^{-1}. Additionally, broad and rather low intense features are visible at ∼2600 – 3000 cm^{-1}. A representative Raman spectrum is shown in Fig. 3.8, together with the spectrum of EG for comparison.

Interestingly, the Raman intensity obtained by measurements on a pristine BL is much more intense than the intensity from a BL which is underneath a graphene layer, as it is

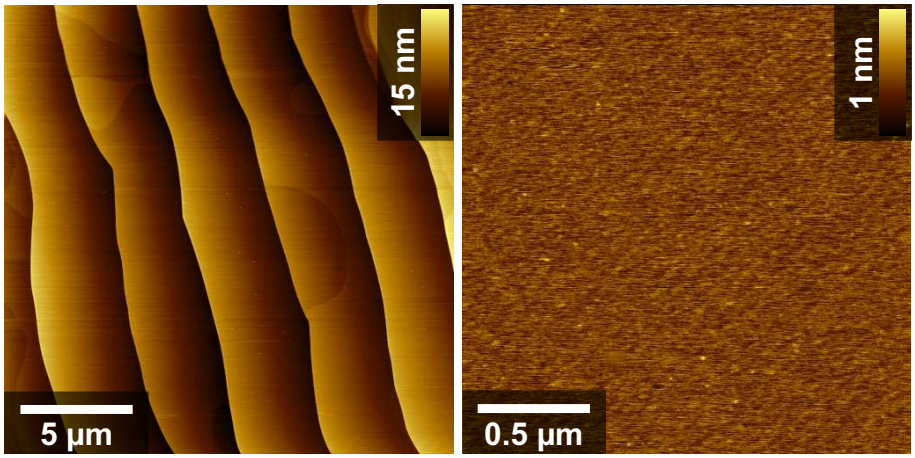

Figure 3.7: AFM images of a buffer layer produced by surface Si-depletion. (a) Several terraces, (b) one single terrace.

the case in EG. A more detailed study on the Raman spectrum of the BL can be found in [66].

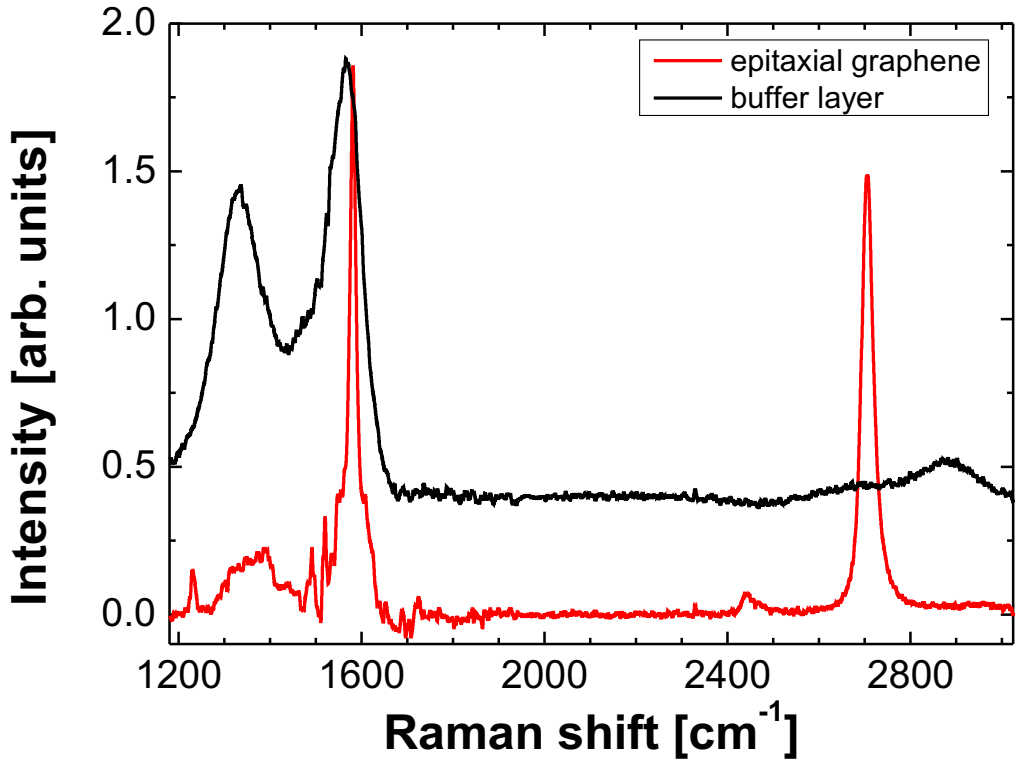

Figure 3.8: Raman spectra of the buffer layer and of epitaxial graphene. The SiC background signal was subtracted, and both spectra were normalized with respect to the SiC background. The spectra are shifted for better visibility.

3.2. The influence of SiC surface steps on the graphene growth process

In this section, the influence of the initial SiC surface morphology on the graphene growth is investigated. The results presented here were published in [122].

After the H-etching, the SiC surface usually features steps with a height of 0.75 nm or 1.5 nm. The graphitization process causes the surfaces to adopt a stepped morphology but with higher steps and larger terraces. This step bunching has been observed in all previous experiments, yet it was still not clear whether or not it is essential for the growth of high-quality graphene layers. Here, the growth on differently stepped SiC surfaces, and its influence on the graphene formation is investigated. The SiC surface morphology was manipulated by varying the temperatures during H-etching, and the influence of the resulting step edge configurations on graphene growth was investigated.

The EG samples are prepared as previously described, but the temperature during H-etching for the different samples varies between 1350 °C and 1550 °C (with all other parameters maintained constant (i.e. $\Delta t = 15$ min, $P = 900$ mbar, $\Phi_{FG} = 500$ sccm). The surface morphology of the samples was investigated before and after the graphene preparation by means of AFM measurements.Fig. 3.9 (a) corresponds to the surface of an non-etched sample. The wafer was treated by the manufacturer *NOVASiC* with their 'epi-ready'[123] process, and its surface is composed of steps with a height of ∼0.3 nm and terraces with a width of ∼0.2 µm. Fig. 3.9 (b) and (c) present samples etched at 1400 °C and 1350 °C, respectively. This results in step-heights of ∼0.75 nm and ∼1.5 nm, which correspond to half or full the height of the 6H-SiC unit cell ($c_{6H\text{-}SiC} = 1.5$ nm). Their average terraces widths are ∼0.67 µm and ∼1.2 µm, respectively. It has to be mentioned that intuitively one would expect higher step heights at higher etching temperatures (which is usually the case), but unfortunately the production of samples with a step height of 1.5 nm is

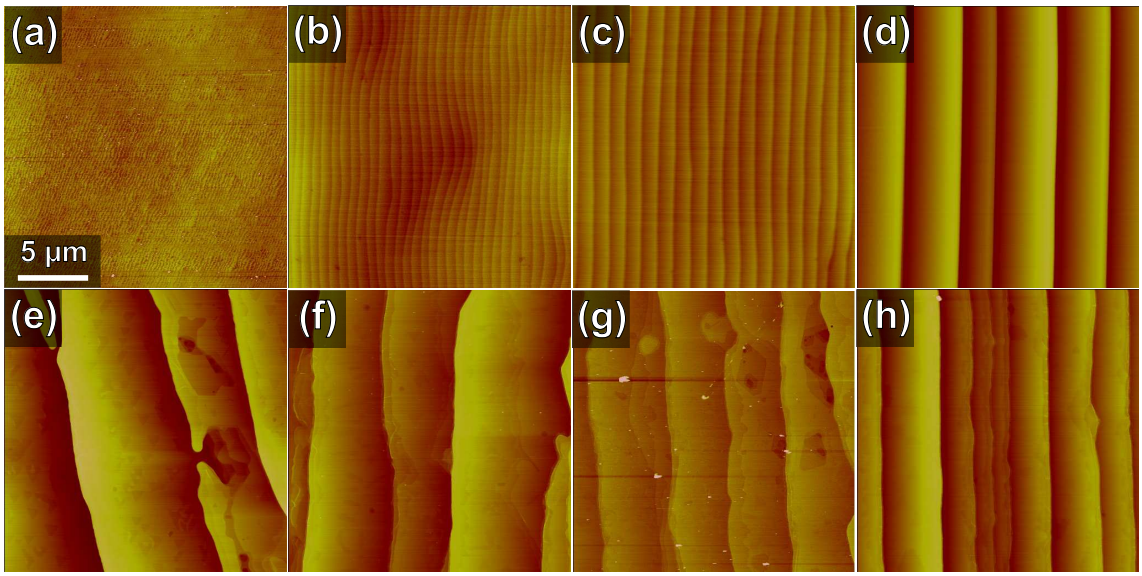

Figure 3.9: AFM images of (a) a non-etched SiC(0001) surface (0.3 nm step height), (b) a H-etched surface with step heights of $(1/2)\cdot c_{6H\text{-}SiC}$ (0.75 nm), (c) a H-etched surface with step heights of $c_{6H\text{-}SiC}$ (1.55 nm), and (d) a H-etched surface with large step heights (∼13 nm), all images obtained before EG preparation. The respective AFM images obtained after the graphitization process are shown in (e) – (h).

difficult to reproduce. This is likely because the specific crystallographic orientation of the steps also plays a role.[104] Fig. 3.9 (e) – (g) show the sample morphology after the graphene growth process. In each case, the surface consists of relatively large terraces, with average widths of ∼5.5 µm and step heights of ∼6 nm. Therefore, the additional step-bunching which occurs during graphitization yields a consistent final morphology, regardless of the initial step configuration.

A different scenario is presented in the last column of Fig. 3.9. Fig. 3.9 (d) presents an AFM image of a SiC surface H-etched at T = 1550 °C, which is composed of rather large terraces with an average width of ∼3.7 µm, and step heights of ∼13 nm. The AFM image of the sample after EG formation [Fig. 3.9 (h)] shows a surface quite similar to the initial one. Interestingly, the average values of 13 nm for the step heights and 3.7 µm for the terrace widths remain the same, which means that no additional step bunching took place during the graphene synthesis. AFM surface profiles of two different samples unambiguously show the presence of step bunching [Figs. 3.10 (a) and 3.10 (b)] or its absence [Fig. 3.10 (c) and Fig. 3.10 (d)].

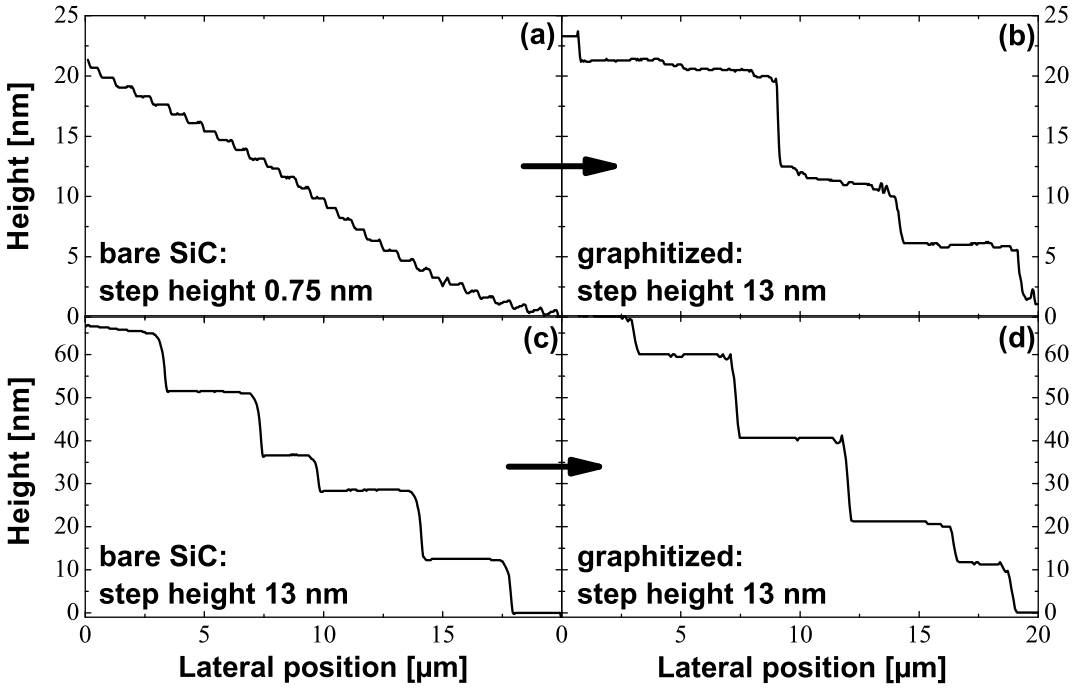

Figure 3.10: Comparison of AFM surface profiles of the stepped SiC surface with initial step heights of half $c_{6H\text{-}SiC}$ (0.75 nm) and terraces of 0.67 µm in width before (a) and after (b) graphene growth, and for the stepped surface with initial step heights of 13 nm before (c) and after (d) graphene formation, where no additional step bunching is observed.

The suppression of step bunching might be due to the fact that the initial surface has already reached a configuration of minimum surface free energy,[104,124] which for the other samples could only be achieved during the graphitization process. Even though no additional step bunching is observed, movement of the steps along the surface might still occur[125] since additional Si-C bilayers disintegrate during the graphene growth process.

To investigate the influence of different initial SiC surface morphologies on the structural properties of graphene, Raman spectroscopy measurements were conducted on the terrace and step-edge-regions of each sample after EG formation (Fig. 3.11). In this study, the spectra were recorded using the 413.1 nm line of a Kr^+ ion laser with a spatial resolution at the sample surface of 1 µm. The SiC Raman signals have been subtracted from all spectra in Fig. 3.11.

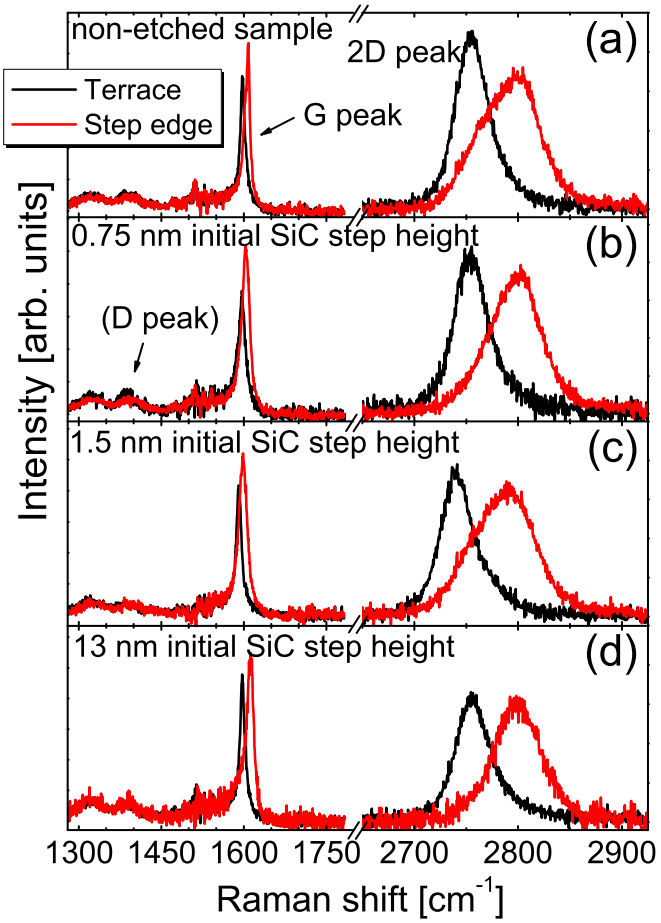

Figure 3.11: Raman spectra of the graphene samples prepared on SiC substrates with different initial surface morphologies, measures on the terrace (black) and on the step edge (red).

For all samples, similar spectra are obtained, regardless whether the measurements were taken on terraces or step-edge-regions. The visible intensity in the spectral region of 1500 cm^{-1} and 1325 – 1375 cm^{-1} is due to the presence of the buffer layer underneath the graphene (see discussion in section 4.1). Another possibility is the presence of the defect induced D-peak (1380 cm^{-2} for the used excitation laser energy). However, the measured intensity in this spectral region is very low, indicating that the analyzed samples possess a high structural quality, with few defects, and that the structural quality is not dependent on the extend of additional step bunching during growth.

The 2D-peak recorded for measurements on a terrace can be fitted by one single Lorentzian with a full width at half maximum (FWHM) of ∼35 cm^{-1} for all samples. This

means that there is a single layer of graphene in these regions.[90] On the other hand, the 2D-peak is broader in the step-edge-regions (FWHM $\sim$64 cm^{-1}), and possesses an asymmetric shape with a shoulder towards lower wave numbers. This indicates the presence of bi- or even tri-layer graphene in this region.[115,116,125,126] Alternatively, this could be due to contributions with different frequencies originating from the step edges and the adjacent terraces, since the laser spot is larger then the step-edge-regions.

The G-peak is located at about 1596 cm^{-1} for every sample, if recorded on a terrace, and at $\sim$1605 cm^{-1} if recorded at a step-edge-region. The blue-shift of about 9 cm^{-1} is accompanied by a broadening of the peak of $\sim$3 cm^{-1}. The same holds true for the 2D-peak which shifts from $\sim$2752 cm^{-1} (terrace) to $\sim$2800 cm^{-1} (step-edge-region). The blue-shifts of both G- and 2D-peaks are caused by a difference in strain[88,127] and/or charge carrier density.[84,85] Additionally, the presence of more than one layer of graphene in the step-edge-regions has an influence on the spectral position of the Raman peaks. Therefore, the peak-shifts cannot be used to quantify differences in strain and charge carrier densities between the two regions. However, the near-absence of a D-peak in each case indicates that the structural quality is good, and is comparable in both graphene regions. The most important observation is that the presence or absence of step bunching during graphene formation does not influence the resulting structural quality. But since the presence of large surface steps cannot be avoided, their impact on potential applications is an important issue. In the next section, the influence of the surface steps on electrical transport is investigated.

3.3. Anisotropic quantum Hall effect in graphene on stepped SiC surfaces

In this chapter the anisotropic behavior of the quantum Hall effect (QHE) in graphene on stepped SiC surfaces is discussed. We first introduce the general properties of the QHE in graphene, and reference measurements on epitaxial graphene layers on SiC are then presented. The specific details of the structures investigated here are then discussed, leading to an in-depth discussion of the associated experimental results. Finally, we introduce a qualitative model which explains these results. The results presented in this chapter have previously been published in [128].

3.3.1. Quantum Hall effect in graphene

Due to graphene's unusual band structure (with its linear dispersion relation at the K and K' points in the Brillouin zone) the QHE is different in graphene when compared to conventional 2D semiconductors (e.g. 2-dimensional electron gases in GaAs/AlGaAs heterostructures). A concise description of the QHE is provided in Appendix A. In conventional semiconductors, the Hall conductivity σ_{H} (which is the inverse of the Hall resistance $\mathrm{R_H}$) is given by:

$$\sigma_{\mathrm{H}} = \frac{1}{\mathrm{R_H}} = \nu \cdot \frac{e^2}{h} = \mathrm{N} \cdot g \cdot \frac{e^2}{h}, \tag{3.2}$$

where ν denotes the filling factor, h Planck's constant, e the electron charge, N the Landau level (LL), and g the degree of degeneracy of this LL.

In graphene however, the situation is described by the so called 'half integer quantum Hall effect'.[15] Due to the existence of states at the Dirac point, the N = 0 LL is half-filled with electron and hole states, and the Hall conductivity is not zero.[129] The quantization is described by:

$$\sigma_{\mathrm{H}} = \frac{1}{\mathrm{R_H}} = \nu \cdot \frac{e^2}{h} = 4\,(\mathrm{N} + 1/2) \cdot \frac{e^2}{h}. \tag{3.3}$$

The factor of 4 is here due to the fourfold degeneracy of the LLs in graphene (2 valley + 2 spin). For instance, LL N = 0 describes the state in which all free carriers occupy the lowest LL, corresponding to the filling factor $\nu = 2$.

The quantum Hall effect measurements discussed here were performed on epitaxial graphene on 6H-SiC substrates. An optical micrograph of a representative Hall bar is shown in Fig. 3.12 (a).

Fig. 3.12 (b) illustrates a typical quantum Hall effect measurement performed on a 10-µm-long and 5-µm-wide Hall bar. Here, one surface step edge crosses the Hall bar diagonally. Several Shubnikov-de Haas (SdH) oscillations are visible in the longitudinal resistivity, which means that the carriers condense in the Landau levels. This is clear evidence for the quantum Hall effect, despite the minima not reaching zero resistivity. The minima in the SdH oscillations coincide with plateaus in the Hall resistance [red curve in Fig. 3.12 (b)]. Three Hall plateaus are observable (Landau levels N = 0 – 2). The values of these plateaus are given by Equation 3.3 and are marked by dotted lines in Fig. 3.12 (b), and agree well with the experimental observation. This proves that the epitaxial graphene on SiC behaves electronically like free-standing monolayer graphene, at least in regard to the anomalous half-integer quantum Hall effect.

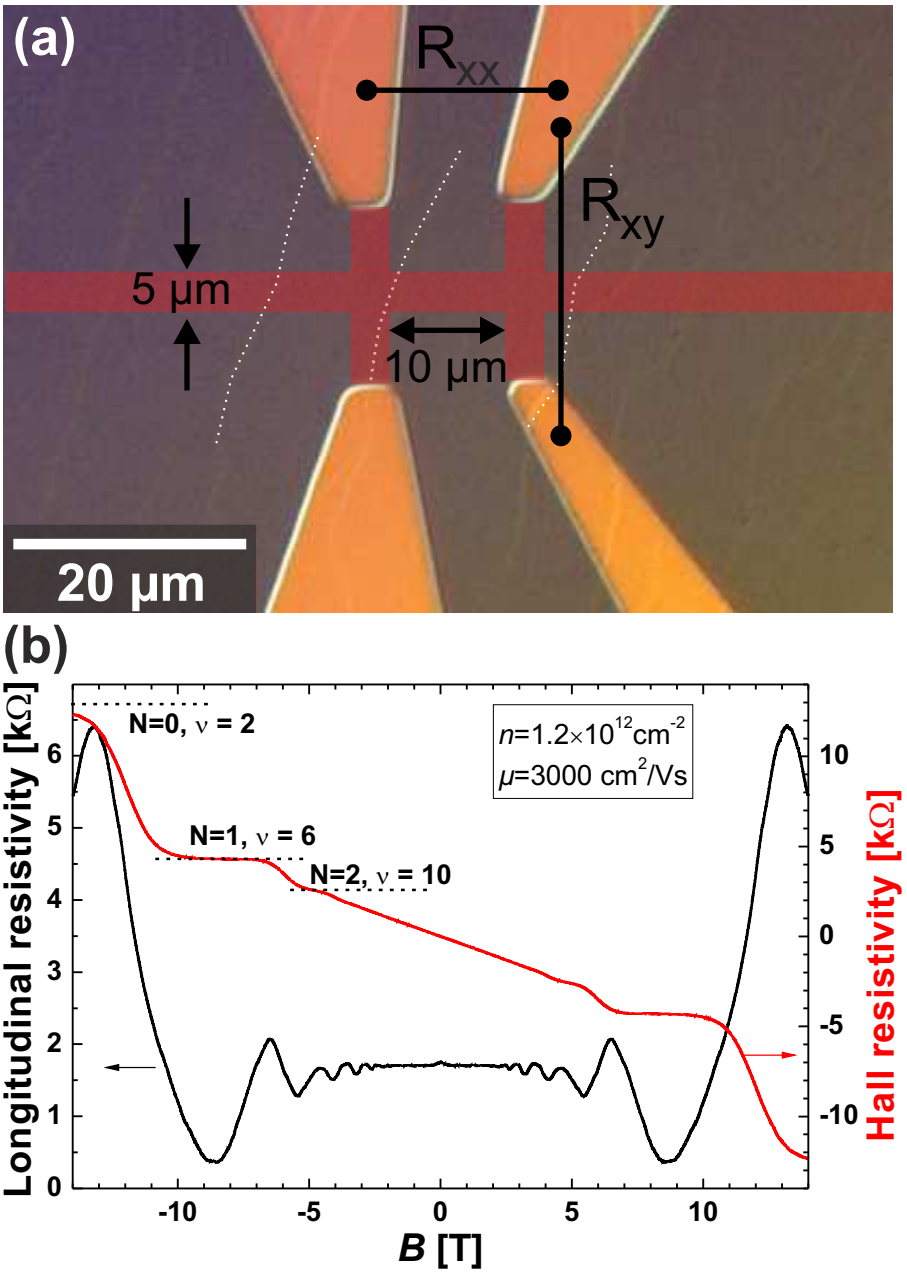

Figure 3.12: (a) Optical micrograph of a representative Hall bar structure. Here, only one surface step edge crosses the Hall bar. The positions of some step edges are indicated by dotted white lines. (b) Quantum Hall effect in epitaxial mono-layer graphene on SiC(0001). The dotted lines indicate the literature values of the Hall plateaus. The Landau level index is denoted by N, ν denotes the filling factor.

From these measurements, the carrier type (electrons or holes), the sheet carrier concentration n, and the charge carrier mobility μ can be deduced. The carrier type and concentration may be determined by measuring the Hall coefficient (i.e. the slope of the Hall resistance near $B = 0$ T). If only one carrier type is responsible for carrying the electric current, its density is given by:

$$n = \frac{1}{e \cdot A_H}. \tag{3.4}$$

The carrier type is given by the sign of A_H ($A_H > 0 \rightarrow$ holes, $A_H < 0 \rightarrow$ electrons). The charge carrier mobility is in turn described by:

$$\mu = \frac{A_H}{\rho_{xx}|_{B=0\,T}}, \tag{3.5}$$

where $\rho_{xx}|_{B=0\,T}$ is the longitudinal resistivity at zero magnetic field.

These methods both rely on the classical Hall effect at low magnetic fields. From the measurement shown in Fig. 3.12 (b), we extract a carrier density of $n = 1.2 \times 10^{12}$ cm^{-2} and a carrier mobility $\mu = 3000$ cm^2/Vs.

An alternative method to determine the carrier concentration is to examine the frequency of the minima and maxima in the SdH oscillations. The number of states per LL is given by:[130]

$$n_L = \frac{e \cdot B}{h} \cdot g, \tag{3.6}$$

where e is the electron charge, B the magnetic field, h is Planck's constant and g the level of degeneracy. The number N of filled Landau levels is thus:

$$N = \frac{n}{n_L} = \frac{n \cdot h}{g \cdot e \cdot B}, \tag{3.7}$$

where n denotes the carrier concentration. Therefore:

$$n = \frac{g \cdot e}{h} \underbrace{\frac{N}{1/B}}_{S}. \tag{3.8}$$

Plotting the maxima/minima of the SdH oscillations versus 1/B yields a linear relationship. When fit, the slope S directly determines the carrier density via Equation 3.8. For the presented measurement, this is shown in Fig. 3.13.

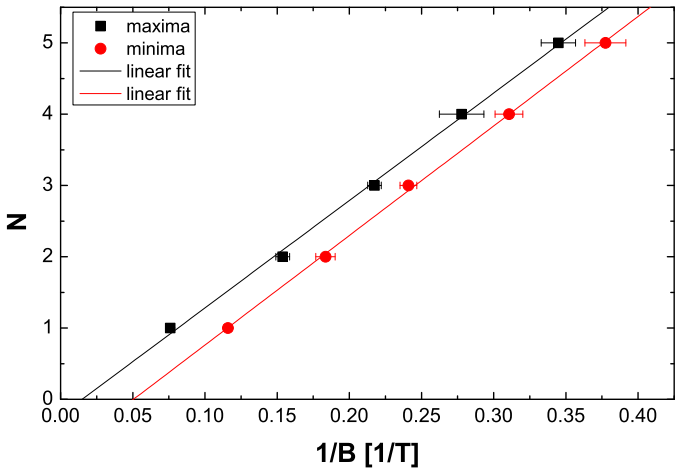

Figure 3.13: Index of SdH oscillations plotted against the position of their maxima/minima in 1/B.

The carrier density extracted by this method has a value of $n = 1.5 \times 10^{12}$ cm^{-2}, which is slightly different from the value obtained from the Hall coefficient A_H. Since measuring the carrier density from the SdH oscillations relays on a purely quantum mechanical

effect, and is not influenced by resistances from contact leads etc., n will be derived by this method when applicable.

3.3.2. Quantum Hall effect on stepped SiC surfaces

The properties of epitaxial monolayer graphene described above have been previously investigated by several research groups.[30,131,132] But, as was shown in Section 3.2, steps and terraces are formed during the growth of graphene on SiC. The influence of these step edges on magnetotransport is investigated in the following section.

Only recently has the electronic transport in epitaxial graphene on SiC been investigated with respect to the direction of terraces and step edges on the surface. Yakes *et al.*[133] reported that the electrical resistance in graphene, grown either on the (0001) or $(000\bar{1})$ face of SiC, is different when measured in two distinct directions (i.e. parallel or perpendicular to the surface terraces). A moderate increase in the resistance was observed for the perpendicular direction, which was attributed to a charge buildup occurring at the step edges, leading to increased scattering of charge carriers. In addition, Ji *et al.*[134] showed that not only defects, but also graphene monolayer-bilayer junctions at the step edge regions (as indicated in Fig. 3.4) contribute to the electrical resistance. In contrast, Jobst *et al.*[132] measured magnetotransport in epitaxial graphene grown on SiC(0001) and observed both mobility and charge carrier density are insensitive to surface steps when measured at low magnetic fields. Note that the experimental conditions (i.e. temperature, atmosphere, and pressure during the growth process) employed for the synthesis of the EG were different for the studies cited above,[132–134] which could explain the apparent differences between the obtained results. Despite these studies, there remain many open questions regarding the influence of SiC surface steps on the magnetotransport properties of epitaxial graphene.

Here, magnetotransport in graphene is investigated at high magnetic fields for narrow Hall bars, aligned parallel or perpendicular to surface terraces. For this purpose, epitaxial graphene was grown on semi-insulating 6H-SiC(0001) substrates with a miscut of about 1°. Sample preparation was performed according to the method described in Section 3.1. Multiple Hall bars, aligned either parallel or perpendicular to the surface terrace, were defined using conventional optical lithography and O_2 plasma etching. Ti/Au layers with 10/100 nm thickness were used as electrical contacts. The morphology of the Hall bars was checked using AFM. Two representative images of Hall bars with a width of 2 μm and length of 30 μm are shown in Fig. 3.14. The dotted lines mark the Hall bar structures, and the elevated structures are the electrical contacts. While the Hall bar crosses two steps when it is aligned in parallel to the steps [$HB_{\parallel}$ - see Fig. 3.14 (a)], more than 25 steps are crossed when the Hall bar is aligned perpendicular to the terraces [$HB_{\perp}$ - see Fig. 3.14 (b)].

The terraces on both samples are about 1 μm wide with step heights varying from 10 to 25 nm. The device layout and sample surface morphology were chosen to maximize the influence of the steps on the electrical measurements. Residual photoresist from the lithography processes is still present on the graphene Hall bar. It has been previously shown that such residue does not fundamentally affect the properties of graphene on SiC (carrier density and mobility).[30,132] Electrical measurements were carried out in an *Oxford Instruments Heliox* He^3 cryostat with a base temperature of 320 mK and at magnetic fields B up to 14 T perpendicular to the surface. Longitudinal (ρ_{xx}) and Hall (ρ_{xy}) resis-

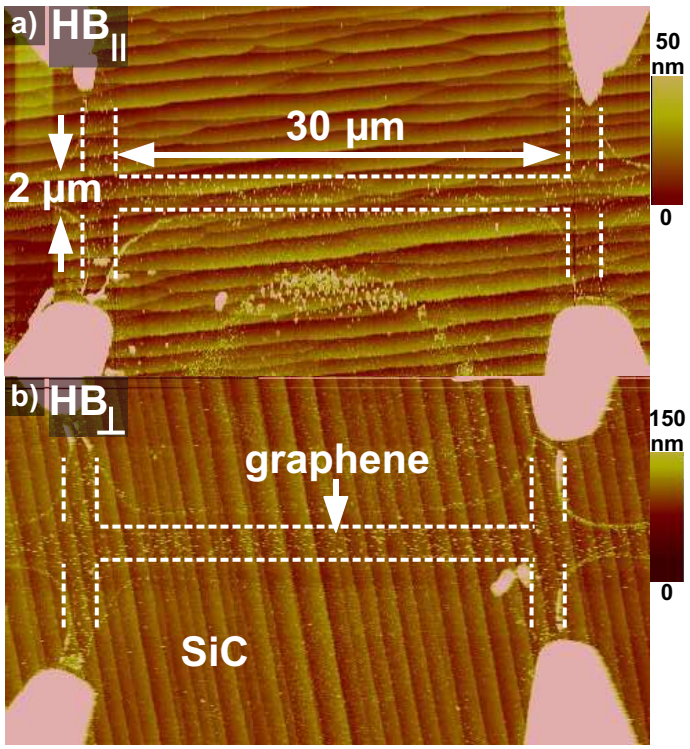

Figure 3.14: Representative AFM images of two graphene Hall bars, aligned (a) parallel ($HB_{\parallel}$) and (b) perpendicular ($HB_{\perp}$) to the terraces on the surface. The dotted lines mark the perimeter of the Hall bar.

tivities were measured in a Hall bar geometry, using 4-terminal contacts with a current of 100 nA in a standard lock-in technique.

The structural properties of the patterned graphene, such as defects and strain, were investigated by Raman spectroscopy with a spatial resolution of 1 µm, using the 482.5 nm line of a Kr^+ ion laser (see Section 2.3). Raman spectra were recorded at positions along the Hall bars with a spacing of 1 µm. The results are depicted in Fig. 3.15. In Fig. 3.15 (a), two representative Raman spectra are shown, which correspond to measurements performed on a terrace and on a step edge. The G- and 2D-peaks of the spectrum recorded on the step edge are blue-shifted with respect to those of the spectrum obtained on the terrace. It is known that the position of both peaks depends on strain[88,127] and carrier density.[135,136] In a recent work, it was also reported that there is a strong correlation between the strain and charge density in epitaxial graphene,[137] with an increase in compressive strain causing a decrease in electron doping. Thus, the observed blue-shift of both peaks indicates that there is a difference in strain (associated with the shift of the G- and 2D-lines) and carrier density (associated to the shift of the G-line) between the two surface regions.

The presence of bilayer graphene at the step edge region may also contribute to a blue-shift of the 2D-line.[122,137] In order to obtain information about the inhomogeneity of strain and carrier concentration, the spectral position of the G-peak was measured along the two Hall bars in Fig. 3.14, as is plotted in Fig. 3.15 (b) and (c). The position of the G-line changes slowly along $HB_{\parallel}$, since in this case only two steps pass the Hall bar diagonally. Indeed, evidence for two surface regions (i.e. terrace and step edge) with distinct properties is the existence of two plateaus at different wavenumbers, one at about 1600 cm^{-1}

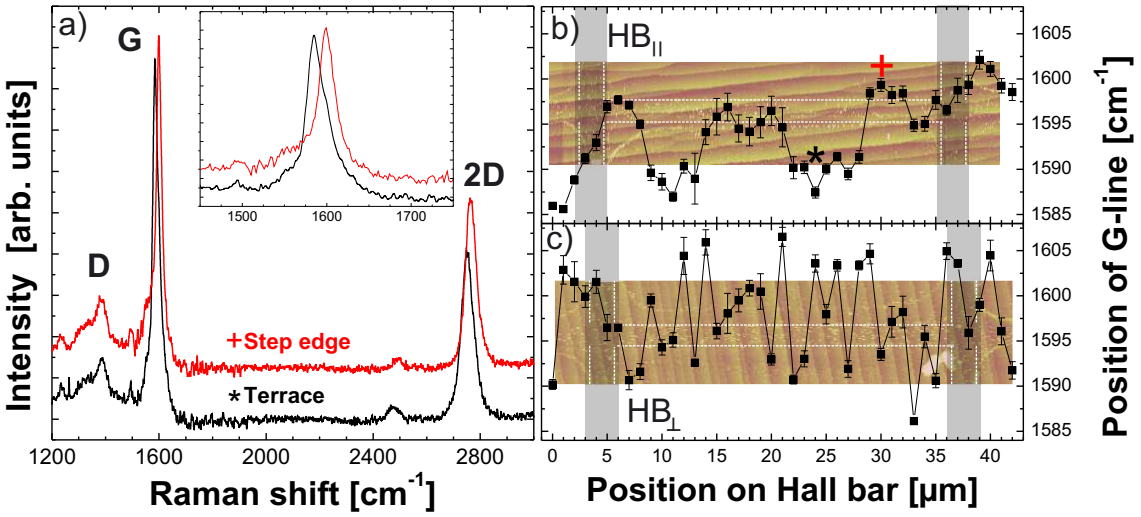

Figure 3.15: Raman measurements from two graphene Hall bars. (a) Two representative spectra, taken at positions marked by the asterisk and the cross in (b). The spectra are offset for better visibility. The inset shows the region of the G-line. Peak position of the G-line along a Hall bar aligned (b) parallel to the terraces and (c) perpendicular to them. The corresponding AFM images from Fig. 3.14 are in the background to clarify the correlation between the step edges and the spectral position of the G-line. The positions of the terminals for contacts are marked by the shaded areas. The dotted lines in (b) and (c) mark the Hall bars.

(step edge region) and another at about 1590 cm^{-1} (terrace). For the $\mathrm{HB}_{\perp}$, fluctuations are present on a short length scale since it crosses many steps, and the terraces widths are on the order of the laser spot size. One can clearly observe that the variability in G-peak position is much more pronounced for this Hall bar. Additionally, it is important to point out that a signal in the region of 1380 cm^{-1} is observed in both spectra [see Fig. 3.15 (a)], which is very similar for both samples and could correspond to the disorder-induced D-line.[84] Alternatively, the intensity in this region could be due to the presence of the buffer layer beneath the graphene film.[66] However, the low intensity of this peak shows that there is only a small amount of defects in the graphene structure. This is an indication for the high structural quality of the epitaxial graphene produced here. Reference Raman measurements on pristine and unprocessed graphene which was grown on a SiC piece from the same wafer show identical features (not shown).

In contrast to the reference measurements shown in Fig. 3.12, Hall bars with a reduced width and larger length (such as those depicted in Fig. 3.14) do not show multiple clearly observable Hall plateaus. The Hall plateaus for the Landau levels with $\mathrm{N} \geq 1$ vanish, probably due to the increased interaction of conducting edge channels. Fig. 3.16 shows measurements on Hall bars with a width of 2 µm and a length of 40 µm. The Hall bars aligned parallel and perpendicular to the terraces exhibit n of about 7.7 and 5.5×10^{11} cm^{-2}, with μ of ∼3500 and ∼3100 $\mathrm{cm}^2/(\mathrm{Vs})$, respectively. The longitudinal resistivity at zero magnetic field is higher for $\mathrm{HB}_{\perp}$. In other measured structures, the resistivity at $B = 0\,\mathrm{T}$ is comparable or even higher for $\mathrm{HB}_{\parallel}$. Such variations might be an effect of nonuniformities in the graphene structure (e.g. slightly different local carrier densities or dimensions produced by lithography and plasma etching), and it is not necessarily related to the stepped surface structure.

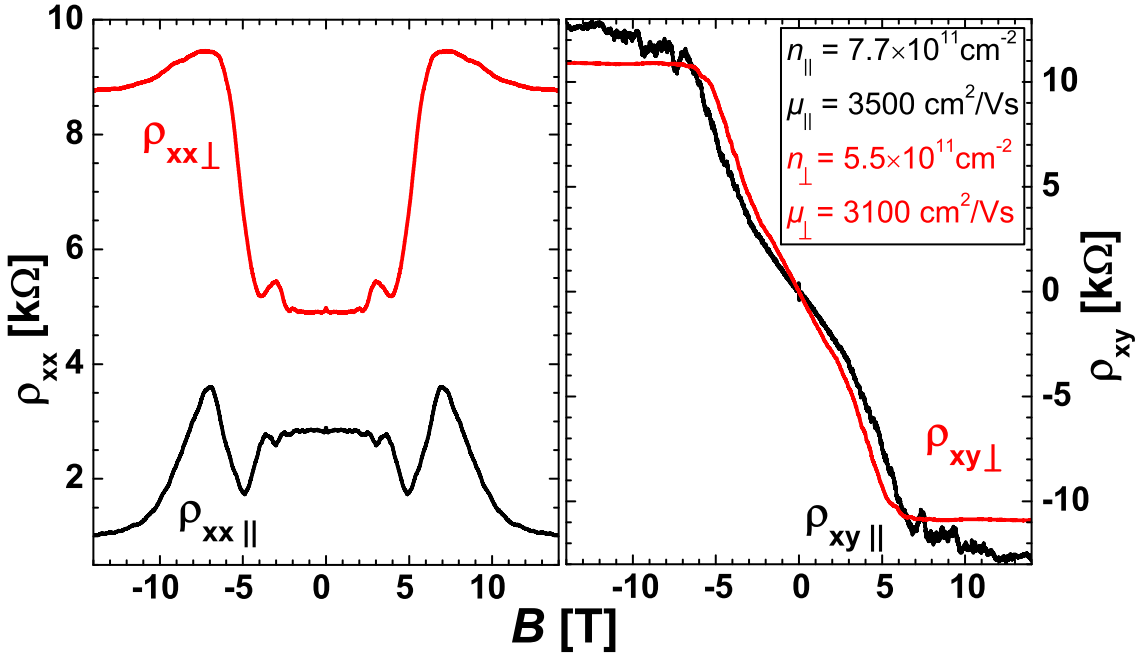

Figure 3.16: Longitudinal (ρ_{xx}) and Hall (ρ_{xy}) resistivity of graphene Hall bar structures aligned in parallel ($\parallel$) and perpendicular ($\perp$) to the surface terraces.

In both cases, the longitudinal resistivity shows several SdH oscillations, while the Hall resistivity exhibits only one distinguishable resistance plateau. Note that the Hall resistivity does not saturate at the predicted value of ∼12.9 kΩ, as expected for N = 0, but at a slightly lower value for $HB_\perp$. This might be caused by a mixing between conducting edge channels, which will be discussed later.

The most striking difference between the behavior of the samples is in the longitudinal resistivity at high magnetic fields. While $HB_\parallel$ shows the conventional quantum Hall effect with predominantly decreasing resistivity, $HB_\perp$ exhibits an increase in resistivity at high magnetic fields and disappearance of minima in the SdH oscillations. This is an unexpected anisotropic behavior for magnetotransport in graphene. It has to be stressed that this cannot simply be an effect of enhanced scattering, e.g. at defects at the step edges, since the zero magnetic field resistivity is not significantly affected. Therefore, the observed effect likely involves a phenomenon taking place in the vicinity of the step edges under the conditions of the QHE.

To further explore this behavior, additional structures with varying and larger Hall bar widths were investigated. For this purpose, L-shaped Hall bar structures were prepared on strongly stepped SiC substrates, as shown in Fig. 3.17. This L-shape was chosen in order to investigate both alignments (parallel and perpendicular to the substrate steps) in a single device. This excludes any influences of different processing environments.

The longitudinal resistivity, as measured on Hall bar structures with larger widths (between 5 and 20 µm) and lengths of 50 µm, aligned parallel and perpendicular to the terraces, are shown in Fig. 3.18. For the Hall bars aligned parallel to the step edges, no significant change is observed for the different HB widths [Fig. 3.18 (a)]. This is in contrast to the measurements in Hall bars aligned perpendicular to the surface steps [Fig. 3.18 (b)]. Here, a positive magnetoresistance can still be observed even for the Hall bars $HB_\perp$ with a width of 20 µm, but the effect is strongly reduced in comparison to what is measured

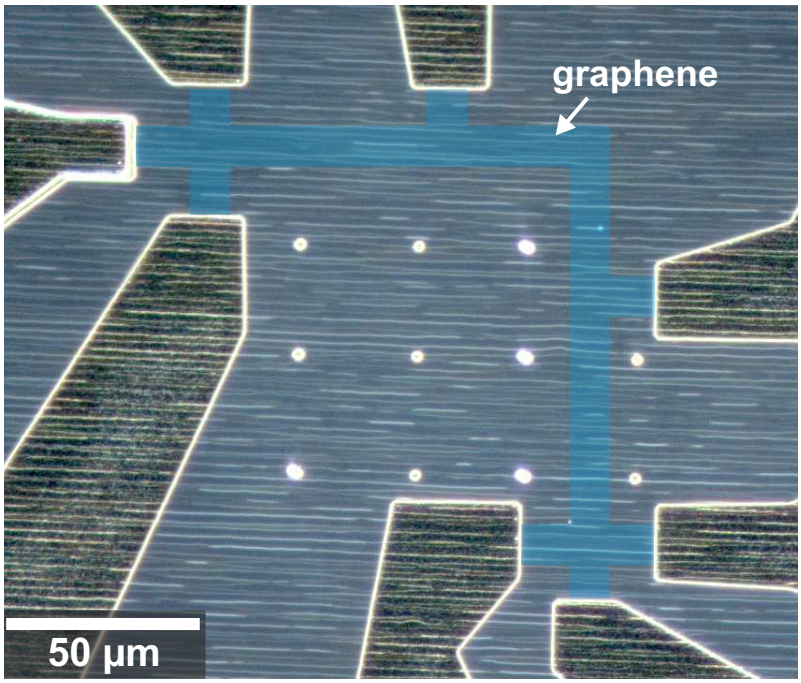

Figure 3.17: Optical micrograph of L-shaped Hall bars, prepared on a stepped SiC substrate. The position of the graphene HB is highlighted, its length and width are 50 and 10 µm, respectively. The surface steps manifest themself as bright horizontal lines in this image.

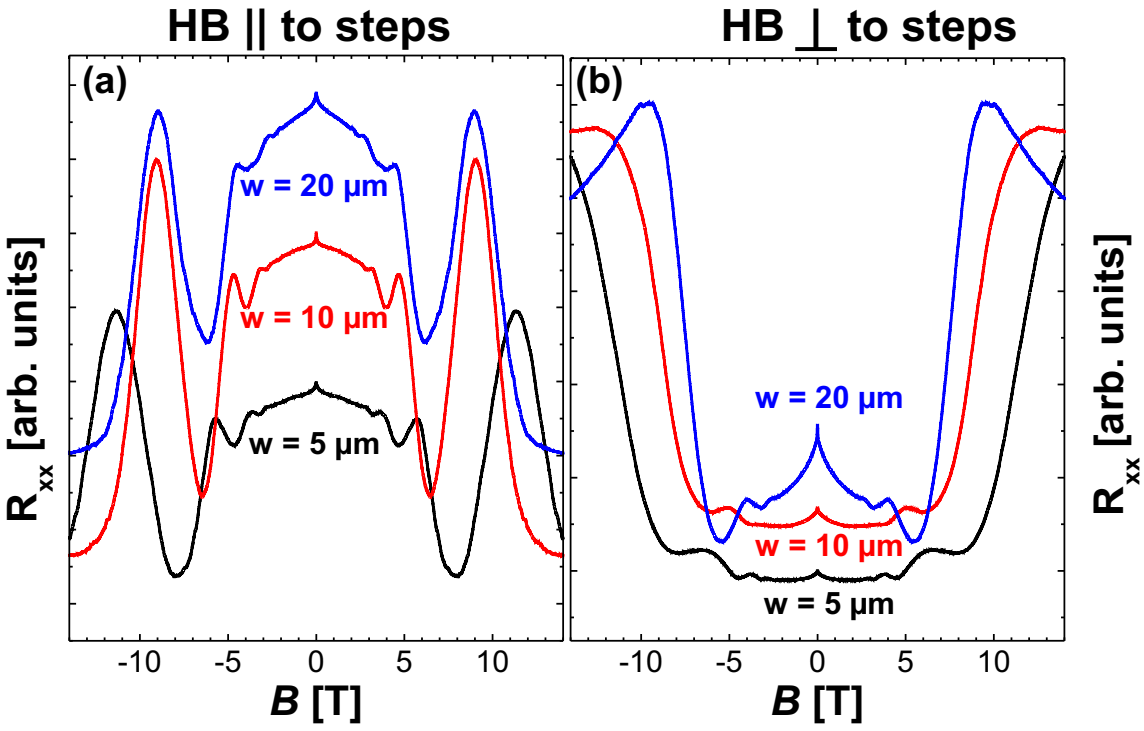

Figure 3.18: Magnetotransport measurements from Hall bars with varying widths. Only the longitudinal resistivity is shown for Hall bars aligned parallel (a) or perpendicular (b) to the terraces is shown. The curves have been scaled and shifted for better visibility.

for the 5 and 10 µm wide structures. In that case, $R_{xx\perp}$ presumably decreases in the minima of the SdH-oscillations (see Fig. 3.18) with increasing magnetic field. However, it does not approach zero in the measured B-field range, as in the case for Hall bars aligned parallel to the terraces.

We tentatively explain this behavior by considering the model illustrated in Fig. 3.19. The structure of the sample with the Hall bar in the region of a step edge is depicted in side view [Fig. 3.19 (a)] and top view [Fig. 3.19 (b)]. The illustration shows the monolayer graphene covering the surface continuously,[138] including the step edge regions where bilayer graphene has already been formed.[125] For simplicity, the underlying buffer layer is not depicted in Fig. 3.19 (a). In the conventional, relative simple understanding, the conductivity at high magnetic fields in the quantum Hall regime is governed by a low number of channels at both edges of the Hall bar (Landauer-Büttiker formalism).[139] The number of conductive channels is given by the filling factor[140] and is proportional to n/B.

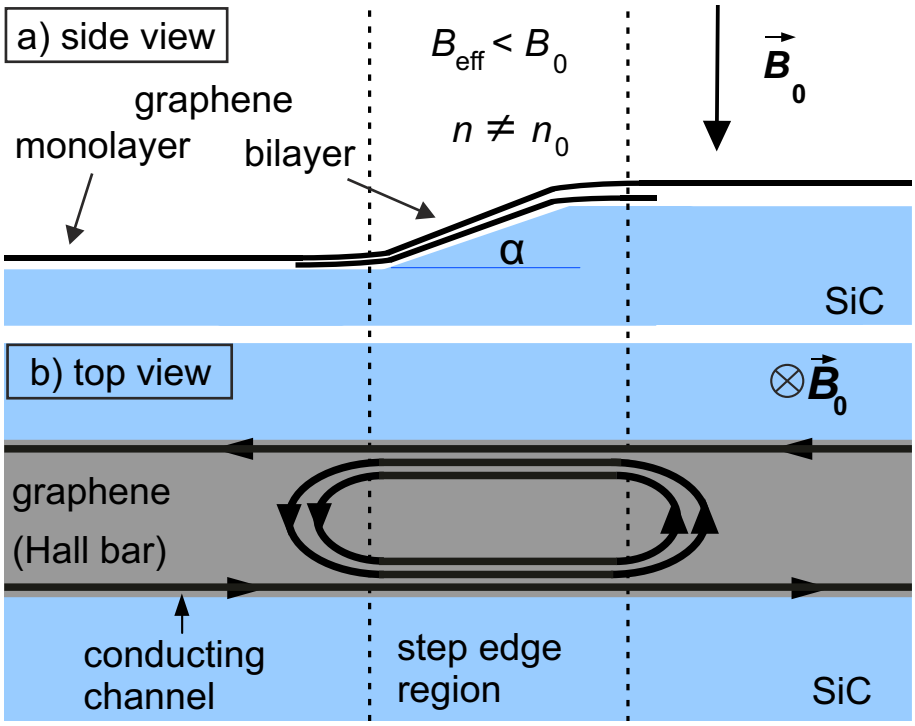

Figure 3.19: Model of magnetotransport in graphene for narrow Hall bars on stepped SiC surfaces in (a) side view and (b) top view.

Additional conductive channels may appear in the step edge regions of the Hall bar, corresponding to higher filling factors. One reason may be that the effective magnetic field (B_{eff}) is lower at the step edge region due to the tilted surface by a factor of $\cos(\alpha)$. The angle between the SiC(0001) surface and the $(1\bar{1}0n)$ step facet is $\sim 24-28°$ [46,138] which locally reduces B_{eff} to $\sim 0.9\,B_0$ and thus changes the spacing and width of the Landau levels. A second possible explanation could be differences in the carrier concentration between the step edges and terraces. The Raman line-scans along the Hall bars [see Fig. 3.15 (b) and (c)] support this interpretation, as the position of the G-line, which is known to be an indicator for carrier concentration,[141] strongly fluctuates for the $HB_\perp$

case [see Fig. 3.15 (c)]. Additionally, the existence of bilayer graphene in the step-edge-regions and different strain states may also play a role.

An alternative formalism which accurately describes the QHE is the screening theory of the QHE. It considers alternating compressible (metallic) and incompressible (insulating) strips which form at the edges of the Hall bar.[142,143] The concept is briefly summarized in Fig. 3.20. In Fig. 3.20 (a) – (c) the one-electron picture is again displayed. In Fig. 3.20 (b), the solid bold black line shows the potential for the electrons. Since the charge carriers are confined in the Hall bar, the potential bends up at the edges. The thin lines with circles represent the energetic positions of the Landau level, in which the electrons are condensed. They maintain their distance from each other ($\hbar\omega_c$) and the bare potential bends up the Landau levels. The position of the edge channels are given by the intersection of the LL with the constant Fermi energy E_F near the edges of the Hall bar.

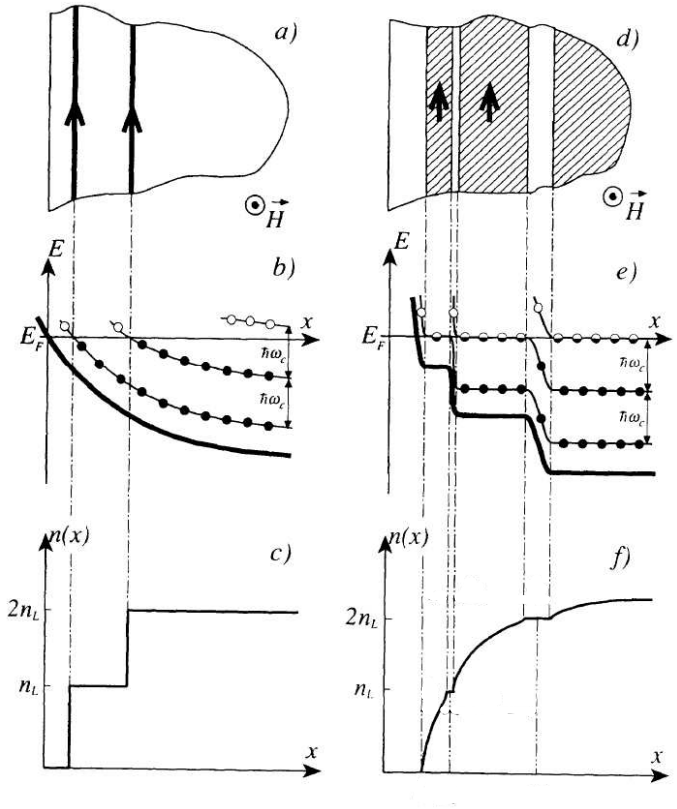

Figure 3.20: Structure of edge states in the integer quantum Hall regime in a one-electron picture [(a) - (c)] and the electrostatic picture with compressible (hatched) and incompressible (blanc) stripes [(d) - (e)]. (a)/(d) Respective top view of a 2DEG near the edge. (b)/(e) Energy of the LL/electrostatic energy. Filled circles represent locally occupied LL, blank circles locally empty LL and half-filled circles half-filled LL, respectively. (c)/(f) Electron density. The figure was adapted from [143].

In Fig. 3.20 (c) – (f) the electrostatic model is depicted. The electrostatic potential is not completely smooth because the electric field [in the x-direction, see Fig. 3.20 (d)] is completely screened in the compressible stripes, just like in a metal. The Hall potential only drops in between them, where the incompressible stripes are. Along these incompressible stripes the local conductivity vanishes because occupied and unoccupied states are

separated by an energy gap,[144] which is equivalent to the Landau quantization in the single electron picture. A similar situation is displayed in Fig. 3.21. Fig. 3.21 (a) shows the undisturbed case, with continuous edge channels. In Fig. 3.21 (b), the edge stripes are distorted by a barrier with reduced filling factor. This is opposite to the situation in our experiment, where the filling factor is likely higher in the step edge regions, but the principle is the same. The edge channels at different sites of the HB are no longer separated and backscattering of charge carrier occurs.

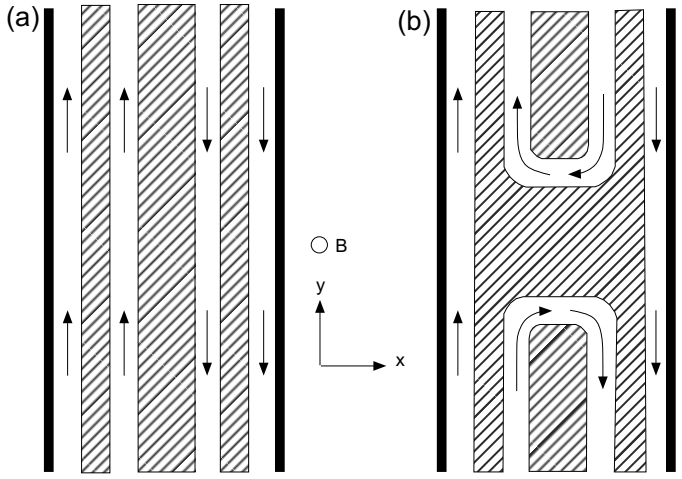

Figure 3.21: Schematic drawing of the (in)compressible stripes in (a) a uniform conductor and (b) a conductor containing a barrier of reduced filling factor. The figure was adapted from [142]

Now to connect the concept of (in)compressible stripes with the model for the anisotropic behavior shown in Fig. 3.19: the conditions for continuous edge states (stripes) are broken in the step edge region, which may be described as a change from incompressible to compressible stripes in the screening theory of the QHE. This is similar to the case of a gradient in the magnetic field. This effect (of breaking continuous edge stripes) even holds true for very small gradients in the magnetic field, similar to the case as described in Reference [145] (and references therein). Then, an interchannel scattering appears due to mixing of states which is denoted as circulating edge states in Fig. 3.19.

We thus illustrate backscattering to the opposite side of the HB due to inter-Landau level scattering, which becomes increasingly important in narrow samples where the spatial separation between the conducting channels at opposite edges of the HB is reduced. This gives rise to the positive magnetoresistance and the suppression of conductance minima of the QHE observed here.

Recently, additional theoretical calculations[146] have been conducted in which following situation was assumed: a narrow stripe of monolayer graphene is disrupted by a section of twisted bilayer graphene. This (partly) reflects the conditions of the experiments presented here, where bilayer graphene is present in the region of the surface step edges. Löfwander *et al.* concluded that 'the Hall plateaux are destroyed by the coupling between opposite edge states via transverse transport channels circulating around the bilayer perimeter'.[146] Their calculations are in agreement with our experimental findings and our model, even though the influence of the morphological tilt of the magnetic field in respect to the surface and the influence of different carrier densities at the step edges is still not completely clarified.

In contrast, the magnetotransport in Hall bars parallel to the steps behaves like monolayer graphene, even though it may be slightly distorted due to inhomogeneities in the structure.

3.3.3. Summary

In summary, we observe an anisotropic behavior in the magnetotransport properties of graphene in narrow Hall bars on stepped SiC(0001) surfaces. We propose a model to explain this behavior, which considers the opening of new conducting channels (i.e. higher filling factors) at both edges of the Hall bar in the surface region close to substrate steps. This is probably caused by a reduced effective magnetic field, an increased carrier density, a different strain state and/or the existence of BLG in the step edge regions which leads to inter-Landau level scattering, and results in enhanced backscattering and a positive magnetoresistance.

3.4. Investigation of the buffer layer, epitaxial graphene and intercalated bilayer graphene by grazing incidence X-ray diffraction

In this section, results from grazing incidence X-ray diffraction (GID) measurements are presented and discussed. Three different sample types were investigated: a buffer layer sample, an epitaxial graphene sample and a quasi-freestanding bilayer graphene sample (produced by oxygen intercalation of epitaxial graphene). First, experimental details are explained, followed by the presentation and discussion of results. Subsequently, possible explanations for the experimental observations will be discussed.

3.4.1. Experimental details

The samples were prepared in the RF-heated furnace, as described in Section 2.1. All samples were prepared on *n*-doped 6H-SiC(0001) substrates ($1 \times 1\,\mathrm{cm}^2$). A H-etching was performed, according to the procedure described in Section 3.1. The BL sample was synthesized at a temperature of 1400 °C, with an Ar pressure of 900 mbar and a flux of 100 sccm. The epitaxial graphene sample was prepared using the 'standard' parameters, described above. Also the bilayer graphene sample (BLG) was prepared in the furnace, using the same parameters to grow epitaxial monolayer graphene as the first step. Subsequently, an oxygen intercalation process was performed by thermally treating the sample in air for 40 min at 600 °C. During this process, oxygen atoms intercalate underneath the BL, breaking its covalent bonds with the SiC substrate. The BL thus converts into a second layer of graphene on an oxidized SiC surface. Since the resulting graphene only couples to the substrate via van der Waals forces, it is referred to as 'quasi-freestanding bilayer graphene'(QFBLG). Additional information on this process can be found in Reference [118]. The samples were investigated using Raman spectroscopy, AFM, and GID.

GID measurements were performed at the beamline ID10 of the ESRF. The primary beam energy was 10 keV and with an intensity of 10^{14} counts per second (cps). The angle of incidence was amounted to 0.15°, which is below the angle of total reflectance (0.21° for SiC). Raman spectra were recorded using an excitation wavelength of 482.5 nm with a spatial resolution of 1 μm.

3.4.2. Results and discussion

Raman spectra of the three types of samples (BL, EG, and BLG) are presented in Fig. 3.22. The Raman spectrum, recorded on the buffer layer, exhibits two intense and broad features in the spectral region of $1200-1600\,\mathrm{cm}^{-1}$, and a low-intensity, modulated bump at $2600-3000\,\mathrm{cm}^{-1}$. More information on the BL are given in Section 3.1.3 and in Reference [66].

The EG sample reveals the G-peak at $1581\pm5\,\mathrm{cm}^{-1}$ and the 2D-peak at $2724\pm10\,\mathrm{cm}^{-1}$, when measured on a surface terrace. The 2D-peak can be well fitted by a single Lorentzian, indicating that the graphene indeed consists of a single monolayer. The estimated error on the peak positions is extracted from the deviation of measurements taken at different positions on the sample. These variations can arise from different strain states and/or fluctuations in charge carrier concentration.[88,135,137] The strain in the graphene can be estimated from the 2D-peak position. The 2D-peak would be located at $2693\,\mathrm{cm}^{-1}$ (for the used excitation energy of 2.57 eV)[147] in case of unstrained graphene, and shifts

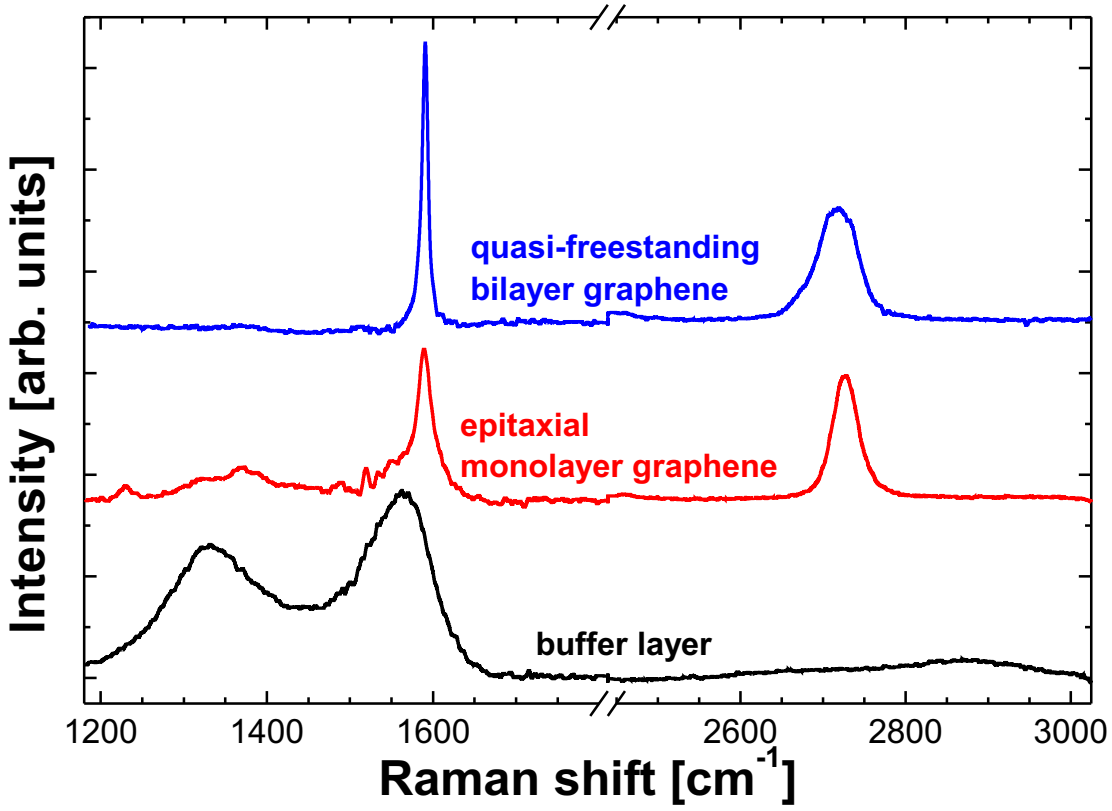

Figure 3.22: Raman spectra of a buffer layer, epitaxial monolayer graphene, and quasi-freestanding bilayer graphene. The spectra are vertically offset for better visibility.

by -140 cm^{-1}/% with strain. Therefore, the EG sample examined here is under compressive strain of $\epsilon \approx -0.2\,\%$.

The Raman spectrum collected after oxygen intercalation shows features of freestanding bilayer graphene. No features of the BL are observable in the spectrum. The absence of a D-peak proves the high structural quality of the graphene, with few or no defects. The 2D-peak is considerably broader than in case of EG and can be well fitted with four Lorentzians, indicating bilayer graphene.[84,85] The four components of the 2D-peak are positioned at 2673 cm^{-1}, 2688 cm^{-1}, 2706 cm^{-1}, and 2738 cm^{-1}, which coincide well with values given by Malard *et al.*[84] for flakes of exfoliated bilayer graphene. This indicates that the initial compressive strain of $\sim$0.2 % is released during the intercalation process. A further indication is that the variation in peak position is reduced with respect to the EG sample for measurements performed at different locations on the sample.

Representative AFM images of a BL, EG, and intercalated BLG sample are depicted in Fig. 3.23. The morphology of all samples is similar, and the surface consists of terraces and steps in between them. Most terraces in the BL are narrower compared to the other two samples, which indicates that the step bunching process is less pronounced for this process, likely due to the lower synthesis temperatures. Comparing Fig. 3.23 (b) and (c), the morphology does not change during the intercalation process. In particular no wrinkles appear on the surface, which could be related with a strain relieve process.

The structure of the samples was investigated by GID. Using this technique, the lattices planes orthogonal to the sample surface normal are analyzed by diffraction, and infor-

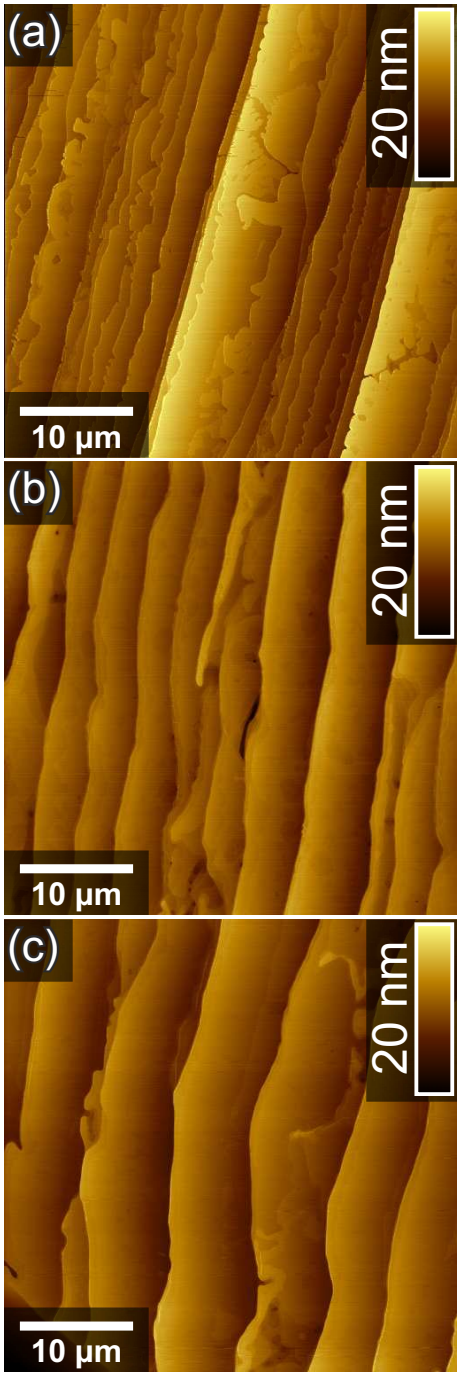

Figure 3.23: AFM images of (a) BL, (b) EG, and (c) intercalated BLG.

mation about in-plane lattice parameter and orientation can be acquired. By rotating the sample with respect to the incident beam while holding the detector position fixed, a so-called angular scan is performed. This scan provides a curved line, $\mathbf{q_a}$, in reciprocal space where every point on the curve has the same distance to the origin (0000) (i.e., the length of the scattering vector is fixed). By varying the azimuthal angle of detection and rotating the sample in a 2:1 ratio, a radial scan along $\mathbf{q_r}$ is obtained, which corresponds to

a Θ–2Θ scan. In the experiment presented here, *reciprocal space maps* (RSM) were recorded by combining angular and radial scans.

RSM for all three sample types (BL, EG, and BLG) are displayed in Fig. 3.24. Two SiC-related reflections are present, the SiC($2\bar{1}\bar{1}0$) and the (forbidden) SiC($2\bar{2}00$) reflection. These were used to calibrate the measurement, i.e. adjust the angles so that the measured substrate reflections coincide with the literature values. Two graphene related reflections were recorded in these measurements,[a] the G($10\bar{1}0$) and the G($11\bar{2}0$) reflections. The RSM of the three samples share common characteristics. The graphene reflections are single, isolated peaks, which shows that the films possess a single orientation with respect to the substrate without rotational disorder. The graphene lattice is rotated by 30° with respect to the SiC, since the (equivalent) ($2\bar{1}\bar{1}0$) and ($11\bar{2}0$) SiC and graphene reflections are rotated by this angle relative to each other. No differences in the structure of the samples could be determined from these RSM, due to their low resolution.

To measure the lattice constants of the graphene films, line scans over the G($11\bar{2}0$) reflection were performed with higher resolution along $\mathbf{q_r}$, as shown in Fig. 3.25. The central position of the peaks was determined by fitting Gaussians to the curves. The error is estimated conservatively to be ∼0.001 Å, based on the error of the fitting, the energy resolution of the primary beam, the accuracy of the motors which move the sample and the detector, and the alignment of the substrate related peaks to their literature values.[148]

These measurement reveal differences between the samples. The buffer layer (green curve in Fig. 3.25) shows a lattice constant of a = 2.4670 Å. The G($11\bar{2}0$) reflection of epitaxial graphene (red curve in Fig. 3.25) shows splitting, and can be well fit with two Gaussian peaks, centered at 2.4626 Å and 2.4556 Å. The reflection obtained from BLG (blue curve in Fig. 3.25) again consists of a single Gaussian, with a lattice constant of a = 2.4605 Å.

The measured lattice constant of the BL is ∼0.24 % larger (tensile strained) in comparison with bulk graphite (a = 2.461Å).[20] This difference is likely due to the fact that the BL is a surface reconstruction of SiC, and about 1/3 of its C atoms are in an sp^3-configuration, convalently bound to the SiC surface. Its structure is therefore different from that of graphite, possibly explaining the difference in lattice constants.

We examine the structure of the EG samples to determine the origin of the doublet in diffraction from these films. The graphene layer is situated on top of a BL, which is partially bound to the SiC substrate. Since ∼1/3 of the C atoms in the BL are in sp^3-configuration, it is plausible that the graphene and the BL possess different lattice constants. We assign the peak at larger lattice constant (a = 2.4626 Å) to the BL underneath the graphene, and the peak at smaller lattice constant (a = 2.4556 Å) to the graphene layer. The lattice constant of the graphene layer is ∼0.22 % smaller in comparison to unstrained graphite, i.e. it is compressively strained (ϵ = –0.22 %). This value agrees well with the strain estimated by Raman spectroscopy (ϵ = –0.2 %). This strain may arise from different coefficient of thermal expansion for graphene and SiC. Graphene's coefficient is negative (it expands when cooled down),[149] while the coefficient of SiC is positive (it shrinks during cooling).[150] Since the growth of epitaxial graphene is performed at high temperatures, this compressive strain in EG may arise during cooling to room temperature. For this contraction of the graphene lattice to be caused by the SiC substrate, the graphene layer must be pinned firmly to the substrate. Otherwise, stress in the EG could be released by formation of wrinkles, as is observed in graphene grown on C-face SiC (see

[a] The buffer layer related reflections are labeled same as graphene's reflections, since its structure is isomorphic to graphene.

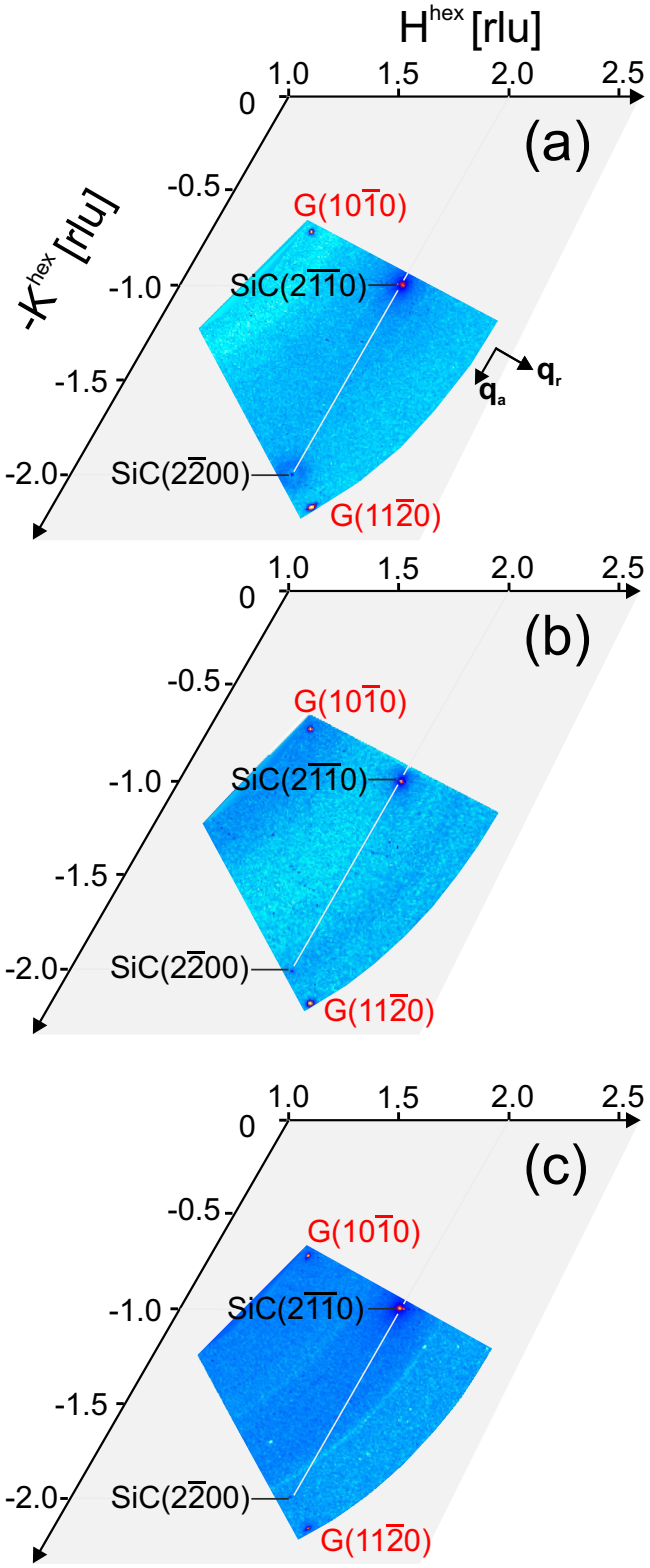

Figure 3.24: Reciprocal space maps of (a) buffer layer, (b) epitaxial monolayer graphene, and (c) intercalated bilayer graphene. The axes are scaled with the reciprocal lattice units (rlu) of SiC, $\mathbf{q_a}$ and $\mathbf{q_r}$ mark the radial and angular directions in the RSM.

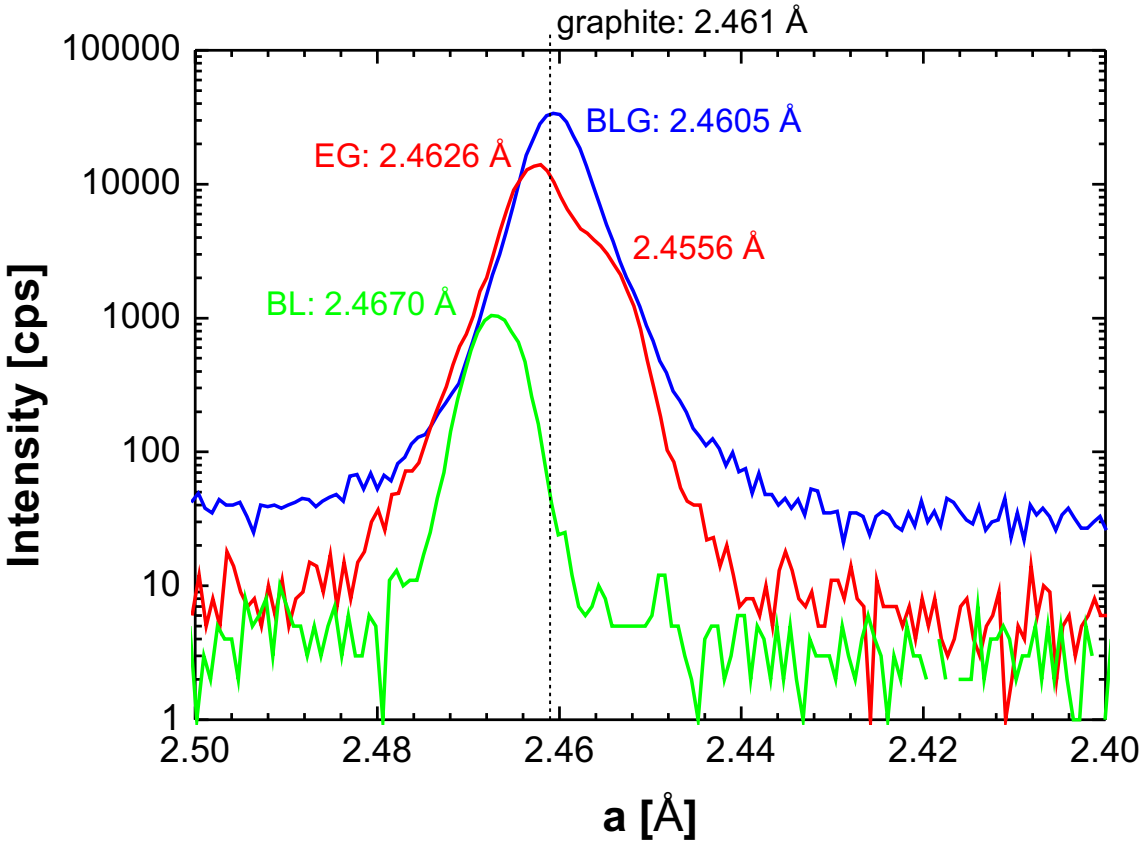

Figure 3.25: Linescans through the G(11$\bar{2}$0) reflection along $\mathbf{q_r}$, performed for the buffer layer (green), epitaxial monolayer graphene (red), and intercalated bilayer graphene (blue). The numbers denote the central position of the peaks, the dotted line indicates the value of the lattice constant of graphite.[20] The x-axis is scaled to the lattice constant of graphene.

Section 3.5). It is currently unknown whether van der Waals forces alone are sufficient to prevent such corrugations. It is also possible that a small number of defects exist in the graphene, which bond covalently to the BL, and therefore also pinned to the substrate. Another reason for the smaller lattice constant might be corrugations in the graphene layer. With GID, only the projected in-plane lattice parameter can be determined. In the possible case of highly curved graphene sheets, this might appear smaller if it possesses a considerable extension in the out-of-plane direction. However, since Raman spectroscopy measurements lead to a similar strain as GID measurements, the argument of corrugation is concidered unlikely.

Another interesting fact is that the BL underneath the EG possesses a smaller lattice constant than bare BL on SiC. The reason for this remains unclear at the moment, but there are some possible explanations for this observation. A reason for this difference might be the different growth environments for the two buffer layers. The first BL grows at the SiC-Ar interface, while for the EG sample the BL grows underneath the 'old' BL (which is transformed into a graphene layer during this process). The sublimating Si atoms have to move through the BL during the growth, and therefore stay longer in contact with the surface, which may influence the growth. Also the existence of the graphene layer on top could influence the growth of the BL, e.g. during the cool-down process after

growth. Weng *et al.*[151] have reported similar results obtained from TEM investigations. They assert that the $6\sqrt{3}$–reconstruction does not persist at the interface during the EG growth, but it has a different structure. No further explanation of the nature of the interface layer was given.

The linescan over the G($11\bar{2}0$) reflection of the quasi-freestanding bilayer graphene sample again shows a single peak, centered at 2.4605 Å. The appearance of a single peak shows that both graphene layers posses the same lattice constant, the former BL slightly contracts while the the EG layer expands. The difference relative to the literature value of graphite is 0.02 %; the graphene layers are therefore basically unstrained. This is in agreement with results obtained from Raman spectroscopy. During the oxygen intercalation process, the BL detaches from the substrate and converts into a graphene layer. Thereby, the strain in the BL, as well as in the original graphene layer is released, resulting in unstrained BLG.

3.4.3. Summary

The lattice constants of BL, EG, and BLG have been measured with high precision by GID. The BL, which forms first on SiC, possesses a lattice constant of 2.467 Å which is higher than that of graphite. EG is under a tensile strain of $\epsilon \approx -0.22$ %, while the BL under the graphene layer possesses a lattice constant which is considerably higher than the one of the bare BL. Upon oxygen intercalation by annealing in air, the EG is transformed into quasi-freestanding BLG, and the strain is released. The strain in the EG is likely due to the different termal expansion coefficients of the graphene and the SiC substrate. However, the origin of the different lattice parameter of the BLs remains unknown.

3.5. Growth of epitaxial graphene on C-face SiC by surface Si depletion

So far, only the growth of epitaxial graphene on Si-face SiC was presented and discussed. Epitaxial graphene can also be prepared on the C-face of SiC, but it is more difficult to achieve homogeneous growth of mono- or few-layer graphene on this face. However, multilayer EG on C-face SiC has been shown to behave like monolayer graphene, with linear band dispersion at the Dirac points, and the associated high charge carrier mobilities. This behavior is attributed to electronic decoupling of the different graphene layers, which is caused by rotational stacking faults between adjacent graphene layers.[152] In this section, a growth study is presented which aims to more systematically investigate the influences of different growth parameters.

Growth was investigated in three different environments: in an Ar atmosphere, in high vacuum ($\sim 10^{-5}$ mbar), and with the SiC enclosed in a confined space ('confinement controlled sublimation', CCS). The latter is inspired by the work of de Heer *et al.*,[153] who assert that they are able to produce continuous, homogeneous, large-area, monolayer graphene on C-face SiC that has a high carrier mobility. The essence of the idea is that Si atoms which desorb from the substrate stay in the vicinity, and therefore increase the local Si vapor pressure. Therefore, the rate of Si depletion is decreased and higher substrate temperatures can be employed; a similar argument as for the use of an Ar atmosphere for growing EG on Si-face SiC (see Section 3.1.2).

3.5.1. Experimental details

Growth was carried out in the same RF-heated furnace as described in Section 2.1. A H-etching was not performed in this study, since the etching process resulted in deep pits in the sample surface, and no differences could be detected between growth on etched and non-etched samples. The same substrate holder was employed as in the case of growth on Si-face, but for the CCS process a graphite cap with a volume of $\sim 1\,\mathrm{cm}^3$ was placed above the SiC. The cap possesses a small orifice (0.75 mm in diameter, see Fig. 3.26), so that some Si atoms can escape the confinement and the Si vapor pressure is not steadily

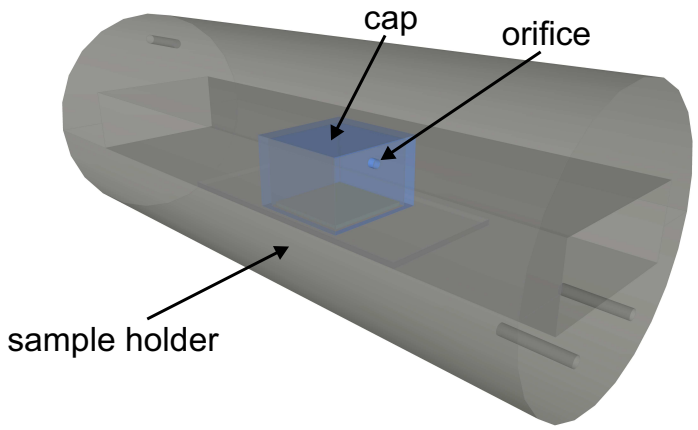

Figure 3.26: Scheme of the sample holder employed for the synthesis of epitaxial graphene. Here, the sample is covered with a carbon capping containing a small orifice, which is used for the 'confinement controlled sublimation' method.

increasing during the growth process. The $1 \times 1\,\mathrm{cm}^2$ samples were chemically cleaned under ultrasonication in n-butylacetat, acetone, and isopropanol, followed by a DI-water dip. Subsequently, the samples were loaded into the reactor and annealed in vacuum at 800 °C for 10 min in order to desorb contaminants from the surface. In the case of growth in vacuum, the sample was then heated to the process temperature. For growth in Ar, the furnace is filled with Ar to a pressure of 900 mbar with a flux of 500 sccm, and subsequently heated up. After the process ended, the sample cooled down to room temperature and could be unloaded for *ex-situ* investigations. The temperatures were varied between 1100 °C and 1600 °C, with growth times between 15 min and 60 min.

The samples were investigated by optical microscopy (OM), atomic force microscopy, Raman spectroscopy, and magnetotransport measurements.

3.5.2. Results and discussion

Epitaxial graphene on C-face SiC was prepared in three different environments, which will be addressed separately.

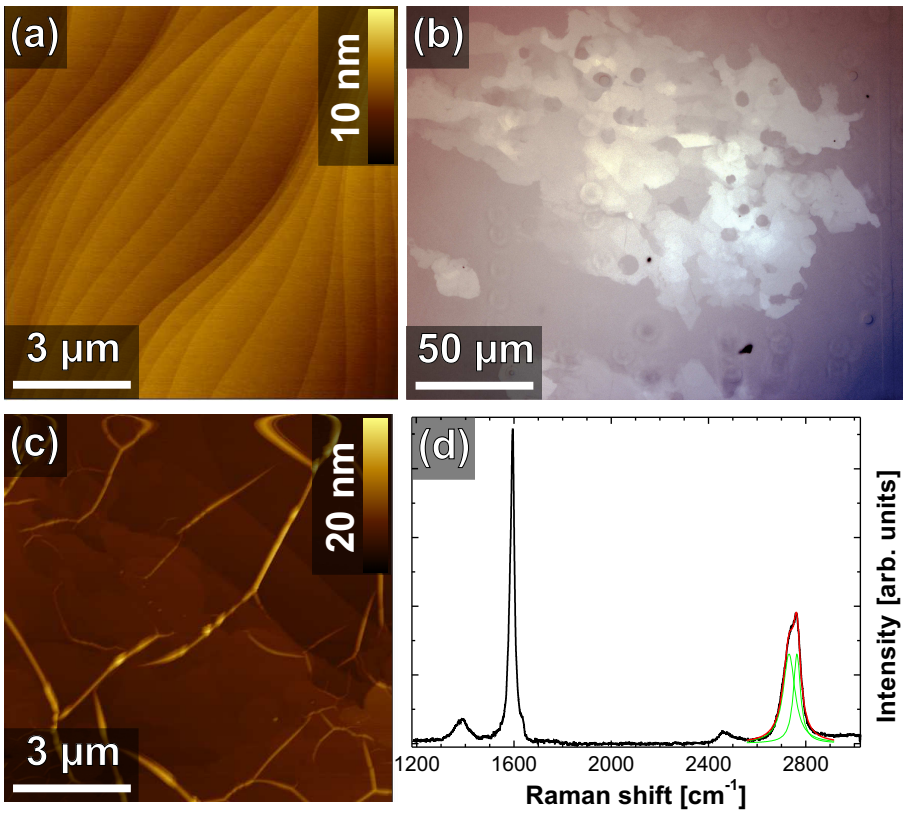

Figure 3.27: Epitaxial graphene on C-face SiC, synthesized in an Ar atmosphere. (a) AFM image of a sample grown at 1500 °C, (b) and (c) optical and atomic force micrograph of a sample grown at 1600 °C, and (d) Raman spectrum, taken from a graphene island, grown at 1600 °C.

Growth in Ar

Three samples were synthesized in an Ar atmosphere with a growth time (Δt) of 15 min and at 1400 °C, 1500 °C, and 1600 °C. At 1400 and 1500 °C, no graphene was formed at the surface, see Fig. 3.27 (a). At a temperature of 1600 °C, islands of graphene are observable on the SiC surface [Fig. 3.27 (b)], although the complete surface is not covered. These islands consist of multilayer graphene, in accordance with the observations by Tedesco *et al.*[154], and Luxi *et al.*[155]. The graphene shows wrinkles at its surface [Fig. 3.27 (c)], which likely originate from strain release during cooling from the growth temperature, since SiC has a positive thermal expansion coefficient, while graphene's is negative (see Section 3.4).

A Raman spectrum, taken from a graphene island (T = 1600 °C), is presented in Fig. 3.27 (d). It shows an intense G- and 2D-peak, as well as a low-intensity D-peak. Therefore, some defects are present in the graphene film. Interestingly, the 2D-peak splits into two components, which will be discussed in detail later. The intensity of the Raman signals vary strongly, depending on the position on the graphene islands. This means that the number of layers is non-uniform, which is also reflected in the intensity ratios of the G- and 2D-peaks. Thin layers have a high 2D/G ratio, while this ratio is smaller for multilayer graphene. Overall, synthesis in an Ar environment seems to to unsuitable for the production of uniform epitaxial graphene on C-face SiC.

Growth in vacuum

The situation for samples prepared in vacuum is rather different. The substrate is completely covered with graphene, and the films are homogeneous, as shown by AFM and Raman spectroscopy. But the graphene possesses a rough surface, similar to the case of EG on Si-face SiC synthesized in vacuum [see Section 3.1.2, Fig. 3.5 (a)]. Representative AFM images of samples grown at 1250 °C and 1450 °C are shown in Fig. 3.28. The sample prepared at the lower temperature shows a smoother surface (RMS roughness of 2.2 Å) than the graphene synthesized at 1450 °C (RMS roughness of 17 Å). The reason for this is not an inferior quality of graphene (see Raman results below), but rather the faster rate of SiC decomposition.

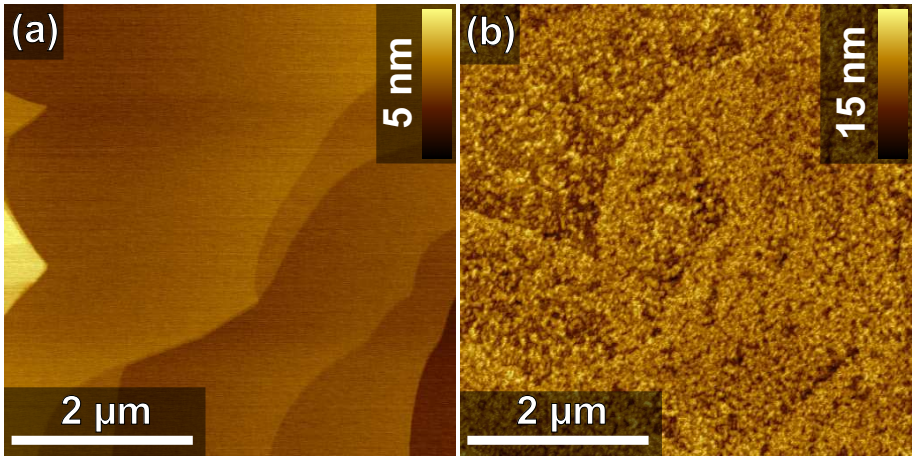

Figure 3.28: AFM images of EG prepared in vacuum in C-face SiC at (a) 1250 °C, and (b) 1400 °C.

All samples have been investigated with Raman spectroscopy. Two representative spectra, taken from samples whose AFM images are depicted in Fig. 3.28 (a) and (b), are shown in Fig. 3.29 (a) and (b), respectively. In both spectra, the D-, G-, and 2D-peaks are present, proving the presence of defective graphene. With increasing growth temperature, the relative intensity of the D-peak decreases and the intensity of the 2D-peak increases. The shape of the 2D-peak is symmetric, and can be well fitted by a single Lorentzian. This implies that the graphene layers behave like isolated sheets, the band structure at K and K′ still resembles Dirac cones, and the stacking of adjacent graphene layers is likely disordered.[156]

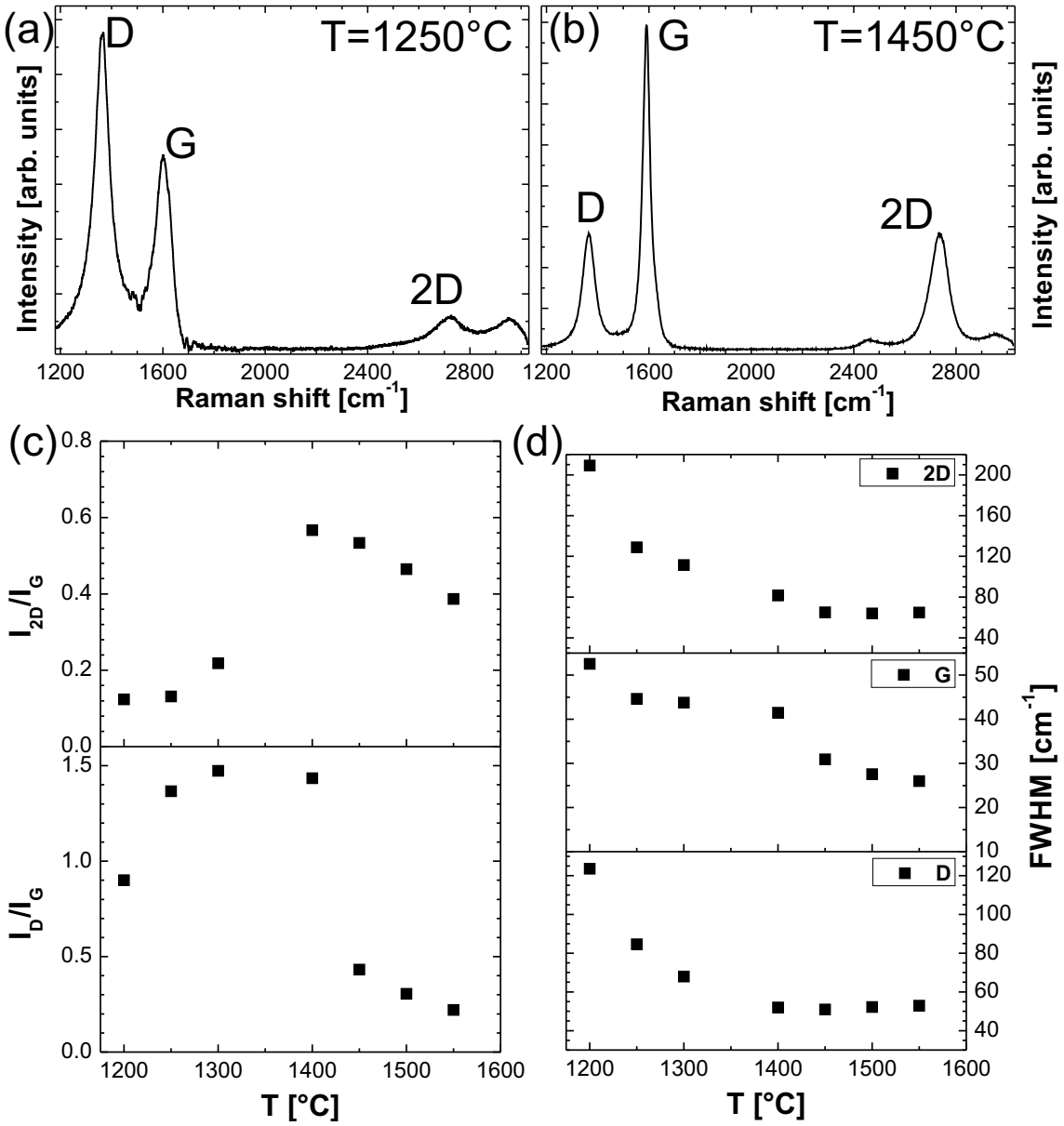

Figure 3.29: Raman spectra of graphene samples synthesized in vacuum on C-face SiC at (a) 1250 °C, and (b) 1450 °C. The SiC background was subtracted. (c) shows the intensity ratios I_{2D}/I_G and I_D/I_G, (d) the FWHM of the 2D-, G-, and D-peak of samples grown at different temperatures.

Parameters for the intensity ratios and FWHM of the peaks were extracted by fitting Lorentzians to the spectra, and these are depicted in Fig. 3.29 (c) and (d). The intensity ratio I_{2D}/I_G increases up to a temperature of 1400 °C and then decreases again slightly. I_D/I_G also first increases and then rapidly decreases by a factor of 3 for samples grown at at temperatures above 1450 °C. The widths of the D- and 2D peak first decrease when the temperature is increased and reach a minimum at 1450 °C and stay constant upon further increases in synthesis temperature. The FWHM of the G-peak monotonously decreases with increasing temperature. Therefore, the structural quality of the graphene layers initially increases with increasing temperature up to ∼1450 °C. If the temperature is increased further, the density of defects decreases further (as indicated by the decrease of I_D/I_G). However, since the I_{2D}/I_G decreases above these temperatures, this might be due to C atoms which are not in an sp^2-configuration, or which do not form hexagonal C rings. At temperatures above 1450 °C the decomposition rate of SiC continues to increase, but the structural quality of the graphene layers already reached the optimum level.

The electrical characteristics of the samples were investigated using room temperature magnetotransport measurements. Reliable measurements could only be obtained for samples synthesized at temperatures above 1400 °C. The results are presented in Fig. 3.30. Films are *p*-doped,and the carrier density decreases from $\sim 3 \cdot 10^{14}\,\mathrm{cm}^{-2}$ for T = 1450 °C to $\sim 3 \cdot 10^{13}\,\mathrm{cm}^{-2}$ for T = 1500 °C and T = 1550 °C. Simultaneously, the carrier mobility increases from $10\,\mathrm{cm}^2/\mathrm{Vs}$ (T = 1450 °C) to $110\,\mathrm{cm}^2/\mathrm{Vs}$ (T = 1500 °C) and $250\,\mathrm{cm}^2/\mathrm{Vs}$

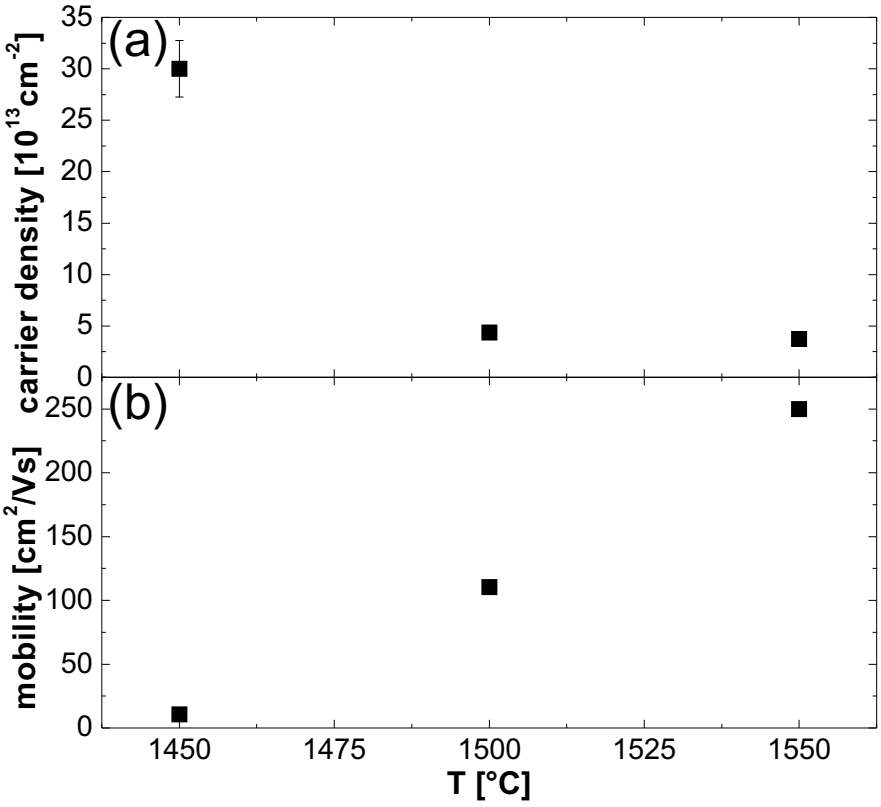

Figure 3.30: (a) Charge carrier density (*p*-type) and (b) mobility of EG on C-face SiC synthesized in vacuum. The values were determined by magnetotransport measurements in van-der-Pauw geometry, performed at room temperature.

(T = 1550 °C). The quality of the graphene with respect to electrical transport properties therefore increases with increasing growth temperature.

Together with the Raman spectroscopy measurements, these results imply that a temperature of 1450 °C is needed to grow a complete conducting layer of graphene on C-face SiC at a growth time of 15 min. Further increases in temperature yield improved transport properties, but the thickness and the surface roughness of the graphene also increases. The improvement in quality is not clearly reflected by the results of the Raman measurements.

Growth in a confinement

The last method addressed here is CCS. A single cap was used, which has an orifice with a diameter of 0.75 mm located at one side of the cap. Samples were prepared at different temperatures (T = 1400 °C – 1600 °C) and for different growth times (Δt = 15 – 60 min).

At high temperatures and short growth times, the resulting graphene layers are similar to the ones synthesized in Ar. Isolated islands of graphene with different thicknesses partially cover the surface and do not combine to form a complete, homogeneous film. If the growth time is increased at a fixed temperature, the coverage of the surface increases. However, the number of layers varies significantly. At lower growth temperatures, the process happens more slowly and in a more homogeneous way. Representative optical micrographs of a sample grown at 1500 °C (Δt = 30 min) and at 1450 °C (Δt = 60 min) are shown in Fig. 3.31.

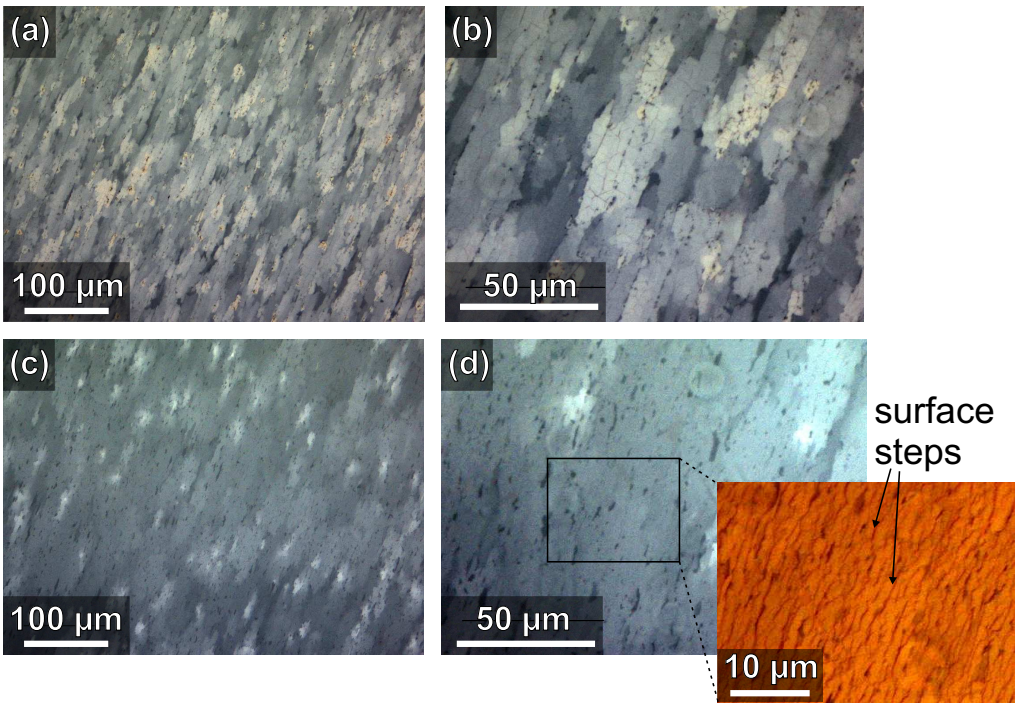

Figure 3.31: Optical micrographs of graphene grown on C-face SiC in a containment (a),(b) at 1550 °C for 30 min, and (c),(d) at 1450 °C for 60 min. The inset in (d) shows a close-up image, taken with an interference filter, where surface steps are clearly visible.

The sample synthesized at higher temperature and shorter growth time [Fig. 3.31 (a) and (b)] exhibits a distribution of graphene with different thicknesses, which manifests itself with different contrasts in the optical micrograph. The areas of uniform thickness have dimensions on the order of tens of µm. Also, the sample prepared at T = 1450 °C for 60 min is not completely homogeneous. Nevertheless, the areas with uniform coverage are considerably larger (>50 µm). The continuous graphene sheet, with no visible change in thickness, covers several surface steps [see inset of Fig. 3.31 (d)]. Overall – also taken the samples into account which are not explicitly discussed here – more uniform graphene sheets can be grown if the temperature is lowered and the growth time is increased. At higher temperatures, the growth of additional graphene layers commences rather quickly while their growth in lateral direction is comparatively slow. At lower temperatures, the relative lateral growth rate (in respect to the growth of additional graphene layers) is higher, therefore larger and more uniform graphene islands grow.

Selected AFM images of two distinct samples, grown at 1500 °C for 30 min and at 1400 °C for 60 min, are shown in Fig. 3.32. Fig. 3.32 (a) displays the height image, taken on a 'thick' flake. Wrinkles are visible on the surface, similar to the case of growth in Ar. A surface plot along the dotted line in (a) is presented in Fig. 3.32 (b). It reveals that the

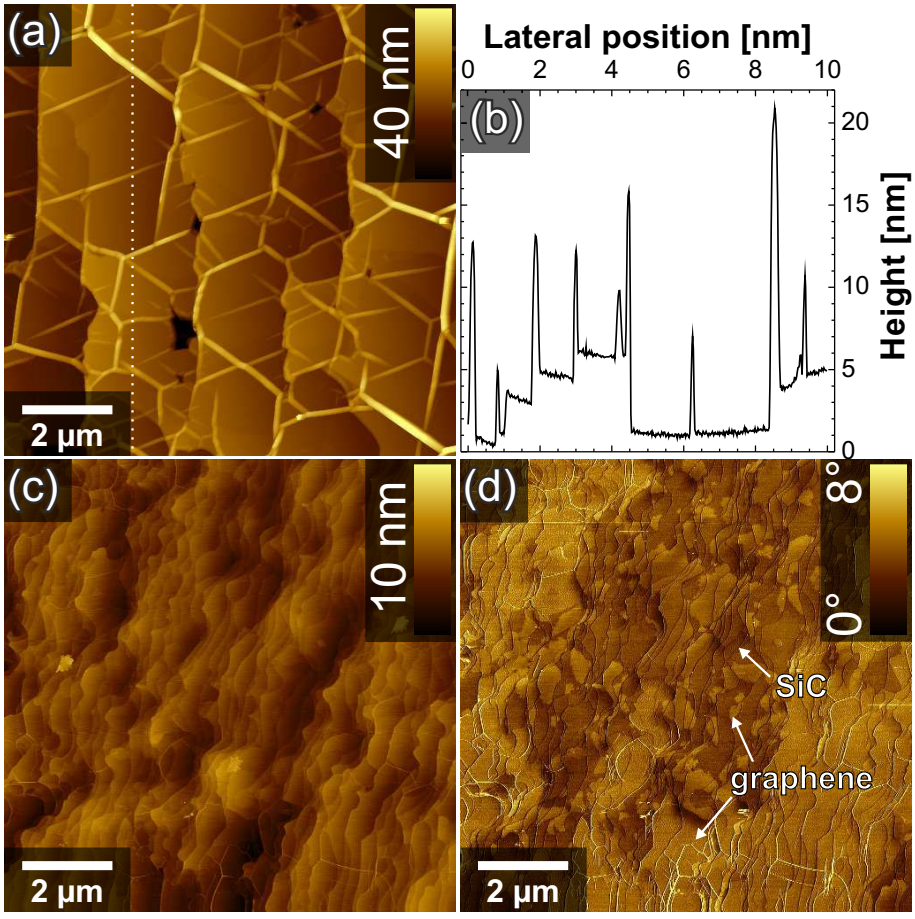

Figure 3.32: AFM image of samples grown on C-face SiC in a confined space. (a) Sample grown at 1500 °C for 30 min, and (b) a surface profile according to the dotted line in (a). (c) and (d) depict the same area of the surface of a sample synthesized at 1400 °C for 60 min. (c) shows a height image and (d) a phase contrast image.

height of the wrinkles ranges from 5 nm to 20 nm. The origin of the wrinkles is likely the same as in case of growth in an Ar atmosphere, that is, strain release during cooling the sample.

Fig. 3.32 (c) and (d) show the same area of a sample grown at 1400 °C for 60 min. In (c), an height image is depicted, while a phase contrast image[157] is shown in (d). The brighter areas in (d) correspond to graphene, while the darker areas correspond to exposed SiC surfaces. Expanded sheets of graphene are present on the surface, e.g. in the lower right part of Fig. 3.32. In this region, wrinkles are also present in the graphene layers. However, small patches of graphene, with diameters below 1 µm, also exist on the SiC substrate. This shows that the thin islands nucleate separately on the surface, and these small islands do not show wrinkles.

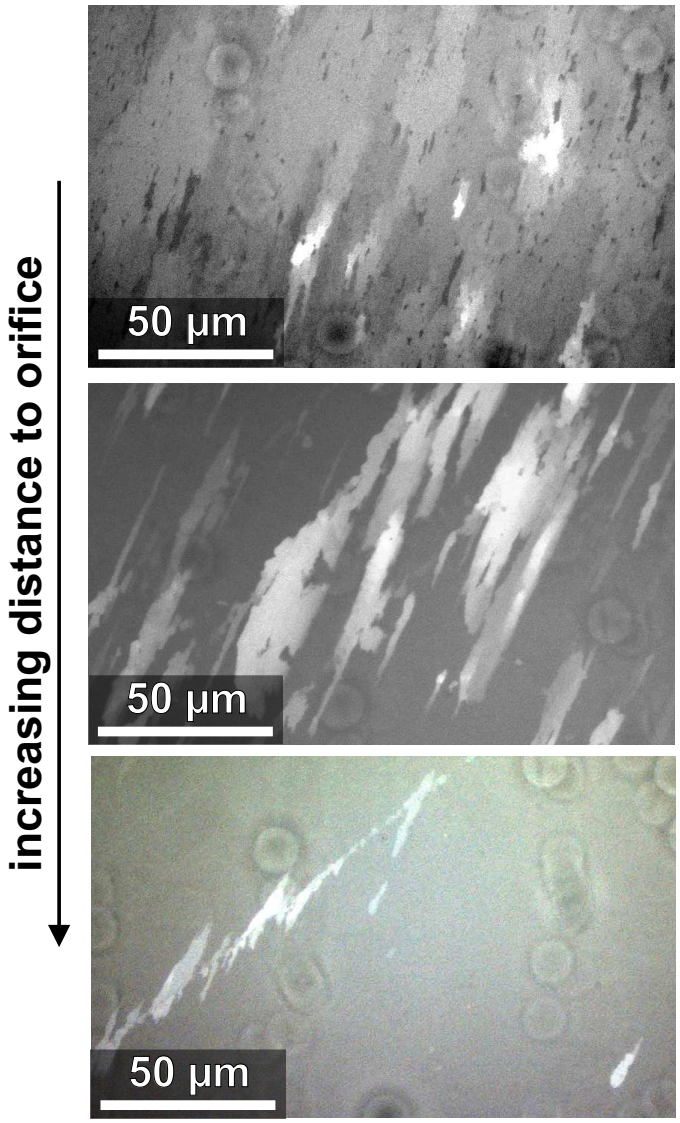

Figure 3.33: Optical micrographs of graphene grown on C-face SiC in a confined volume with different distances to the orifice in the capping. The circular structures in the images are artifacts from the microscope.

Since the orifice in the cap is located at one side (see Fig. 3.26), the growth of graphene changes along the substrate. In Fig. 3.33, three OM images are depicted, taken near the orifice, in the center of the sample, and at the side opposite from the orifice. The graphene coverage decreases with increasing distance to the orifice. The reason is the variation in Si vapor pressure inside the confinement. Near to the orifice, the probability of Si atoms leaving the confinement is larger than in areas further away from the orifice. For growth of graphene which is uniform across the complete substrate, the cap has to be modified to yield a homogeneous Si pressure in the complete confinement. A possible approach is to include multiple orifices, each with a smaller diameter.

The structural quality of the graphene produced by this method has been investigated by Raman spectroscopy. Spectra obtained from two samples are presented in Fig. 3.34. One Raman spectrum was recorded on a 'thick island', and the other at a 'thin island'. The samples were prepared at 1500 °C for 30 min (a), and at 1400 °C for 60 min (b). The spectra obtained from the two samples are rather similar. Only a weak D-peak is observable in each spectrum, indicating the high structural quality of the graphene. The spectra taken from a thin island show, for both samples, characteristics of monolayer graphene, with a symmetric 2D-peak with an intensity higher than that of the G-peak. It should be noted, that the 'thin island' also consists of more than one layer of graphene, as indicated by optical microscopy. This is in agreement with the observations of de Heer *et al.* who

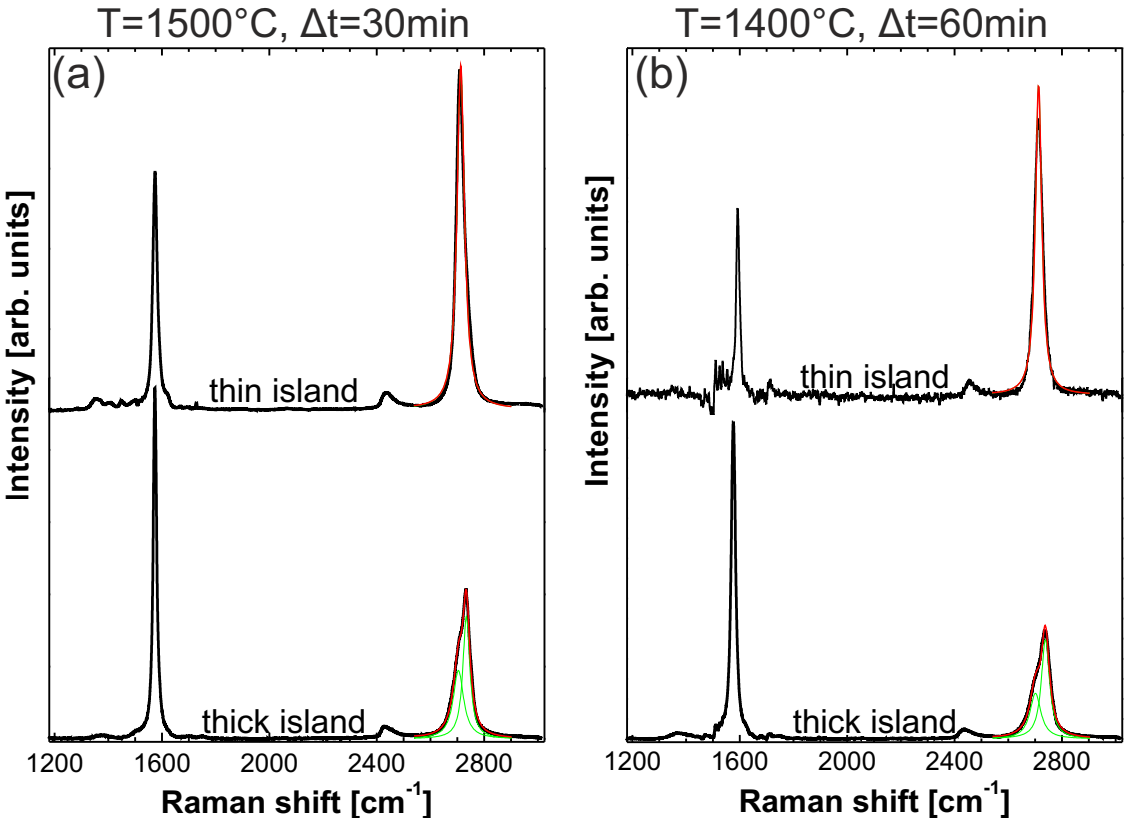

Figure 3.34: Raman spectra of epitaxial graphene on C-face SiC, prepared in a confinement (a) at 1500 °C for 30 min, and (b) at 1400 °C for 60 min. One spectrum, taken at a thick and at a thin island, are displayed each. The SiC background was subtracted from the spectra.

claim that multilayer graphene grown on C-face SiC behaves like monolayer graphene due to rotational stacking faults between adjacent layers.[152,158]

In contrast, the Raman spectra obtained from thick flakes do not show the characteristics of MLG. The 2D-peak splits, and can only be fitted by two Lorentzians. Additionally, the intensity of the G-peak is approximately two times higher than the intensity of the 2D-peak. One reason for the splitting of the 2D-peak might be that different layers of graphene possess different properties, so that the splitting of the 2D peak arises from a superposition of detuned Raman modes from different graphene layers. However, since the G-peak does not show such splitting, this explanation is unlikely.

Rather, these observations suggest that the graphene layers posses an ordered stacking, such as graphitic AB-stacking. It is interesting that this behavior only appears in islands with many graphene layers. Some of the Raman spectra, which show characteristics of monolayer graphene, consist instead of multilayer graphene. There are two possible explanations for this distinction:

– The graphene located in the 'thick island' grew at a higher rate during synthesis, which might influence the dynamics during growth, resulting in a different stacking than islands grown with a lower growth rate.

– It is also possible that the first layers have a turbostratic stacking, and that graphene layers which grow underneath several preexisting layers of graphene posses a defined stacking order. Since the local environment for the SiC decomposition and Si depletion is influenced by the coverage of graphene, it is plausible that it also changes the graphene growth, but further investigations would be needed to unambiguously clarify this issue.

To investigate the electrical transport properties of EG grown in an enclosure, Hall bar structures were prepared for two samples ($T = 1450\,^{\circ}C$, $\Delta t = 60$ min, and $T = 1400\,^{\circ}C$, $\Delta t = 90$ min). Since the graphene is inhomogeneous, large area VdP measurements were not suitable. HB structures enable measurements of locally uniform graphene. An optical micrograph of a patterned HB structure is shown in Fig. 3.35. The results from room tem-

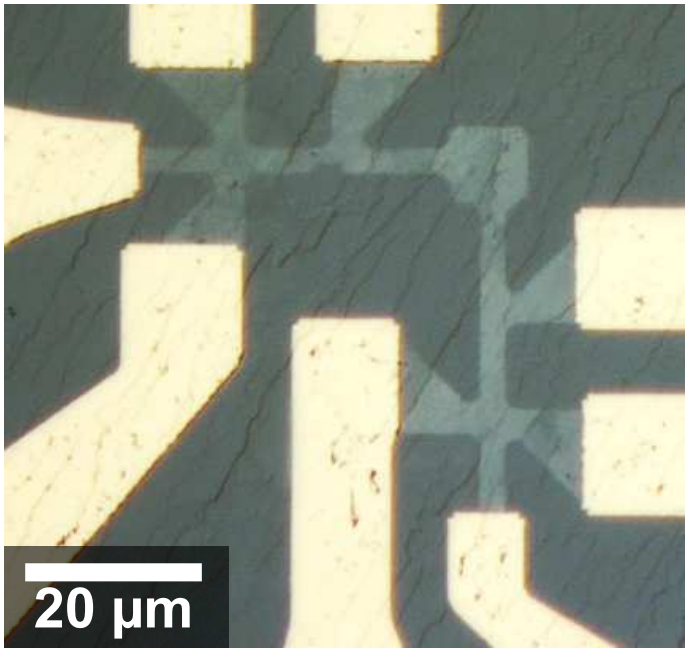

Figure 3.35: Patterned Hall bar structure on EG on C-face SiC grown at 1450 °C for 60 min.

perature measurements reveal that the layers are *p*-doped with a charge carrier density varying between $1.5 \times 10^{13}\,\mathrm{cm}^{-2}$ and $8 \times 10^{13}\,\mathrm{cm}^{-2}$. The measured charge carrier mobility varies between $120\,\mathrm{cm}^2/\mathrm{Vs}$ and $900\,\mathrm{cm}^2/\mathrm{Vs}$. No systematic variations of the electrical transport properties could be determined so far. These mobilities are considerably lower compared with values given by de Heer *et al.*, who reported charge carrier mobilities exceeding $25\,000\,\mathrm{cm}^2/\mathrm{Vs}$ in multilayer graphene samples prepared with the CCS method on C-face SiC.[159]

3.6. Summary

The growth of EG on C-SiC was investigated in this chapter. The use of an Ar atmosphere seems to be unsuitable for growing large-area, homogeneous graphene films. Growth in vacuum leads to complete coverage of the substrate surface, but the graphene contains defects and is composed of a large number of layers, each of which behave like monolayer graphene. Also, the growth in a confined space did not lead to a completely homogeneous coverage of the substrate with graphene. However, our observations suggest that lowering the growth temperature, accompanied by an increase in growth time, may lead to a more controlled and homogeneous growth. Additionally, the design of the confinement itself and the position of the orifice in it should be changed to ensure a consistent Si vapor pressure across the entire substrate surface. Interestingly, graphene layers grown in an Ar atmosphere or in an enclosure show to possess an ordered stacking, which is in disagreement with previous observations.

4. Synthesis of graphene by molecular beam epitaxy

In this chapter, experimental results on the growth of graphene by means of molecular beam epitaxy (MBE) will be presented and discussed. Two different substrates were used, $(6\sqrt{3} \times 6\sqrt{3})$R30°–reconstructed SiC surfaces ('buffer layer') and $Al_2O_3(0001)$ (sapphire). The influence of the growth parameters on the structural properties of the graphene layers was investigated. Atomic force microscopy (AFM), Raman spectroscopy, grazing incidence synchrotron X-ray diffraction (GID) and X-ray photo electron spectroscopy (XPS) were employed. Additionally, density functional theory (DFT) was used in order to explain some experimentally observed phenomena. XPS measurements and DFT calculations were conducted in collaboration with partners from the Chemnitz University of Technology and the Fritz-Haber-Institute Berlin, respectively.

4.1. Growth on $(6\sqrt{3} \times 6\sqrt{3})$R30°-reconstructed SiC surfaces

This section addresses the growth of graphene on $(6\sqrt{3} \times 6\sqrt{3})$R30°–reconstructed SiC(0001) surfaces, also known as buffer layer (BL). This substrate was chosen because its surface is isomorphic to graphene, which means that it possesses the same honeycomb lattice structure and a similar lattice constant.[110] However, the BL has about 30% of its atoms covalently bound to the SiC substrate.[113] Due to its similarities to graphene, the buffer layer can be employed as a template to investigate quasi-homoepitaxy of graphene by means of MBE.

The buffer layer passivates dangling bonds at the SiC surface,[158] and should therefore prevent covalent bonding between the substrate and the graphene film. Because of this, the requirements for van der Waals epitaxy[160] are fulfilled. One considerable advantage of using the BL template instead of epitaxial monolayer graphene (EG) is that experimental results (e.g. obtained by Raman spectroscopy) originating from the substrate and from the MBE-grown films can easily be identified and separated.

4.1.1. Experimental details

MBE growth was performed as described in Section 2.2. A fixed growth temperature of 950 °C was used. This rather low temperature was chosen to prevent further surface graphitization by Si depletion. The growth time varied between 30 and 240 min. The samples were investigated by non-contact tapping-mode AFM, Raman spectroscopy with a spatial resolution of 1 µm and an excitation wavelength of 482.5 nm, and XPS using a monochromated Al Kα X-ray source. For the latter analysis (performed by Felix Fromm from the Chemnitz University of Technology), the samples were annealed at 350 °C for 20 min in UHV in order to remove surface contaminants. Additionally, GID measurements were performed at the ID10 beamline of the *European Synchrotron Radiation Facility (ESRF)* with a photon energy of 10 keV ($\Delta E = 10^{-4}$). The primary intensity

was amounted to 10^{14} counts per second (cps) at a beam size of 100 μm (horizontal) times 1 mm (vertical) with a vertically mounted sample and an angle of incidence of 0.15°.

4.1.2. Results and discussion

Atomic force microscopy

AFM images of the MBE-grown samples are presented in Fig. 4.1. Fig 4.1 (a) – (d) show the large-area ($20\times20\,\mu m^2$) topology of the samples after MBE growth for different deposition times. In each case, an ordered structure with terraces and step edges is visible after the growth process. Hence the surface morphology persists throughout the MBE growth process. No further step bunching or surface graphitization due to surface thermal decomposition occurs (as confirmed by Raman spectroscopy). Corresponding AFM images of a $2\times2\,\mu m^2$ section, taken on terraces of the substrate, are shown in Fig. 4.1 (e) – (f). Corresponding AFM images of bare BL template are shown in Fig. 3.7

The surface roughness of the films measured on several single terraces increases after MBE growth from ∼0.8 Å for a pristine BL sample to 1.2 Å for $\Delta t = 30-60$ min. It reaches a rms value of ∼1.3 Å for $\Delta t = 120$ min, and ∼3.6 Å for $\Delta t = 240$ min. One reason for the increased surface roughness after 4 hours of growth could be the fact that more than 2 hours are needed to form a complete layer of graphene (see XPS investigations). It is possible that the first layer of graphene grows rather flat on the BL, while subsequent layers grow on previously deposited graphene, show higher roughness. No surface segregation or island formation is observed after MBE growth. This indicates that, despite the increased roughness, the MBE-prepared graphene layers grow essentially planar on top of the BL. Note that AFM measurements performed on several surface terraces of different samples reveal that no extended wrinkles or nanofins exist on the surface, which is opposite to what has been observed in graphene grown by MBE using cracked ethanol as precursor,[161] and EG as the substrate (obtained by surface Si depletion of SiC).

Raman spectroscopy

Raman spectroscopy measurements were performed on all samples at the center of surface terraces. Since the SiC substrate, as well as the buffer layer, possess Raman modes in the spectral regions relevant for graphene, these backgrounds have to be subtracted from the raw data before further analysis can be performed. As a first step, all spectra (taken before and after MBE growth) were normalized with respect to the 'plateau' of the SiC background between 1810 cm^{-1} and 1870 cm^{-1} and the SiC background is subtracted. Subsequently, the spectrum of the BL has to be subtracted from the MBE-grown graphene spectrum. Since the Raman intensity of the BL in the spectrum decreases after MBE growth, a program is employed to determine the best BL signal subtraction. The intensity of the BL spectrum (recorded prior to the MBE growth) is scaled by a factor between 0 and 1, and subsequently subtracted from the spectrum acquired from the MBE-grown layer. After each subtraction, two Lorenz-shaped peaks are fitted to the spectrum between 1200 cm^{-1} and 1800 cm^{-1}. The fitting with the lowest χ^2 (which corresponds to the quadratic deviation of the fitting curve and the measured points) was considered and used in the following analysis. Raman spectra of the raw data, with the SiC background removed and additionally the BL background removed are shown in Fig. 4.2.

The contribution of the BL to the Raman spectrum is much less than one would expect if the intensity would simply be reduced by the amount of light absorbed by the graphene

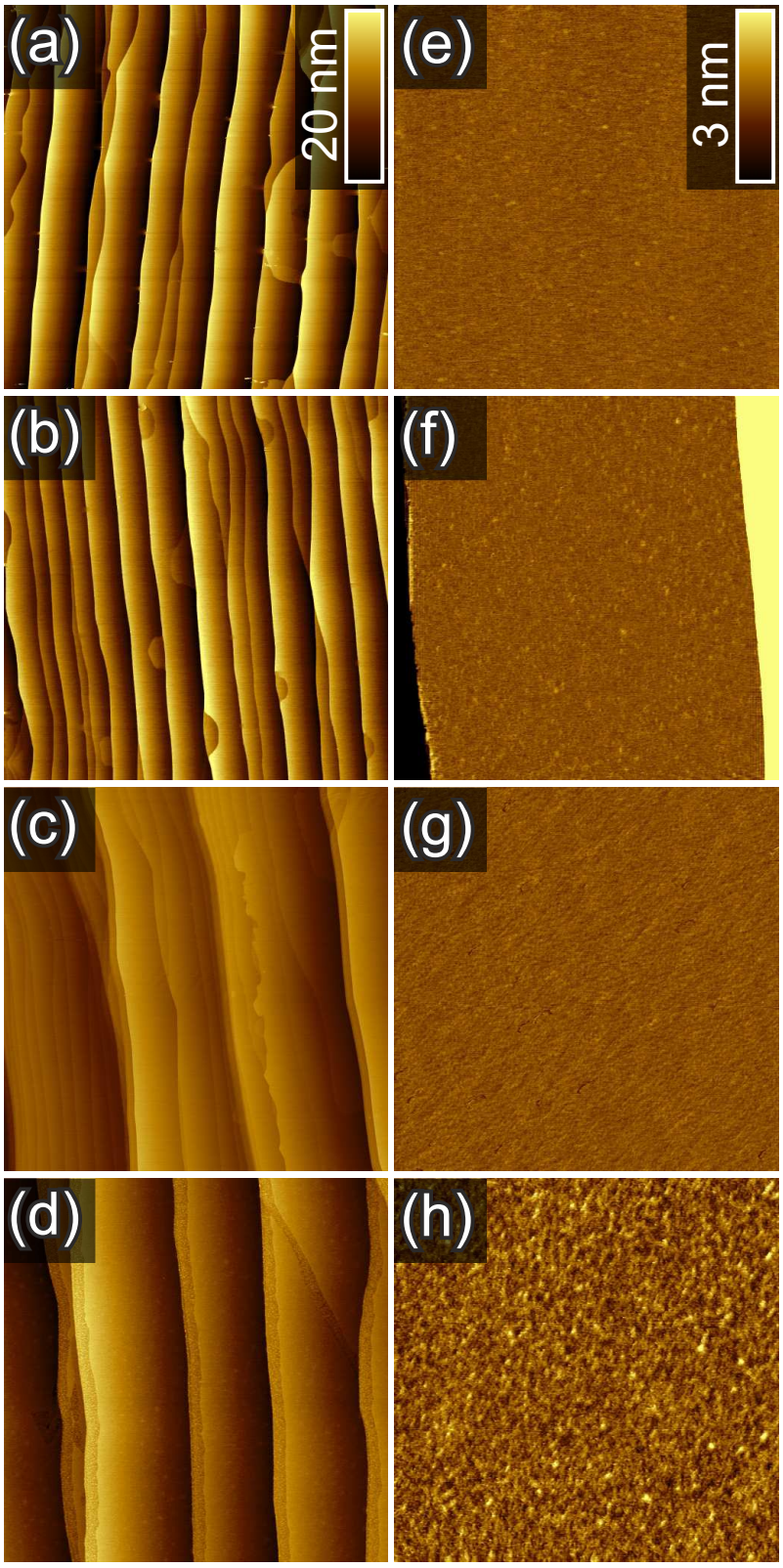

Figure 4.1: AFM images of samples grown by MBE on BL. (a) – (d) images of a 20 × 20 µm section with a vertical scale (see inset of (e)) of 20 nm, (e) – (f) images of a 2 × 2 µm section with a vertical scale of 3 nm. The growth time of the samples is 30 min [(a)/(e)], 60 min [(b)/(f)], 120 min [(c)/(g)] and 240 min [(d)/(h)].

(on the order of a few percent). However, the Raman intensity originating from the BL decreases by about a factor of five. The MBE grown graphene has a similar effect on the Raman intensity of the BL as EG layers produced by surface Si depletion.[66,119]

Raman measurements performed on the center of the surface terraces for each growth condition are displayed in Fig. 4.3. The displayed spectra correspond to what is obtained after subtracting the SiC- and BL-related background signals from the raw data. The spectra show the typical graphene-related Raman features, namely the defect-induced D- and D′-lines at ∼1380 and ∼1610 cm^{-1}, the normal E_{2g} mode (or G-line) at ∼1590 cm^{-1}, the double-resonant 2D-line at ∼2720 cm^{-1}, and the second order line D+D′ at ∼2970 cm^{-1} (see Section 2.3 for details). Five Lorenz-shaped peaks are fitted to the spectra and are displayed as green curves in Fig. 4.3.

The intensity of the graphene signal increases with longer growth times, while the peak widths decrease. Especially the double resonant 2D-peak, which becomes clearly visible for growth times over 120 min. The full widths at half maximum (FWHM) are presented in Fig. 4.3 (b). Overall, the widths decrease monotonically with growth time, indicating an increase in structural order of the grown graphene.[83] Only the G-line FWHM of the layer grown for ΔT = 30 min appears as an exception. This might be due to the fact that the surface coverage for this film is very low (less than 0.4 monolayers – see XPS results below). Consequently, the Raman signal intensity is also quite low, which may result in a non-ideal subtraction of the SiC- and BL- backgrounds. Additionally, the noise in the measurement is proportional to $(\text{counts})^{-1}$. While the *relative* noise decreases with $(\text{counts})^{-1}$, the absolute noise remains high after subtracting the contributions from the

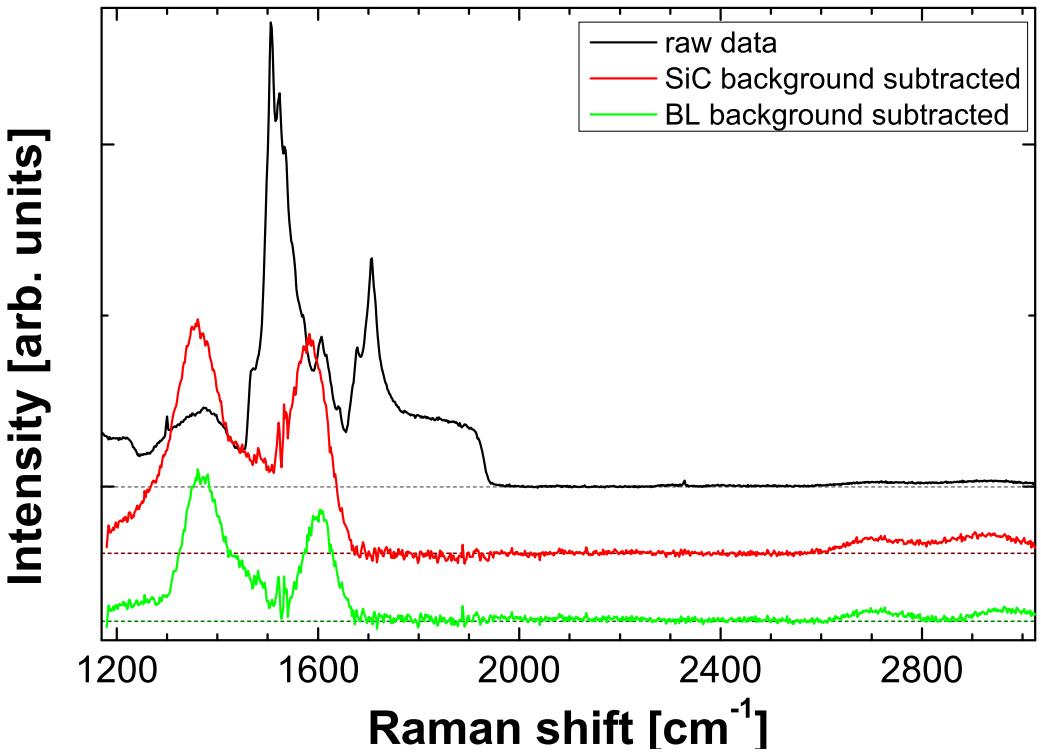

Figure 4.2: Raman spectra of the sample grown for Δt=30 min. Black: raw data, red: SiC background subtracted, and green: SiC+BL background subtracted. The curves are shifted for better visibility, the dotted lines mark the respective zero lines.

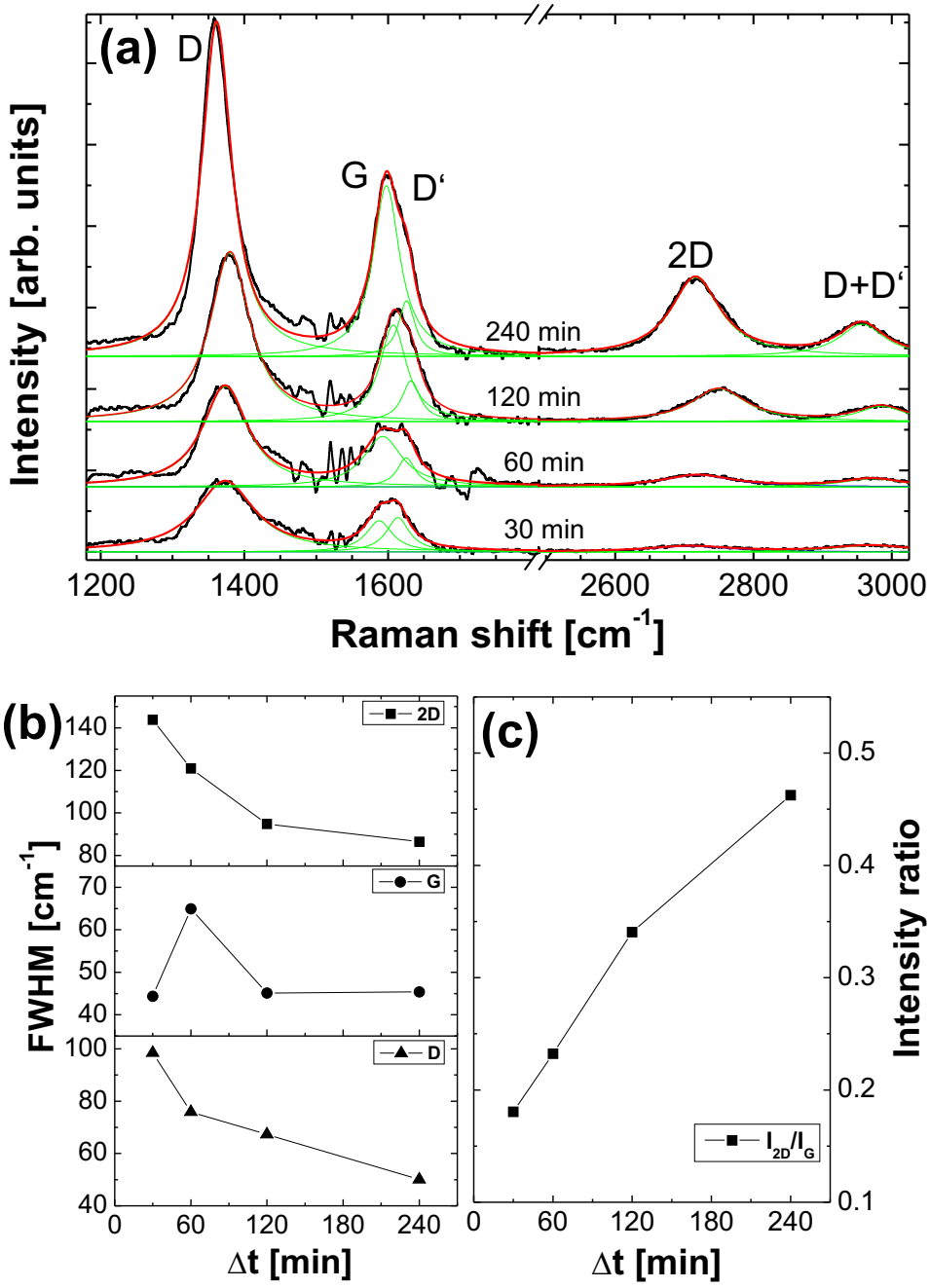

Figure 4.3: (a) Raman spectra and best fit curves (the green curves are single Lorentzians, the red ones are the sum of them) of samples prepared at T_S = 950 °C with growth times as indicated in the plot. The background spectra originating from the SiC and the BL were removed. The spectra are shifted vertically for better visibility. (b) Full width at half maximum (FWHM) of the D-, G- and 2D lines as a function of growth time. (c) Ratio between the intensities of the 2D- and G-lines as a function of growth time.

SiC- and BL-background signals, and may influence the results of the peak fittings. In Fig. 4.3 (c), the intensity ratio (I_{2D}/I_G) between the 2D- and G-line versus growth time is displayed. It increases monotonically, confirming that the fraction of sp^2-bonded carbon arranged in the graphene honeycomb lattice increases with growth time.[83] The average lateral size L_a of the graphene domains can be determined by taking into account the peak parameters of the different lines, i.e. their intensity ratios and peak widths (see Section 2.3 for details). The resulting values for the lateral sizes of the graphene domains as calculated by the different methods are displayed in Fig. 4.4.

For the present case, L_a increases from ∼5–7 nm for ΔT = 30 min to ∼15–20 nm for ΔT = 240 min. These values can be taken as a lower limit for the actual crystallite size, since the model provided by Cançado *et al.*[93] consider as defects only domain boundaries, and not point-like defects (such as vacancies or sp^3-bonded C-atoms) located within the graphene domains. This might too be the reason why L_a calculated by the integrated peak intensities of the D- and G-line is lower in respect to the values given by the other parameters. The sensitivity of the D-line (in comparison to the D′-line) is higher for point-like defects than for boundary-like defects.[87] The Raman measurements reveal that the film is not a single crystalline graphene sheet, but it is composed of nanocrystalline graphene.

The influence of the growth temperature was also investigated by Raman spectroscopy. The growth time was fixed at 240 min and the substrate temperature was varied between 900 and 950 °C. Representative spectra are shown in Fig. 4.5 (a). The spectra vary little within this temperature range, with relative intense D-peaks ($I_D/I_G > 1$) in comparison to EG. The size of the nanocrystalline graphene domains, calculated from the Raman parameter are presented in Fig. 4.5 (b). There is no discernible difference in domain size

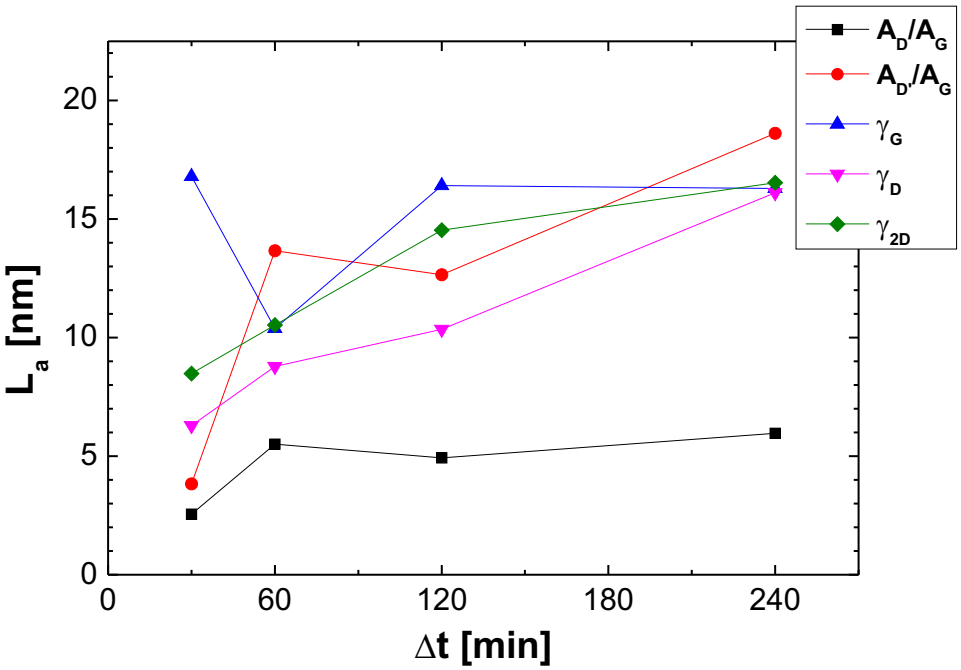

Figure 4.4: Lateral size L_a of the graphene domains, as calculated from different Raman peak parameters. $A_\star$ denotes the integrated peak intensity and $\gamma_\star$ the FWHM of the respective Raman line $\star$.

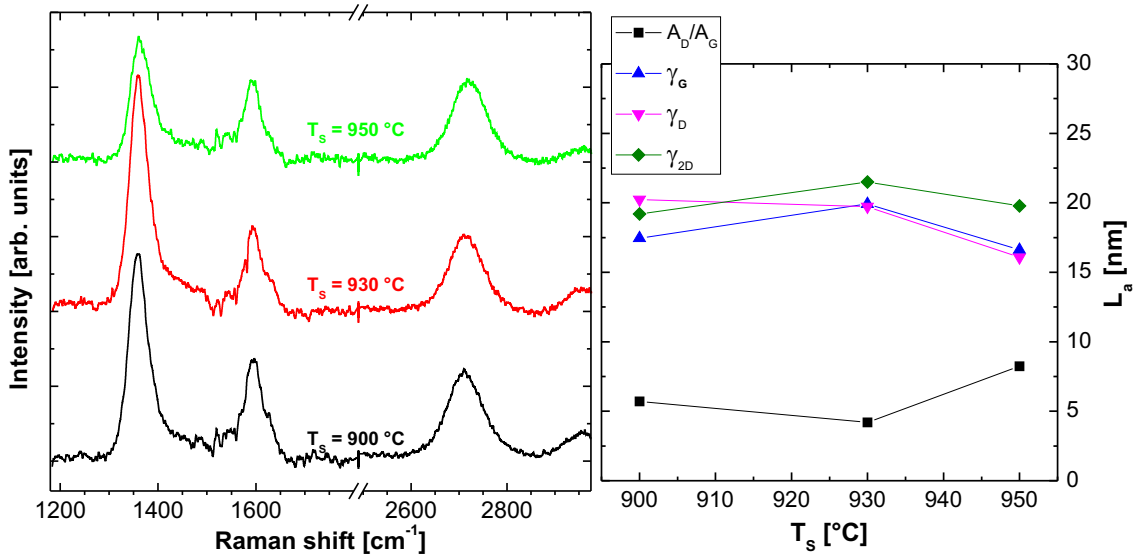

Figure 4.5: Raman spectra of MBE-grown nanocrystalline graphene samples synthesized at different temperatures. The growth time was 240 min, with the respective substrate temperature T_S as indicated in the figure. The intensities are normalized in respect to the (subtracted) SiC Raman background. The curves are shifted against each other for better visibility.

within the (small) temperature range investigated. However, we can speculate that the graphene's quality is dependent on the substrate temperature (see Section 4.2, Fig. 4.12 for such investigations for graphene growth on sapphire). Nevertheless, the maximum deposition temperature is limited by the temperature at which SiC starts to decompose.

X-ray photoelectron spectroscopy

X-ray photoelectron spectroscopy (XPS) measurements were performed in order to determine the number of graphene layers grown by MBE, as well as the bonding within the films.[65,113] A representative measurement of the C1s core-level spectrum is presented in Fig. 4.6 for the graphene film grown for 60 min on the BL/SiC(0001) substrate. Two components of the spectrum are related to the BL (S_1 at ∼284.70 eV and S_2 at ∼285.35 eV, orange). The lower energy component S_1 is due to the covalent bonding between the BL and the SiC (sp^3-bonds), while S_2 arises from the sp^2-bonded carbon within the buffer layer.[113] This confirms that the BL remains unaltered during the MBE growth process even for the longest employed growth times, as was also observed by Raman spectroscopy. It also reveals the absence of strong interaction, i.e. covalent bonding, between the BL and the MBE-grown graphene layer. The component which corresponds to carbon in the SiC bulk is seen at ∼283.61 eV, while the component at ∼284.61 eV is due to the carbon in the sp^2-bonding configuration, which forms the MBE-grown graphene. From the intensity ratio between the SiC and graphene components (taking into account the existence of the BL as well), the thickness of the MBE films could be deduced. In the investigated samples, the number of layers monotonically (but not linearly) increases from ∼0.4 monolayers (ML) for a growth time of $\Delta t = 60$ min to ∼0.6 ML for $\Delta t = 120$ min, and up to ∼1.5 ML for $\Delta t = 240$ min. Hence, more than 120 min are needed to form one complete ML. Finally, it is observed that the graphene peak in the C1s spectrum is shifted to higher binding energies with respect to the neutral position (∼284.45 eV, measured

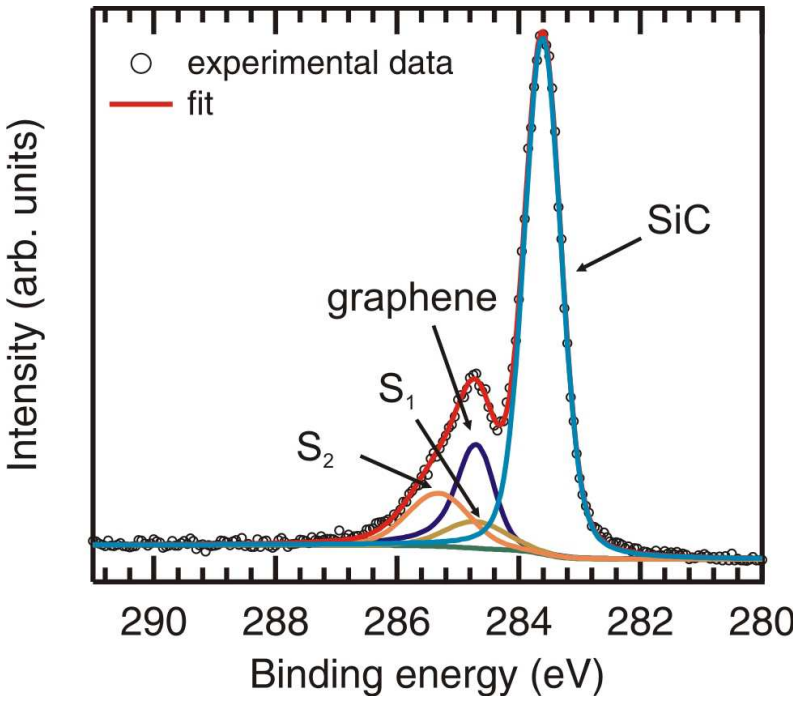

Figure 4.6: C1s core level spectrum of a MBE grown graphene film on a BL/SiC(0001) template with a growth time of Δt = 60 min. There are two contributions, labeled S_1 and S_1, which correspond to the BL, a third one related to the SiC bulk, and a forth one related to the MBE-grown graphene layer. Data acquisition and curve fitting was performed by F. Fromm (TU Chemnitz).

for HOPG). This means that the graphene layer is *n*-doped, similar to what is observed for monolayer graphene synthesized by surface Si depletion of SiC(0001), see Chapter 3. However, the ∼0.15 eV shift of observed in the present case is small than the values observed for those samples (∼0.3 eV), indicating a lower level of intrinsic doping in MBE-graphene. In the sample with $\Delta t = 240$ min, a component related to C-O bonds is found, which indicates that a small amount of oxygen is incorporated in the film. It is important to note that this is the only sample on which synchrotron X-ray diffraction measurements were performed prior to the XPS measurements. Therefore it is possible that the oxygen incorporation did not take place during the MBE process, but rather later during the investigation.

Grazing-incidence X-ray diffraction

Grazing-incidence X-ray diffraction measurements (GID) were performed in order to obtain information about the structure as well as the epitaxial alignment of the MBE-grown layers. The GID measurements were performed for pristine BL substrates as well as for the sample grown for 240 min, where it is certain (as shown by XPS) that at least one complete graphene layer has formed on the substrate.

A RSM, recorded for the sample with $\Delta t = 240$ min, is presented in Fig. 4.7. The axes are scaled in reciprocal lattice units (rlu) of the SiC substrate. Therefore, the reflections from the SiC appear at integer values in the map. This is a good test to verify if the transformation from angular space (in which the map was recorded) to reciprocal space is correct.

The reflections associated with SiC, the BL, and the graphene appear at the same angular positions, revealing that the graphene film and the buffer layer are in-plane aligned with the substrate. Therefore, the graphene domains possess a single orientation, since a distribution of many randomly aligned domains would lead to a diffraction ring at the same radial position in reciprocal space (which means with the same length of the scattering vector, or the same lattice constant). In order to examine a larger angular range, line scans along $\mathbf{q_a}$ over the G(11$\bar{2}$0) reflection with an azimuthal range of 130° were performed, as shown in Fig. 4.8.

Only graphene (and analogous BL) peaks with a separation of 60° emerge, with an intensity that is two orders of magnitude higher than the background signal. Hence, the carbon lattice in the nanocrystalline domains possess six-fold symmetry, as expected for graphene, and at least 99 % of the graphene domains are aligned with the substrate. This result is inconsistent with what has been measured for nanocrystalline graphene grown by MBE (when cracked ethanol is used as the precursor) on epitaxial graphene on SiC.[162] In that work, samples analyzed by reflective high energy electron diffraction (RHEED) did not show any preferential alignment with the EG/SiC(0001) substrate. The GID result presented here also contradicts the notion that graphene synthesized by MBE should generally be composed of randomly aligned nanocrystals.[163,164]

Even though our graphene films possess a single crystallographic orientation, the size of the domains is limited to a few nm, as shown by Raman spectroscopy. This raises the question as to why no coalescence takes place. The scan in the angular direction reveals a FWHM of ∼0.5° and hence a quite narrow rotational distribution, but this small mis-

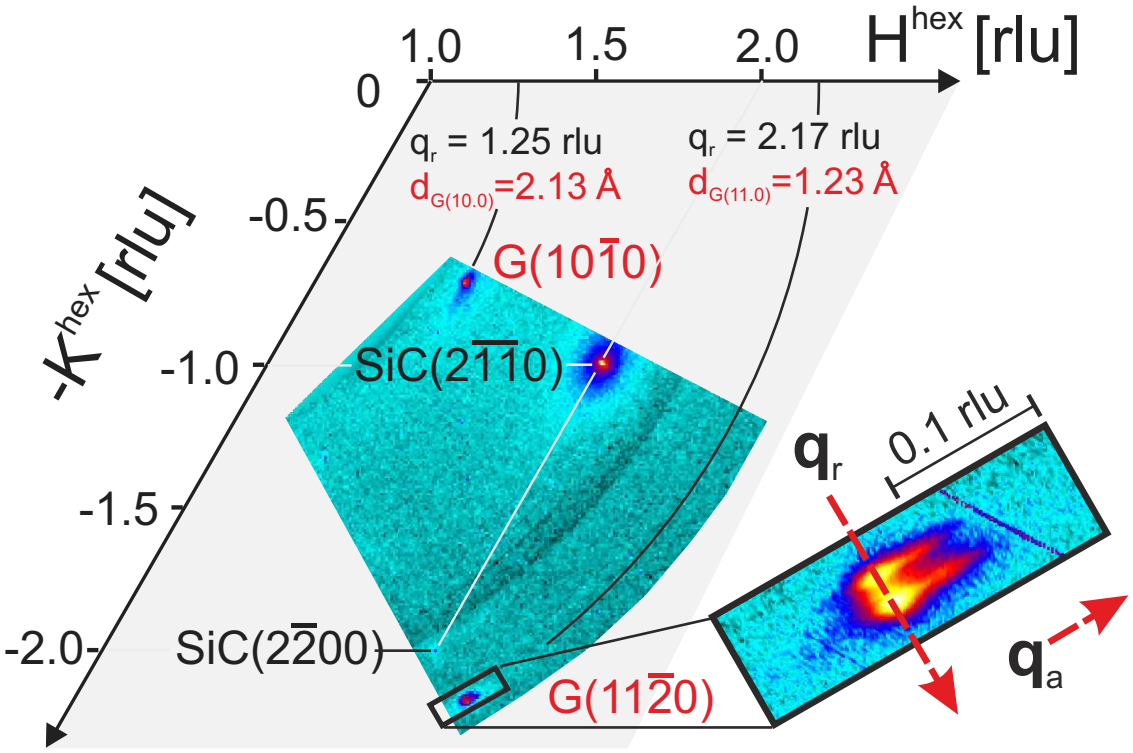

Figure 4.7: Reciprocal space map of MBE grown nanocrystalline graphene on a BL/SiC(0001) template. The inset shows a higher resolution around the graphene (11$\bar{2}$0) reflection, revealing a splitting into a BL and a graphene reflection.

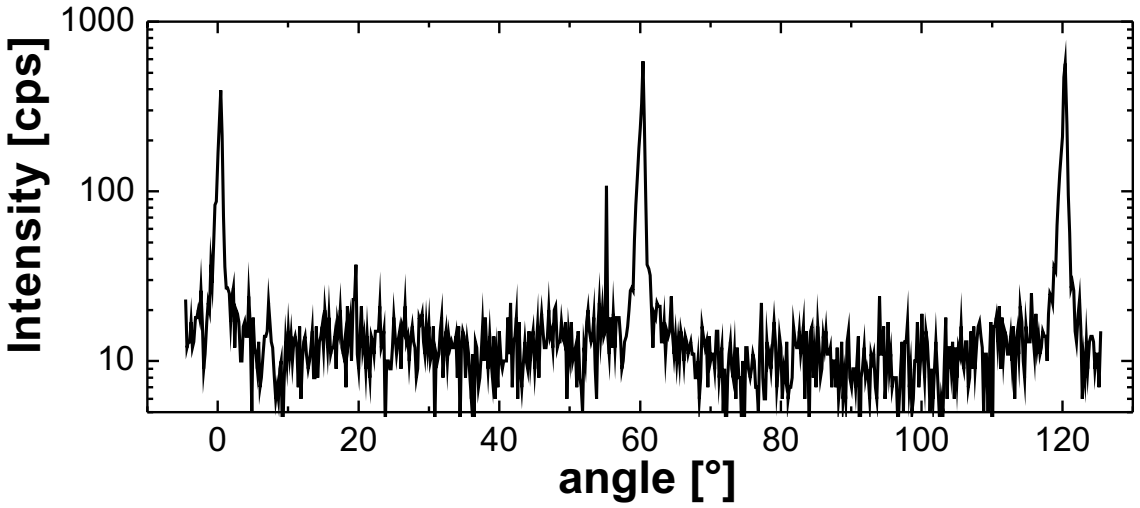

Figure 4.8: Angular scan with a range of 130° over the graphene(11$\bar{2}$0) reflection, performed on the sample grown for Δt = 240 min.

alignment could already be enough to hinder effective coalescence between neighboring islands. Additionally, the moderate temperature of 950 °C might be too low for an effective healing of defects in the grain boundary regions, which might contain localized amorphous structures, and hence impede coalescence. Scanning tunneling microscopy (STM) measurements may shed light on the structure of the grain boundary regions, but were unavailable during the duration of this thesis.

GID offers a complementary method to the before presented Raman spectroscopy to determine the lateral sizes L_a of the graphene domains. By fitting the graphene related R2 peak (in Fig. 4.9) with a Gaussian function, a lower limit for the domain size could be estimated via the application of the determined fitting values into the Scherrer equation:

$$L_a = \frac{K\lambda}{\beta \cos\theta}, \tag{4.1}$$

where K is a dimensionless shape factor (here considered as 1), λ is the X-ray wavelength (1.24 Å), β is the FWHM (0.00415 rad), and θ is the Bragg angle of the peak (30.39°). The value for L_a is ∼35 nm, which agrees well with that derived from the Raman data.

The inset in Fig. 4.7 shows the RSM with higher resolution around the graphene (11$\bar{2}$0) reflection. A splitting into two components can be observed. One of the two reflections corresponds to the graphene, the other to the underlying buffer layer. A line scan over the graphene (11$\bar{2}$0) peak is shown in Fig. 4.9. For comparative purposes, a corresponding measurement from a pristine BL/SiC sample is also added to the plot. By comparing these two scans, one can unambiguously attribute the peak R1 to the underlying buffer layer. The graphene reflection, labeled R2 in Fig. 4.9, is clearly shifted towards higher $\mathbf{q_r}$ in comparison to the BL reflection, which correspond to a smaller lattice parameter in the analyzed in-plane direction. The lattice parameter derived from Fig. 4.9 are 2.446 Å and 2.464 Å for the MBE grown graphene and the BL, respectively. This yields a mismatch of ∼0.7%. Interestingly, the lattice parameter of the MBE-grown graphene is about 0.6% smaller than the lattice parameter of graphite (2.461 Å).[20] There are several potential causes for this conspicuous contraction:

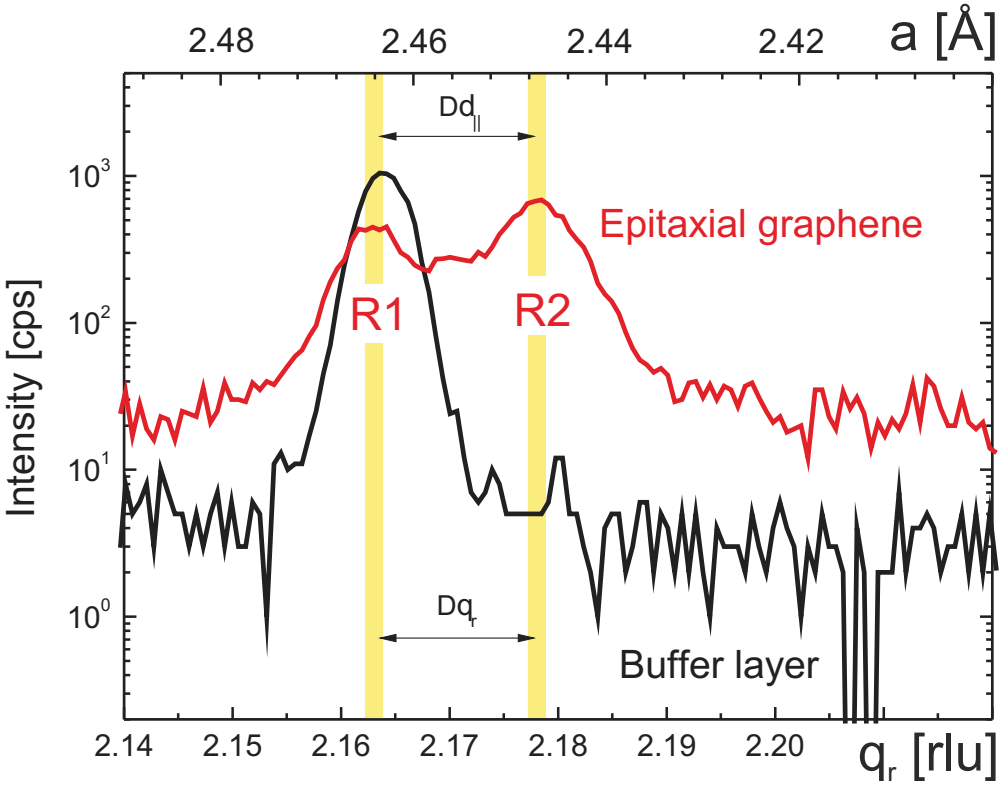

Figure 4.9: Radial scans along the graphene $(11\bar{2}0)$ direction. The red curve shows a measurement on MBE grown graphene ($\Delta t = 240$ min), while the black curve is an according scan on a bare BL sample. The peak positions of the BL (R1) and graphene (R2) reflections are indicated by the shaded areas.

(i) the contraction could be related to the difference in coefficient of thermal expansion between graphene and SiC.[165–167] Based on this difference, Ferralis *et al.*[165] estimated that a compressive strain in graphene up to ∼0.8% can arise upon cooling a sample to room temperature, since SiC contacts during cooldown, while graphene expands.[149,150]

(ii) The strong corrugation of the BL, which is a product of its partial covalent bonding to the SiC,[110] could also contribute to the apparent contraction of the (projected) lattice parameter of the nanocrystalline graphene, despite the existent epitaxial relation between them. Recent first-principle calculations[168] quantify the corrugation of epitaxial monolayer graphene films on the BL to be ∼0.4 Å.

(iii) A lateral contraction of graphene could also be induced by the presence of intrinsic defects and/or domain boundaries in the nanocrystalline film. The strong D-peak in the Raman spectra (see Fig. 4.3) as well as the small-scale structures seen in the AFM image [Fig. 4.1 (h)] indicate the presence of both point- and linear defects in the films.

Regarding point (i), we deduced a compressive strain of ∼0.4% by Raman spectroscopy and GID (see Section 3.4) for epitaxial monolayer graphene on SiC(0001). A similar contraction was directly linked to substrate thermal contraction in a study of near-perfect CVD-grown graphene on Ir(111).[20] However, the contraction we observed induces a significantly smaller lattice parameter then that found in Refs. [20, 137]. In a perfect graphene plane, strain relaxation by forming wrinkles would be expected (as is the case for epitaxial graphene grown on C-face SiC, see Section 3.5), but our AFM analysis shows no such structures in our MBE-grown films.

Density-functional theory calculations

To estimate possible contributions of (ii) and (iii), density-functional theory (DFT) calculations were performed with collaborators from the Fritz-Haber-Institut (FHI) Berlin, the results of which will be presented here. The calculations were performed using the all-electron, localized basis set code 'FHI aims'[169]and the PBE (*Perdew, Burke, Ernzerhof*) functional[170] with a correction for van der Waals (vdW) effects, PBE+vdW.[171]

To estimate the influence of a possible substrate-induced corrugation [point (ii) above], the following procedure was used. A fully relaxed structure of a graphene sheet with a (13×13) supercell is situated on top of the BL, as determined in Ref. [168]. Its calculated maximum corrugation perpendicular to the surface (top to bottom atom) amounts to 0.41 Å. The MBE-grown graphene on the BL should show the same approximate corrugation. If this corrugation led to significant stress in the plane, a perfect graphene sheet with fixed z corrugation leads to a surface area that corresponds to an effective graphene lattice parameter of a = 2.462 Å. The calculated contraction is thus less than 0.05%.

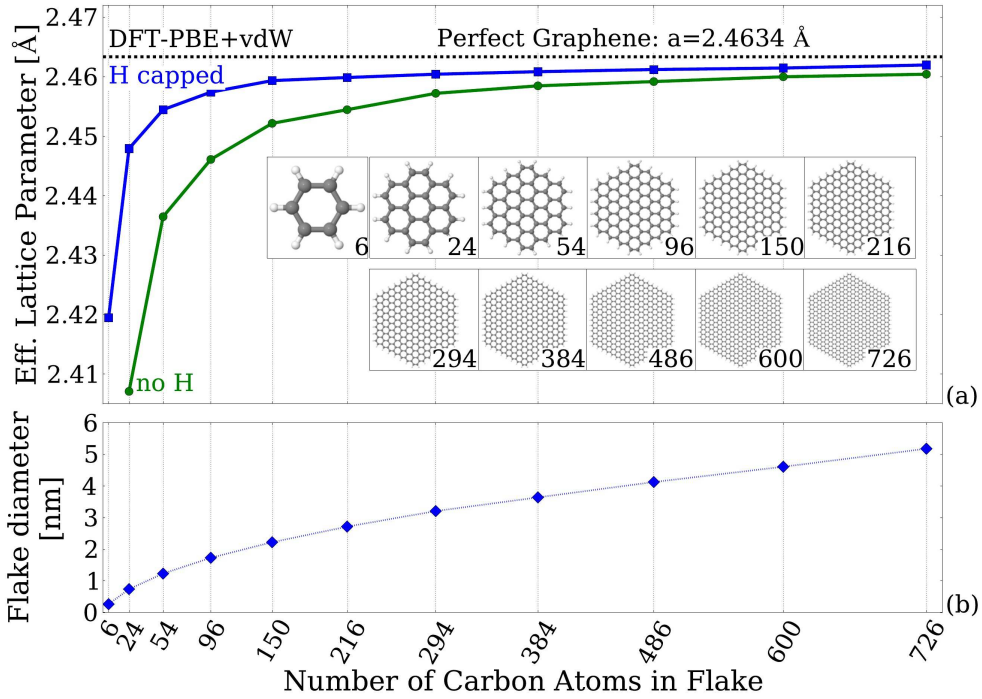

Figure 4.10: (a) Calculated effective lattice parameter (average C-C bond length) in a series of fully relaxed graphene flakes of finite size with (squares) and without (circles) hydrogen termination at the edges. The hydrogen-terminated flakes are shown in the inset. The lattice parameter of a flat, strain-free, periodic graphene sheet calculated in DFT-PBE+vdW is indicated by a dashed line. (b Diameter (maximum C-C distance) of the flakes used in (a). The image was created by L. Nemec from the FHI Berlin.

The potential impact of different types of defects on the in-plane lattice parameter was also investigated. Fig. 4.10 shows the development of the effective lattice parameter of finite-size graphene flakes as a function of flake size. This resembles the influence of one-dimensional defects, such as domain boundaries. Two different types of flakes were considered, either with a H-saturated boundary or with no extrinsic bond saturation at

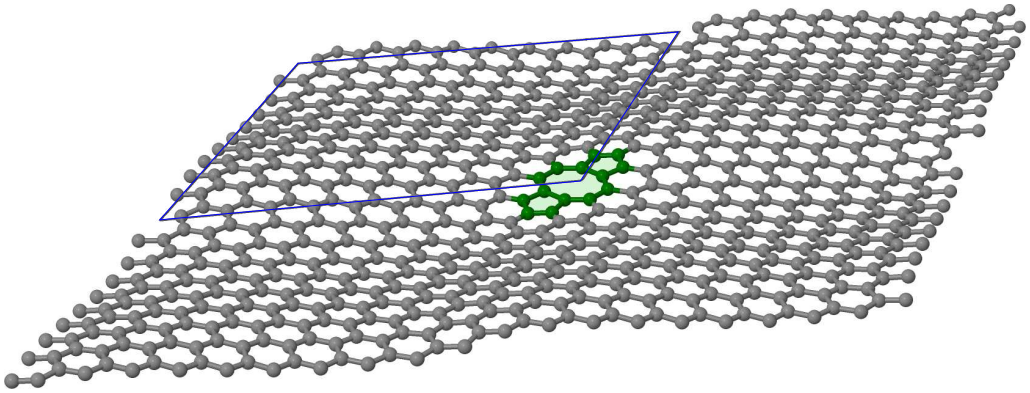

Figure 4.11: The calculated, fully relaxed (atomic positions and unit cell) structure of a graphene sheet with a (10×10) periodic arrangement of 5-8-5 di-vacany defects (highlighted in green). The in-plane supercell is indicated by thin blue lines. The image war created by L. Nemec from the FHI Berlin.

the boundary. A significant contraction of the effective lattice parameter results in either case. But to approach the experimentally determined lattice parameter of 2.446 Å (Fig. 4.9) by this effect alone, the equivalent saturated flakes would have to be extremely small (less than 0.7 nm in diameter). The equivalent unsaturated flakes, however, could be significantly larger (1.7 nm). With increasing flake size, the net lattice contraction decreases rapidly. Since an average flake size in the order of 10 nm was determined by Raman spectroscopy (Fig. 4.4), this effect is not enough to explain alone the observed contraction.

Localized zero-dimensional (point-like) defects can also lead to strain and corrugation in graphene sheets.[172,173] Fig. 4.11 gives quantitative predictions for the strain, corrugation and net area change of a periodic graphene sheet with well-defined arrays of specific common defect types: mono-vacancies, di-vacancies, and the Stone-Wales defect. As an example, the calculated structure of a fully relaxed structure of graphene with a (10×10) periodic arrangement of 5-8-5 di-vacancy defects is shown in Fig. 4.11.

Mono-vacancies in graphene have been intensively studied (e.g. Refs. [173, 174] and references therein). As listed in Table 4.1, mono-vacancies would be associated with significant strain and corrugations of perfect graphene sheets if no spin polarization were included. However, mono-vacancies are in fact paramagnetic defects that carry a significant local moment in the DFT-PBE+vdW model used here. This leads to a slight reduction of the compressive strain compared to a perfect graphene sheet, and thus also to a reduction of the overall distortion (buckling of the mono-vacancy and corrugation of the sheet). Even with 2% mono-vacancies (modeled by a (5×5) periodicity in Table 4.1), mono-vacancies alone would not yet lead to the full strain seen in the GID experiment above.

Among the investigated point defects, di-vacancies are thermodynamically more stable than mono-vacancies.[172,175] The calculated results for di-vacancies with corrugation shown in Table 4.1 were obtained by starting from the fully relaxed, non-spinpolarized mono-vacancy geometries and removing the most strongly buckled atom (in z-direction) in the mono-vacancy. As can be seen in the structure of the (10×10) di-vacancy defect in Fig. 4.11 and Table 4.1, this procedure leads to significant strain and buckling in a free-standing graphene sheet. The sheet curvatures seen at the defect location follow the trend described in the literature.[172] Therefore, such defects could easily explain the

(5×5)			(7×7)			(10×10)		
a_{eff}	$\Delta z_{top\text{-}bottom}$	ΔA_{defect}	a_{eff}	$\Delta z_{top\text{-}bottom}$	ΔA_{defect}	a_{eff}	$\Delta z_{top\text{-}bottom}$	ΔA_{defect}
Mono-vacancy, non-spinpolarized								
2.447	0.741	-1.72	2.445	0.800	-1.78	2.459	0.865	-1.88
Mono-vacancy, spin-polarized (ferro- or paramagnetic								
2.453	<0.01	-1.06	2.458	0.197	-1.11	2.461	0.055	-0.98
Di-vacancy, non-spin-polarized, corrugated								
2.417	1.023	-4.94	2.431	1.566	-6.82	2.443	1.888	-8.46
Di-vacancy, non-spinpolarized, flat (metastable)								
			2.447	$\leq$0.02	-3.42			
Stone-Wales defect, non-spinpolarized								
			2.469	0.00	+0.54			

Table 4.1: DFT-PBE+vdW calculated effective lateral lattice parameter a_{eff} (in Å), the top-to-bottom corrugation $\Delta z_{top\text{-}bottom}$ (in Å) and effective area lost (gained) per defect ΔA_{defect} (in Å^2) of different defect types and periodicities in an ideal, free-standing graphene sheet. The data was obtained by V. Blum and L. Nemec from the FHI Berlin.

experimentally observed lateral lattice parameter reduction even for relatively low defect concentrations [(10×10) case]. In fact, significant corrugations of this kind were experimentally observed by atomically resolved STM images of defects in HOPG generated by ion implantation.[176] However, even if a di-vacancy was completely flat the associated strain would still be significant. For comparison, Table 4.1 also includes data for a flat (7×7) periodic di-vacancy, which is a local structure optimum about 0.1 eV higher in energy than the corrugated di-vacancy arrangement. Even at this defect density, di-vacancies would be sufficient to explain the observed strain. Finally, also the Stone-Wales defect was included, which results from the rotation of a single C-C bond, but where the number of C atoms remain unchanged. In this case, rather than compression, a slight expansion of the overall lattice constant would result.

These idealized theoretical defects are certainly just approximations to the experimental reality of the MBE-grown nanocrystalline graphene films. The film is likely characterized by a combination of the defect types considered here (and possibly others). But it is qualitatively plausible that strain introduced by defects plays a considerable role in the observed overall lattice contraction measured by the GID measurements. Eliminating the potential for metastable defects will be important to achieve large-scale, homogeneous, epitaxial, MBE-grown graphene films. On the other hand, controlling the nature and concentration of defects in a graphene sheet during growth may be a promising route towards strain-engineered graphene films.

4.1.3. Summary

The synthesis of nanocrystalline graphene films by MBE on $(6\sqrt{3} \times 6\sqrt{3})$R30°–reconstructed SiC(0001) surfaces, as well as their characterization, was presented and discussed in this section. Raman spectroscopy measurements indicate an improvement in the structural quality with increasing growth time. The average size of the graphene domains exceeds 15 nm for layers grown for 240 min. XPS measurements confirm that the buffer layer persists throughout the MBE growth process, and which also reveal that the upper-most MBE-grown graphene film consists of sp^2-bonded carbon and thus seems to interact weakly with the underlying BL pseudo-substrate. This indicates that van der

Waals epitaxy takes place. Strikingly, GID measurements reveal that the graphene domains are in-plane aligned to the BL template (and hence also with the SiC substrate). Therefore, despite its nanocrystalline nature, the layer possesses an epitaxial relation to the substrate. In addition, GID shows that the lattice parameter is strongly contracted in comparison to freestanding and perfect graphene layers. By a first principle approach for isolated graphene sheets, collaborators from the FHI derived reference values for the lattice parameter contraction expected from buckling of the graphene, edges associated with finite size graphene flakes, and defects in a periodic supercell arrangement. The calculations show that the presence of mono- and di-vacancy defects lead to a contraction in the lattice parameter. The largest contraction is associated with di-vacancy defects, and even a low defect concentration may result in the experimentally observed contraction.

Overall, the results presented in this section demonstrate the feasibility of using MBE as a method for the controlled synthesis of graphene layers directly on an insulating substrate. Nevertheless, the growth conditions (e.g. substrate temperature) have to be optimized in order to allow the preparation of layers with higher structural quality, i.e. increasing the graphene domain sizes exceeding hundreds of nanometer and lower defect concentration.

4.2. Growth on Al_2O_3(0001)

In this section, the growth of graphene films by MBE on Al_2O_3(0001) substrates is investigated. The *c*-plane sapphire was selected as the substrate for heteroepitaxy of graphene due to its hexagonal symmetry. This may facilitate graphene epitaxy since its in-plane lattice constant (4.75 Å)[177] is approximately twice that of graphene (2.46 Å). Additionally, the thermal stability of sapphire allows growth experiments at high substrate temperatures, which is likely necessary for the formation of high-quality graphene layers by means of MBE.

The samples were investigated with the same methods as the samples grown on the $(6\sqrt{3} \times 6\sqrt{3})$R30°–reconstructed SiC surfaces, and additionally transmission electron microscopy (TEM) were performed by my colleague Raquel Gargallo-Caballero. It has to be noted that the results presented here were obtained through a collaboration between my colleague Myriano H. Oliveira Jr. and myself.

4.2.1. Experimental details

In this study, samples were prepared at three different substrate temperatures (800, 900, and 1000 °C, limited by the employed substrate heater) and for growth times varying between 15 and 480 min. AFM, XPS, GID and Raman measurements were performed using the same equipment as described in 4.1. The additional TEM measurements were carried out in a JEOL 3010 microscope operating at 200 keV, equipped with a GATAN slow-scan charge-coupled device camera. Cross sectional specimens were prepared by mechanical polishing followed by Ar-ion milling along the two orthogonal $[2\bar{1}\bar{1}0]$ and $[01\bar{1}0]$ projections. Carrier density and mobility values were obtained by magnetotransport measurements in a large-ares (>5 × 5 mm^2) van-der-Pauw geometry.[96] The measurements were carried out at low magnetic fields up to 0.6 T, and at room temperature as well as 77 K.

4.2.2. Results and discussion

Raman spectroscopy

Raman spectra of samples grown at three different temperatures (800, 900 and 1000 °C) and with four different growth times (15, 120, 240 and 480 min) are displayed in Fig. 4.12. In all samples, six different Raman peaks (see Section 2.3) are visible: the G- and 2D-line, as well as the defect related D- and D′-peaks, and the 2nd order G+D′ and 2D′ peaks.[85] Since the sapphire substrate does not possesses Raman lines in the investigated spectral region, no background subtraction has to be performed and hence the spectra are thus easier to analyze in comparison to those for the samples grown on $6\sqrt{3}$–reconstructed SiC.

The presence of a D-peak in all spectra of Fig. 4.12, as well as of the 2D peak, indicates that the MBE-grown films contain a graphitic structure. However, the knowledge about the degree of crystallinity of each sample depends on a more detailed analysis taking into account the evolution of Raman features as a function of the different growth conditions. Considering the spectra of the samples with a growth time $\Delta t = 15$ min [Fig. 4.12(a)], it can be noticed that they show only two well-resolved features (the D- and G-peaks) and, at the spectral region of higher wave numbers (2400 – 3300 cm^{-2}), only a low-intensity bump instead of a clearly resolved 2D peak. This, combined with the large FWHM of the

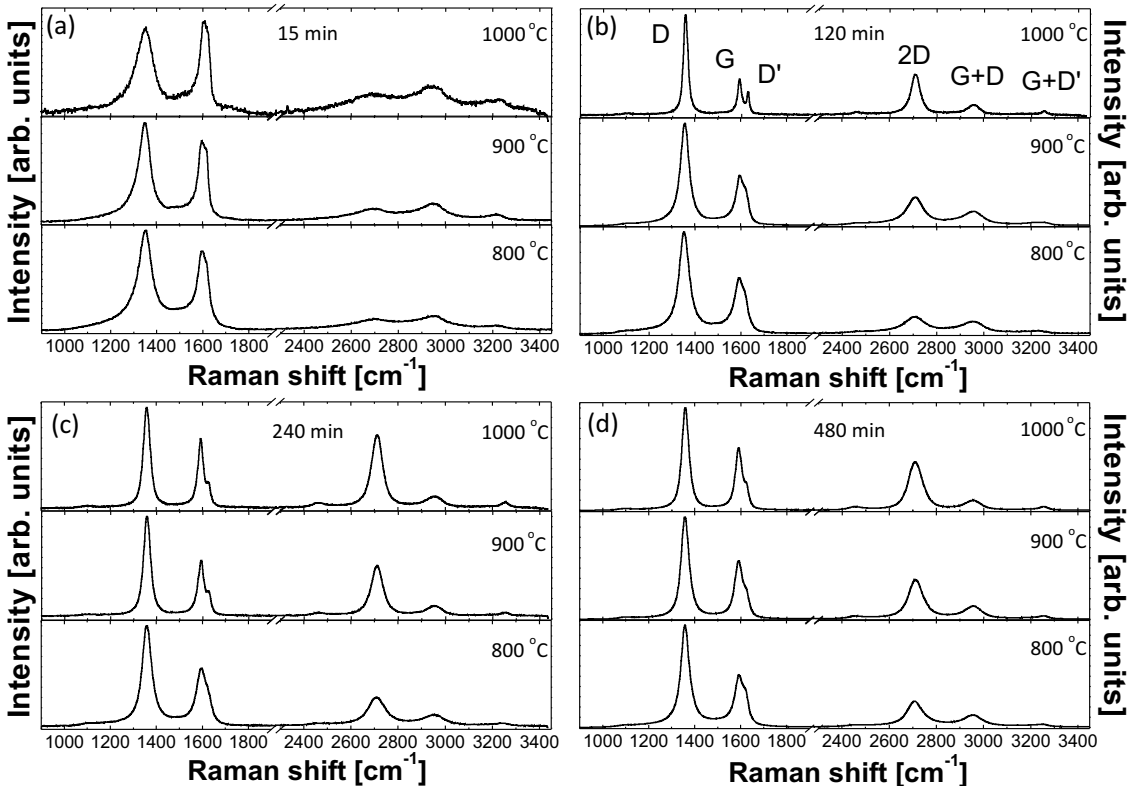

Figure 4.12: Raman spectra of carbon layers grown by MBE on $Al_2O_3(0001)$ for growth times of (a) 15 min, (b) 120 min, (c) 240 min and (d) 480 min, at different temperatures. For growth times of 15 min (a) the spectra show typical features of highly disoriented sp^2 carbon structures, with broad peaks and low intensity second order-related peaks. For longer growth times (b – d), the Raman spectra display features that are characteristic for nanocrystalline graphene domains, such as narrow peaks and a well-resolved and intense 2D peak.

G and D peaks (as shown in Fig. 4.13 (a)), is typical for highly disordered graphitic-like structures.[178]

The spectra clearly change for longer growth times, as depicted in Fig. 4.12 (b) – (d). In all of these cases, the degree of crystallinity increases with increasing substrate temperature. Two main changes in the spectra reveal this trend, (i) a narrowing of the peaks takes place and (ii) development of clearly resolved second order peaks (especially the 2D-line) instead of a low-intensity, diffuse bump. The dependence of the width of the peaks on the substrate temperature is displayed in Fig. 4.13 (a). Only the films grown for 15 min follow a different trend, which is probably related to their coverage on the substrate surface (see below). The narrowing of the G peak is clearly observed by the rising of a doublet shape for the G-peak, which is due to a smaller overlap between it and the D′ peak.

Fig. 4.13 (b) illustrates the influence of the growth time, displayed for a substrate temperature of 1000 °C. For the film deposited for 15 min, the spectrum displays typical characteristics of a highly disordered graphitic structure. The appearance of the D′-peak in the spectrum of the film grown for 30 min, due to the narrowing of the G- and D′-peaks, indicates an improvement in the structural ordering. However, due to the high intensity of this peak (approximately as intense as the the G peak), as well as the absence of well-

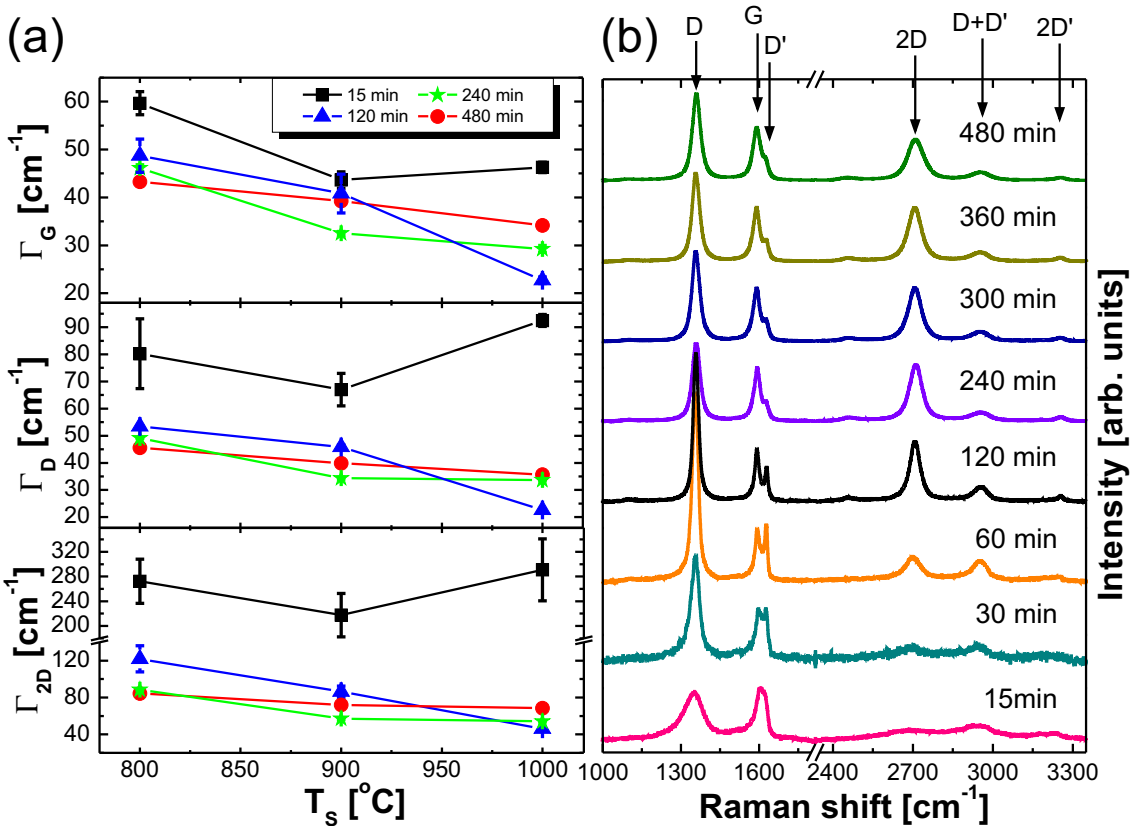

Figure 4.13: (a) Dependence of the FWHM of the G, D and 2D peaks (Γ_G, Γ_D and Γ_{2D}, respectively) on the growth temperature T_S for different growth times. (b) Raman spectra of carbon films deposited at $T_S = 1000\,°C$ with different growth times. The spectra are normalized to the G peak intensity.

defined second-order peaks, the material still cannot be classified as crystalline. Increasing the growth time to 120 min leads to the appearance of the 2D-peak (at $\sim$2700 cm^{-1}), and the narrowing of the first order peaks. Nevertheless, the high intensity of the D peak (as well as the D′) may be evidence for the small sizes of the in-plane crystalline domains. The Raman spectra of films deposited for 240 min or longer exhibit very similar features with high-intensity 2D-peaks, narrow first-order peaks, and D- and D′-peaks with lower intensities, in comparison to the 15- and 30-min cases. These characteristics reveal the growth of nanocrystalline graphene.[93,178]

The evolution of the Raman spectra shown in Fig. 4.13 (b) is also correlated to the surface coverage of the deposited films. The layer thickness of some of these films were determined by XPS (similar to the case of growth on reconstructed SiC). For the films grown for 480 min, a thickness of $\sim$3 graphene layers was determined, for the film synthesized at $T_S = 900\,°C$ and $T_S = 1000\,°C$. Interestingly, for the film grown at 1000 °C for 120 min the Raman spectrum shows typical features of nanocrystalline graphene, but magnetotransport measurements (see below) reveal that no complete, conductive layer is formed on the surface. This indicates that this film, as well as those with growth times below 120 min (at 1000 °C), does not cover the entire substrate surface. On the other hand, all layers prepared with a growth time of 240 min, or longer, are conductive. Therefore, based on the combination of results obtained by Raman-, XPS-, and magnetotransport-measurements, it is plausible to state that for growth times shorter than 60 min the carbon

atoms are aggregated in highly disordered islands, which randomly cover only a fraction of the substrate surface.

Similar to the investigations on graphene grown on buffer layer substrates, the Raman spectra are employed to determine the lateral sizes of domains in the nanocrystalline graphene films. The values for L_a were determined taking into account the widths Γ of the G and 2D peaks, as well as the intensity ratios I_D/I_G and $I_{D'}/I_G$. The resulting domain sizes are displayed in Fig. 4.14.

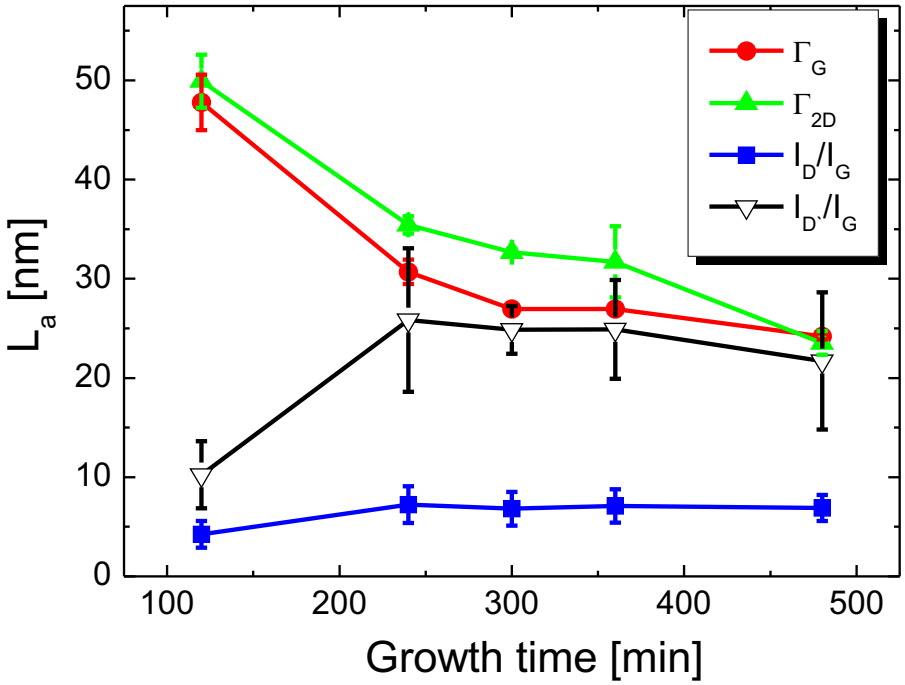

Figure 4.14: Comparison between the average graphene domain size calculated on Γ_G, Γ_{2D}, I_D/I_G and $I_{D'}/I_G$. The substrate temperature during growth was 1000 °C for all samples.

As in the case of the growth on the BL, the domain sizes calculated by I_D/I_G differs from the L_a calculated from the other parameters, which again indicates that the defects in the layer do not consist only of domain boundaries, but also point defects. Overall, the domain sizes L_a possess a lower limit of ∼30 nm (with the same reasoning as growth on the BL). A more detailed analysis and discussion for the samples presented here can be found in Reference [94].

AFM and TEM analysis

An AFM surface morphology of the sample grown at T_S = 1000 °C for 480 min is depicted in Fig. 4.15. An average RMS roughnesses of 1.9 Å was measured. This value differs only slightly from what was measured on the bare Al_2O_3 substrate prior to the growth (RMS roughness ∼1.5 Å). Even for this growth condition, which led to the thickest film obtained at 1000 °C, no evidence of island formation is seen. This supports the idea that a layer-by-layer process takes place.

The layered structure of the material is confirmed by high-resolution transmission electron microscopy (HRTEM) measurements. Fig. 4.16 illustrates a cross sectional HRTEM micrograph of the graphene structure grown at 1000 °C for 300 min on Al_2O_3 along the

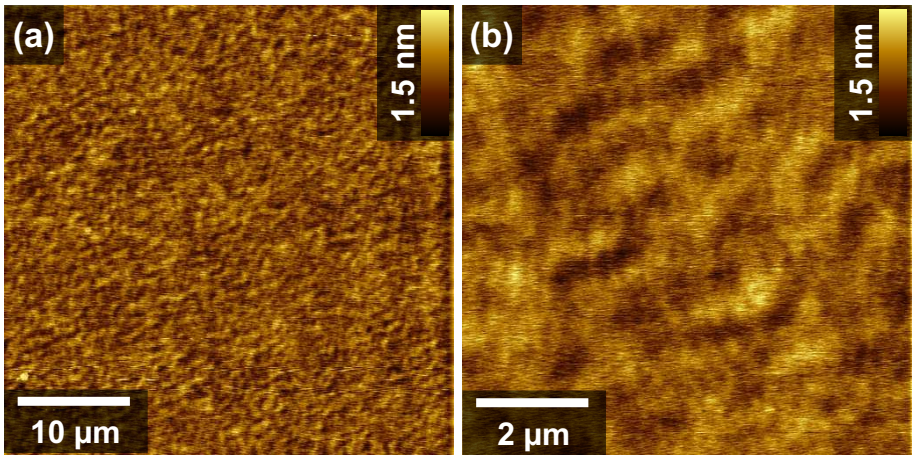

Figure 4.15: AFM images obtained for (a) 40×40 µm^2 and (b) 8×8µm^2 scanned areas of the sample grown at 1000 °C for 480 min.

$Al_2O_3[2\bar{1}\bar{1}0]$ zone axis. A multilayer graphene structure with a thickness of a few layers is observed. The carbon atomic layers are present as bright lines, as designated by the arrows in the left inset of Fig. 4.16. As observed, the film exhibits a planar morphology, which confirms that the graphene layers possess a predominant in-plane order. The presence of some local corrugation within the carbon layers is also seen. The carbon layers corresponding to the areas free of corrugations are separated by 3.3 ± 0.2 Å(see insets of Fig. 4.16), very close to the theoretical interlayer distance of the set of $\{0002\}$ planes in hexagonal graphite ($d_{0002} = 3.335$ Å at low T)[17], and experimental observations

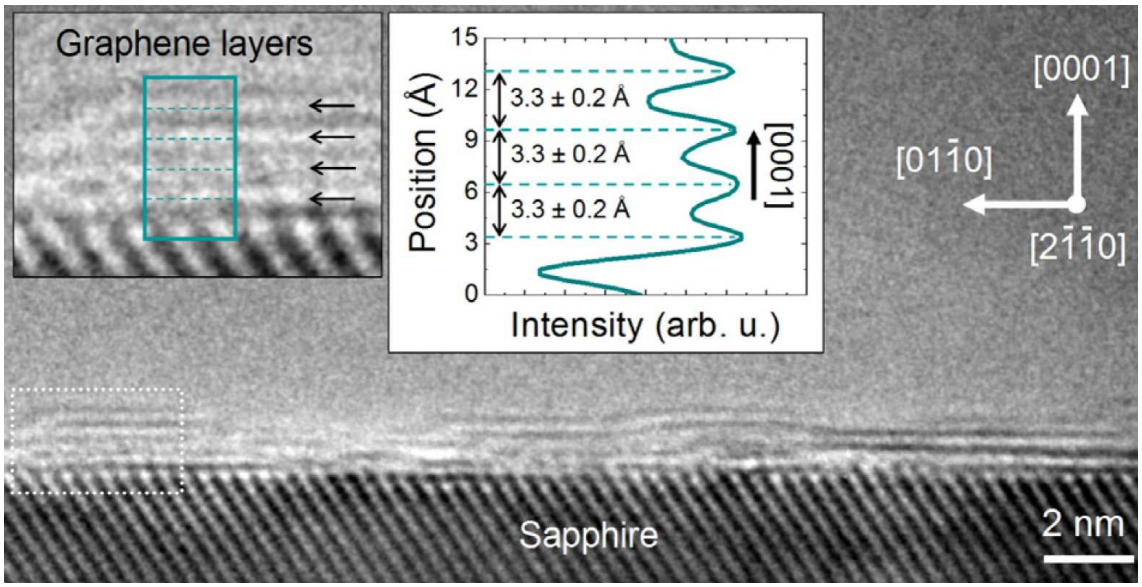

Figure 4.16: Cross-sectional HRTEM micrograph of the graphene structure on AL_2O_3 along the $[2\bar{1}\bar{1}0]$ zone-axis. The left inset shows a magnified image of the white dashed rectangle and the right inset shows an average linescan of the intensity along the growth direction corresponding to the marked area in the left inset (integration width 2 nm). This image was taken from a film grown at 1000 °C for 300 min. The data was collected and processed by Raquel Gargallo-Caballero.

($d_{0002} = 3.354$ Å at 300 K).[179] It is also in good agreement with previous observations for graphene on SiC.[180,181] In the presence of local corrugations, this spacing between layers can increase up to about 1 Å. The formation of such ripples may be associated with the presence of atomic steps in the sapphire substrate, and/or with the relaxation of the graphene layers with respect to the atomic structure of the sapphire substrate, similar to graphene on SiC.[182,183] Also, different coefficients of thermal expansion could introduce these ripples in the film during post-growth cooling, as it is the case of epitaxial graphene on C-face SiC.[155,184]

On the other hand, from qualitative analysis of this HRTEM image, it can be observed that the interface between graphene and Al_2O_3 appears to be inhomogeneous. While at some regions it is easily visible that a graphene layer is the first layer adjacent to the sapphire surface, at others this is not evident. Therefore, as a first approximation, these results could indicate that the chemical nature of the interface may be spatially inhomogeneous. At present, a detailed investigation based on HRTEM imaging with the assistance of contrast simulations is in progress (by Raquel Gargallo-Caballero) in order to obtain further insight into this subject. Even though a thickness variation (mainly between 1 and 4 graphene layers) is observed by HRTEM, it is not in disagreement with the AFM images since these variations are on the order of the surface roughness.

Grazing incidence X-ray diffraction

The orientation and lattice constant of the graphene nano-domains was determined by GID measurements. A reciprocal space map (RSM) measured with a primary beam energy of 10 keV is displayed in Fig. 4.17.

Two substrate-related reflections [$Al_2O_3(2\bar{1}\bar{1}0)$ and $Al_2O_3(3\bar{3}00)$] and two graphene related reflections [G($10\bar{1}0$) and G($11\bar{2}0$)] are visible in the RSM. Additional reflections, which are not aligned with the high symmetry directions of the Al_2O_3(0001) substrate, are also present. Their origin is uncertain at the moment, but could be related to a new phase which is formed due to an intermixing between C and the Al_2O_3 substrate. Such an intermixing was observed in the HRTEM study, but more detailed investigations are still necessary to unambiguously assign these peaks.

Similar to the case of growth on the buffer layer, the graphene reflections manifest themselves as isolated peaks and not as diffraction rings in the RSM. Therefore, all the graphene domains possess the same epitaxial orientation with respect to the substrate. To gain further insight, a line scan in the angular direction over the graphene ($11\bar{2}0$) peak is shown in Fig. 4.18. In the measured range of 130°, three distinct peaks with a separation of 60° can be observed, which means that the MBE grown graphene layer possesses the expected six-fold symmetry. The full width at half maximum of the peaks is ∼4.0°.

In order to determine the lattice parameter of the graphene layers grown on sapphire, two line-scans along $\mathbf{q_r}$ were performed (corresponding to the red and dark blue arrow in Fig. 4.17) and are displayed in Fig. 4.19 (a) and (b). These high-range scans give an overview, and are also used to align the substrate-related peaks to the correct position.

To evaluate the lattice parameter quantitatively, only the section around the graphene related peaks are shown in Fig. 4.20. The x-axis is scaled to directly display the lattice parameter of the respective graphene reflections. Therefore, both measurement curves can be plotted within the same graph.

The measurements reveal a lattice parameter of 2.458±0.016 Å (graphene($11\bar{2}0$) peak) and 2.457±0.018 Å (graphene($1\bar{1}00$) peak). The error values describe the standard deviation of fitted Gaussian curves. These values are ∼0.1% smaller in comparison to the

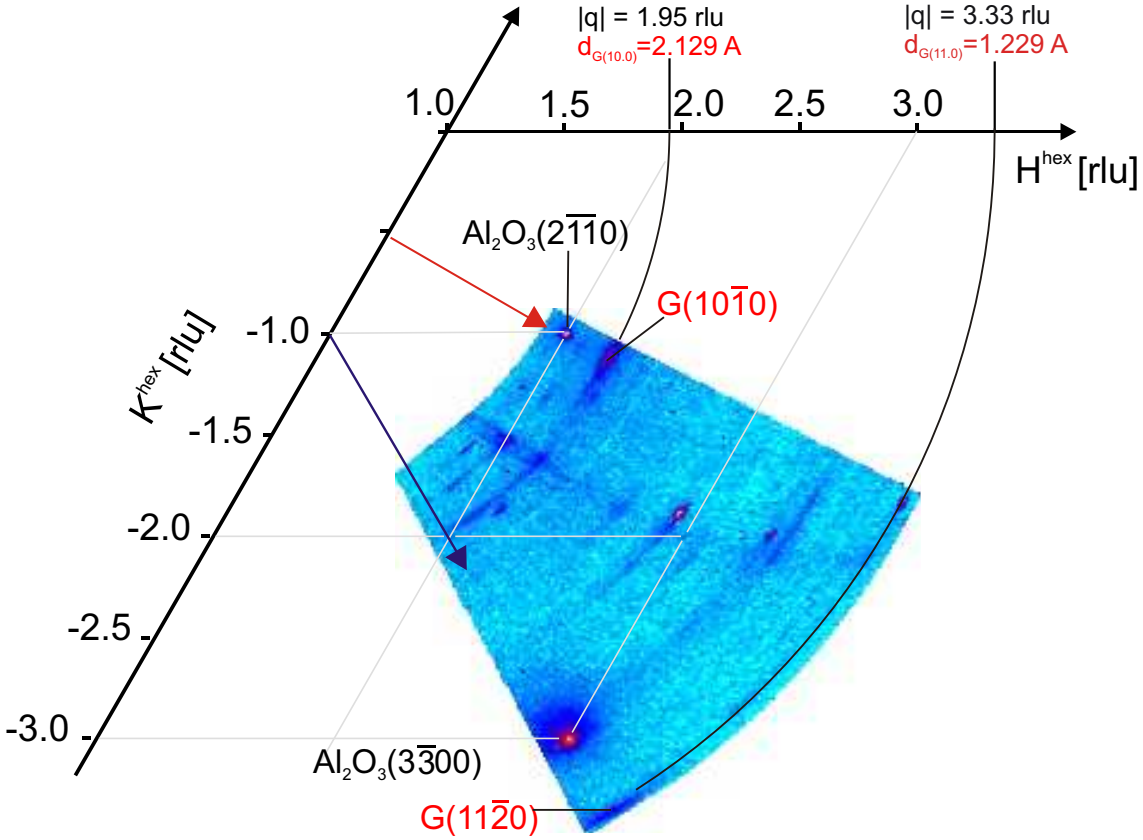

Figure 4.17: Reciprocal space map of a MBE grown sample on Al_2O_3 at a substrate temperature of 1000 °C and a growth time of 300 min. The map is scaled in the reciprocal lattice units (rlu) of the sapphire substrate

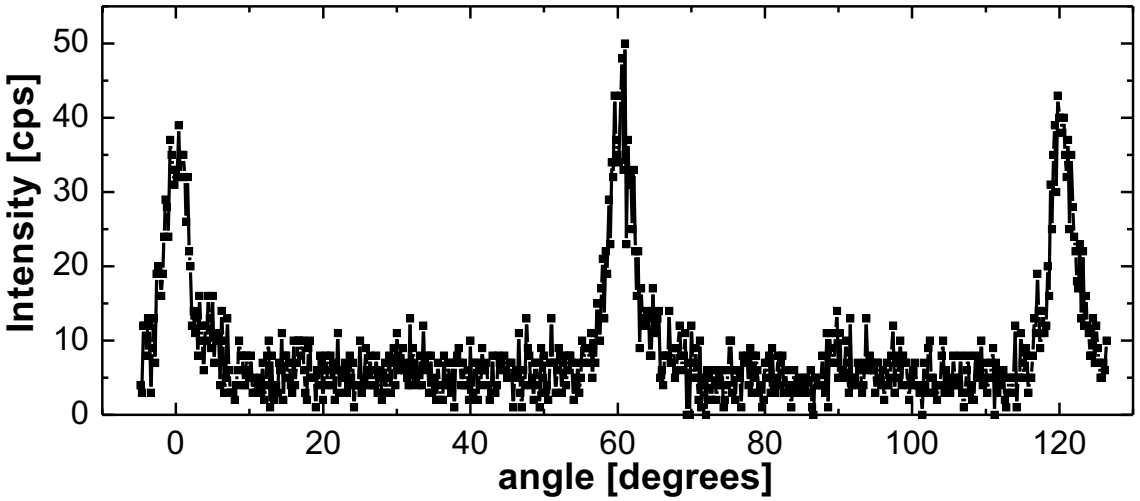

Figure 4.18: Scan in angular direction over the graphene(11.0) reflection.

lattice parameter of bulk graphite (2.461 Å),[20] which might again be explained by the presence of defects, similar to the case of growth on the buffer layer (see DFT calculation in Section 4.1).

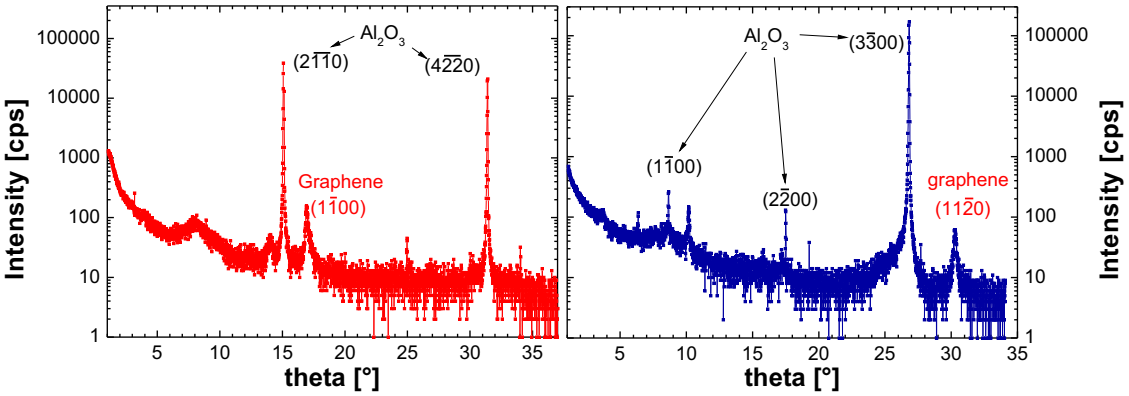

Figure 4.19: GID scan in radial direction direction over (a) the graphene(10$\bar{1}$0) reflection and (b) the graphene(11$\bar{2}$0) reflection. The two directions correspond to the arrows depicted in Fig. 4.17, the x-axis is scaled with the angle-of-incidence of the incoming beam.

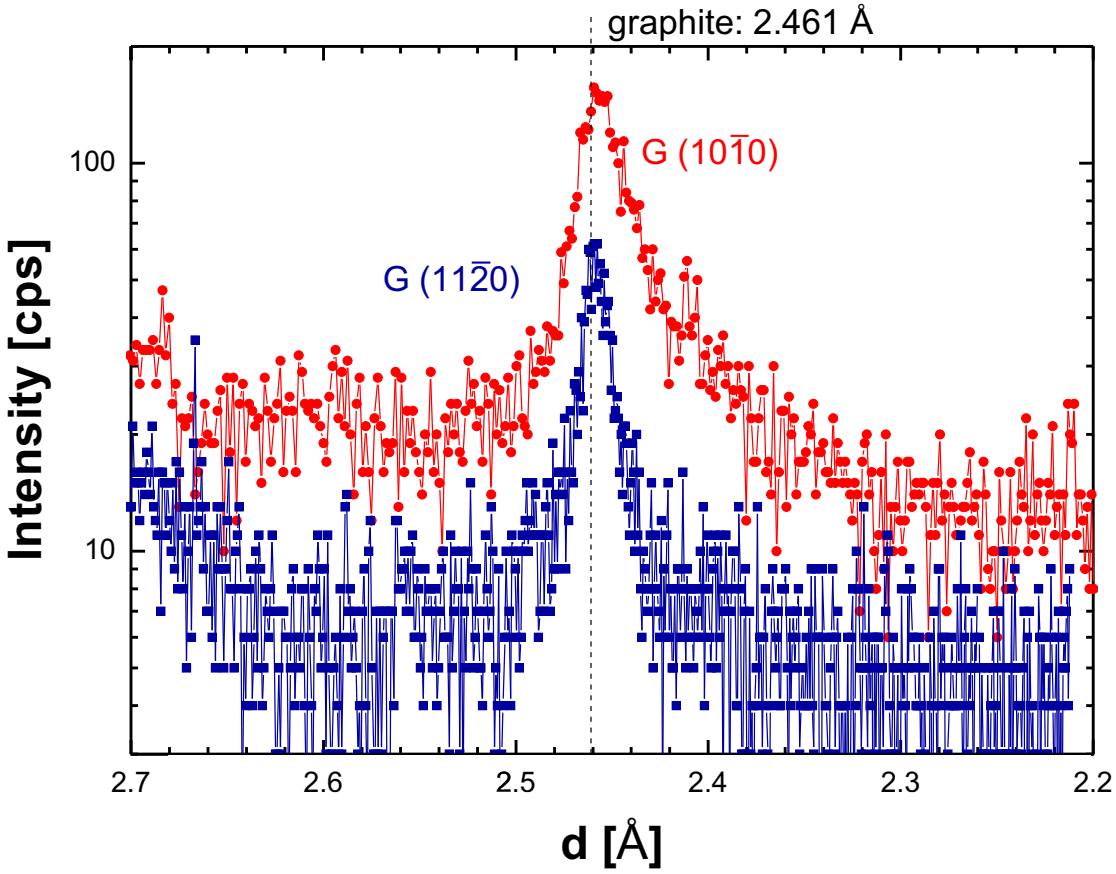

Figure 4.20: Scan in radial direction over the graphene (10$\bar{1}$0) and (11$\bar{2}$0) reflections, plotted against the graphene lattice parameter. The x-axis is scaled to represent the lattice parameter of the respective reflections with the indices as denoted within the figure.

Electrical characterization

The electrical properties of the MBE grown films on sapphire were determined by large-area (>5 × 5 mm^2) van der Pauw magnetrotransport measurements. These measurements were performed at room temperature and 77 K, and yielded the majority carrier type, concentration, and mobility). Two samples were examined, both with growth times of $\Delta t = 480$ min, and growth temperatures of 900 °C and 1000 °C. The determined values for carrier density, carrier mobility and sheet resistance are displayed in Table 4.2. Measurements performed on samples with a growth time of 120 min did not yield reliable results, which is in agreement with the fact that no complete layer was formed after this shorter growth time.

T_S [°C]	Δt [min]	p [10^{13}cm^{-2}]	μ [cm^2/Vs]	ρ [k$\Omega/\square$]
900	480 min	1.5±0.1	64±7	6.7±0.7
1000	480 min	1.2±0.2	111±23	4.8±0.5

Table 4.2: Values obtained from magnetotransport measurements for nanocrystalline graphene grown on Al_2O_3.

The nanocrystalline graphene films show *p*-type doping with similar carrier densities, all on the order of 10^{13} cm^{-2}. The carrier mobility *pmu* is significantly higher for the sample grown at an elevated temperature of 1000 °C in comparison to the sample grown at 900 °C. Hence, an increase in substrate temperature results in enhanced transport properties, as expected from the improvement in crystal quality (e.g. increase in domain sizes). Measurements performed at 77 K show no significant difference in comparison to measurements performed at room temperature, neither in carrier concentration or mobility. This suggests that the graphene films interact only weakly with the underlying substrate, and hence the layers can be described as quasi-freestanding. If a strong interaction between the graphene and substrate takes place one would expect increased carrier mobility at decreased temperature, due to freeze-out of phonons in the substrate.[185]

Interestingly, the doping type is opposite to what has been measured for graphene also grown on Al_2O_3 using CVD.[63] The reason for this difference is unknown at the present time.

4.2.3. Summary

In this section, the growth of nanocrystalline graphene of different thicknesses on 2-inch Al_2O_3(0001) wafers by MBE has been demonstrated. Raman spectroscopy shows a strong dependence of the structural quality of the graphene layers on the substrate temperature during growth (ranging from 800 °C up to 1000 °C) and time (ranging from 15 min up to 480 min). In particular, films prepared at 1000 °C possess the highest crystalline quality, and are composed of nanocrystalline layers which are aligned parallel to each other and the surface, with in-plane domains exceeding 30 nm in size. TEM analysis confirms the planar nature of the prepared films, and shows the existence of corrugations/defects within the layers. Grazing incidence X-ray diffraction reveals that the nanocrystalline domains possess a consistent alignment with the substrate, and a lattice parameter close to the one of undisturbed graphite. In terms of transport properties, measurements performed using van der Pauw geometry show that the graphene films are *p*-doped, and yield mobilities of ∼110 cm^2/Vs at room temperature.

The results shown in this section demonstrate the feasibility of using MBE to achieve the controlled, large-area synthesis of graphene (mono- and few-layer) directly on an insulating substrate.

4.3. Comparison between the growth on reconstructed SiC and Al_2O_3

In this section, similarities and differences in the results obtained from investigating the growth by MBE on $6\sqrt{3}$–reconstructed SiC(0001) and Al_2O_3(0001) surfaces will be discussed.

On first examination, the results appear to be quite similar. Nanocrystalline graphene films can be synthesized on both substrates, as determined by Raman spectroscopy. Two spectra, one for each substrate, are depicted in Fig. 4.21. The growth time was 240 min, the substrate temperature was 900 °C, in both cases.

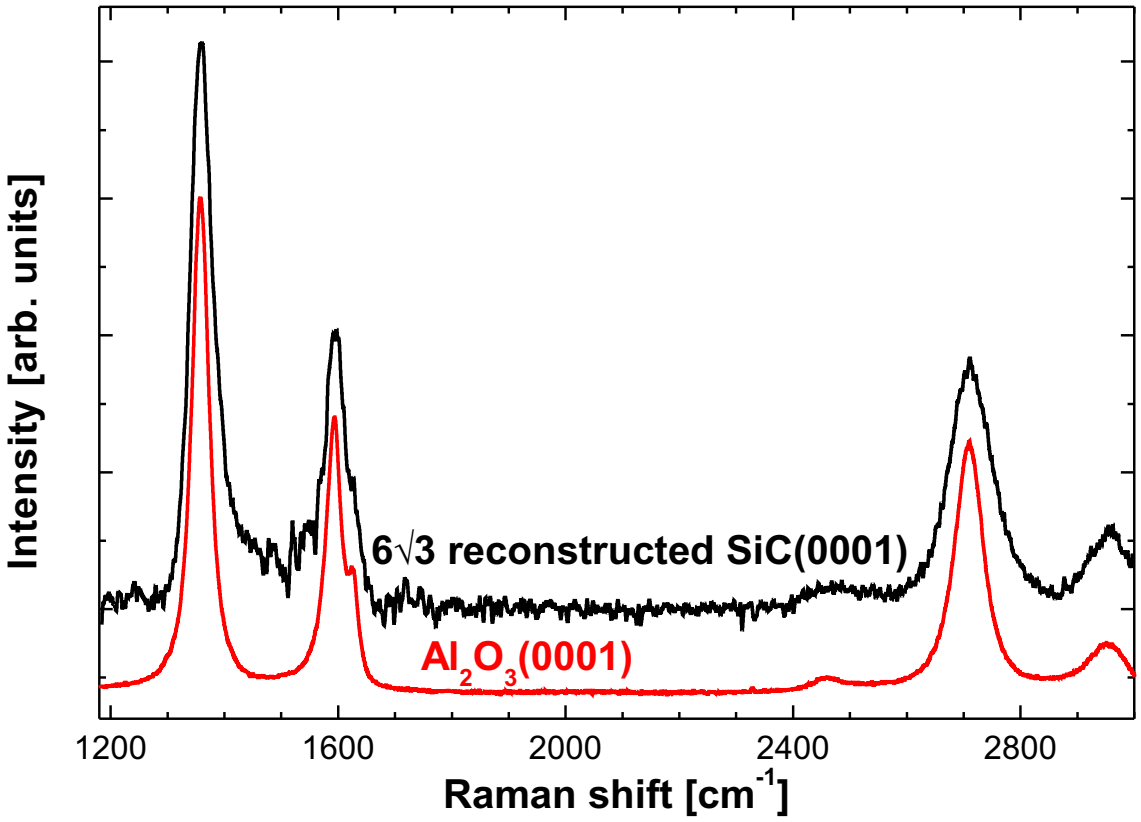

Figure 4.21: Representative Raman spectra obtained from nanocrystalline graphene layers synthesized at $T_S = 900\,°C$ and $\Delta t = 240$ min on Al_2O_3 (red) and $6\sqrt{3}$–reconstructed SiC (black). Both spectra are normalized in respect to their G peak and shifted against each other for better visibility.

While the intensity ratios of the peaks are fairly similar, the widths of the peaks are narrower in case of growth on sapphire. This also manifests itself in the determined sizes of the nanocrystalline graphene domains (compare Figs 4.4 and 4.14). On Al_2O_3, the domains reach a size (as determined by Raman) of up to ∼30 nm (at $T_S = 1000\,°C$) while in case of growth on the buffer layer, the domains reach sizes of ∼15 nm (at $T_S = 950\,°C$).

Regarding the GID experiments, another scenario is displayed. The widths of the diffraction peaks are smaller for the films grown on the buffer layer, compared with films synthesized on Al_2O_3, both in radial as well as in angular direction (see Figs. 4.8, 4.9, 4.18 and 4.20). This implies that graphene domains grown on the buffer layer possess a higher degree of in-plane ordering.

These observations can be explained as followed: since the buffer layer provides a quasi-homoepitaxial substrate for graphene growth, the epitaxial alignment of the domains is narrower, because film and substrate are lattice matched. No coalescence of individually nucleated domains takes place (or only with a high amount of defects in the region of the grain boundaries). Therefore, the in-plane ordering only plays a minor role in the resulting domain sizes. Rather processes in the nucleation phase may play a much more prominent role. The size of a domain depends only on the distance between its nucleation center to the neighboring nucleation center. The nucleation density is generally dependent on the diffusion length of the adatoms on the substrate, and their sticking coefficient. At higher substrate temperatures, the sticking coefficient (or surface lifetime τ) is lower,[186–188] and surface diffusion coefficient is higher.[188,189] The surface lifetime and surface diffusion coefficient determine the surface diffusion length. The separation between nucleation centers increases with higher temperatures,[189] which is consistent with the observation that the structural quality of the graphene layers increases with increasing substrate temperature [see Fig. 4.12 and Fig. 4.13 (a)].

Also defects, impurities, or surface steps on the substrate play a role, since nucleation is enhanced at these sites.[190,191]

Therefore, one can conclude that either the defect density is higher on the buffer layer than on Al_2O_3, or the diffusion length is higher on Al_2O_3. Surface steps probably play a less important role, since the sizes of atomically-flat terraces are on the order of several microns [buffer layer, see e.g. Fig. 3.7 (a)] or several hundreds of nano meter (Al_2O_3, AFM images not shown here), respectively. Also other nucleation mechanisms might play a role. As suggested by Lippert *et al.*[192] (for the case of growth on Mica) and Jerng *et al.*[163] (growth on Al_2O_3), some carbon atoms of graphene bind covalently to atoms from the substrate and hence no pure van-der-Waals growth take place. In the case of MBE growth on mica,[192] graphene island with domain sizes on the order of microns could be grown, but the substrate is not completely covered. This suggests that the diffusion length of C atoms on mica is very large and/or the sticking coefficient of them is very low. Therefore, only few graphene nucleation centers exist on the substrate (which probably coincide with surface defects), and the graphene domains can grow to these comparably large domain sizes.

Implications on future approaches and requirements for MBE growth of graphene will be discussed in Chapter 5, 'Conclusions and outlook'.

5. Conclusion and outlook

In this chapter, the results of this thesis are briefly summarized, and an outlook for further experiments and approaches will be given, based on the results obtained so far.

Conclusion

In this work, the synthesis of graphene on (semi-) insulating substrates was investigated and the resulting graphene films were characterized. Two different methods were employed which allow the possibility to directly grow graphene on substrate which might be used for further device processing without the need of transferring the graphene subsequent to synthesis.

By surface Si depletion of SiC substrates, monolayer graphene films can be grown with high structural quality and reasonable charge carrier mobilities. The influence of surface steps of the substrate on the graphene growth was investigated. We showed that the initial SiC surface morphology has little influence on the final morphology after graphene growth. A step bunching process occurs and the sample surface after graphene growth consists of µm-sized terraces with steps in between them. If the SiC surface prior to growth also possesses a similar morphology, additional step bunching is suppressed. Since the formation of these surface steps cannot be avoided by our process, their influence on the transport properties was investigated. While transport across surface steps is not altered dramatically at low magnetic fields, a strong increase in resistance is observed at high magnetic fields. We schematically explained that behavior via a model, based on inter-Landau level mixing in the step edge regions, which enhances electron backscattering.

The structure of epitaxial graphene, the buffer layer, and oxygen intercalated graphene was investigated by grazing incidence X-ray diffraction. Epitaxial graphene is in-plane aligned to the SiC substrate, and compressively strained by 0.2 %. By oxygen intercalation the strain is released, resulting in unstrained bilayer graphene. The buffer layer possesses a different lattice constant, depending on whether it is located underneath an EG layer or not. This indicates that the $6\sqrt{3}$–reconstruction does not persist unaltered during EG growth. That is in opposition to many other studies,[113] but supporting recent results obtained by TEM.[151]

The feasibility of growing EG on C-face SiC was investigated by varying the growth parameters and the growth environment. To date, we could not synthesize homogeneous graphene layers, but the results suggest that the quality and homogeneity may be increased by redesigning the cap used for confinement.

Molecular beam epitaxy of graphene on insulating substrates (sapphire and BL/SiC) has been demonstrated. Graphene films were grown with a high control of the layer thickness. The graphene consists of nanocrystalline domains with diameters of about 30 nm. The nanocrystallites possess a common in-plane orientation and are aligned with the respective substrate. The graphene grown on the BL has a lattice parameter smaller

than that of relaxed graphite, which is explained by the presence of point defects within the film.

In conclusion, we find that epitaxial graphene on SiC is suitable for applications which require graphene on an insulating substrate, but the surface morphology has to be considered since surface steps can have a strong influence on the magnetotransport properties.

MBE is a promising method to grow mono- or few-layer graphene on different substrates. The quality of the films still has to be increased

Outlook

During the synthesis of EG on SiC, the growth starts at the surface step edges. This can be exploited in order to form graphene nanoribbons (GNR). We started working on this subject and were able to grow GNRs with widths ranging from 50 nm to 300 nm at the step edges. In the future, we aim to produce GNRs on prepatterned surfaces, in order to gain control over the position and to produce GNRs in uniform arrays, similar to what was demonstrated by Sprinkle *et al.*[46] By using the oxygen intercalation process, not only mono- but also bilayer graphene nanoribbons can be synthesized.

For the growth of graphene by MBE, the structural quality and domain sizes of graphene still has to be increased. A co-deposition of Ni together with carbon might lead to an increased diffusion length of the C atoms on the surface and thereby to larger domain sizes, first experiments are currently in progress.

Another planned approach is to utilize hexagonal boron nitride (hBN) as substrate material. First experiments are ongoing to grow this material. In the future, also the direct growth of heterostructures is planned, e.g. hBN/graphene/hBN. Since we showed that graphene can grow epitaxially on substrates, it might be possible to grow heterostructures or multilayer graphene with a defined stacking order. Theoretic calculations predict that this will lead to an opening of a bandgap in graphene, what would make it suitable for transistor applications.

A. Appendix A: The (Quantum) Hall effect

The Hall effect

In this appendix, the concept of the Hall- and the quantum Hall effect (QHE) is briefly explained and important formulas are derived. Specific aspects of QHE in graphene are addressed in the respective Section 3.3.

The Hall effect is observed when a current is driven through a (semi-)conductor in a magnetic field, the Hall voltage can be measured perpendicular to the current, as well as to the magnetic field. From measurements of the Hall effect, the type and concentration of charge carriers can be determined, as well as their mobility. The following derivation of the Hall effect was adapted from [193].

A schematic of a measurement of the Hall effect is depicted in Fig. A.1.

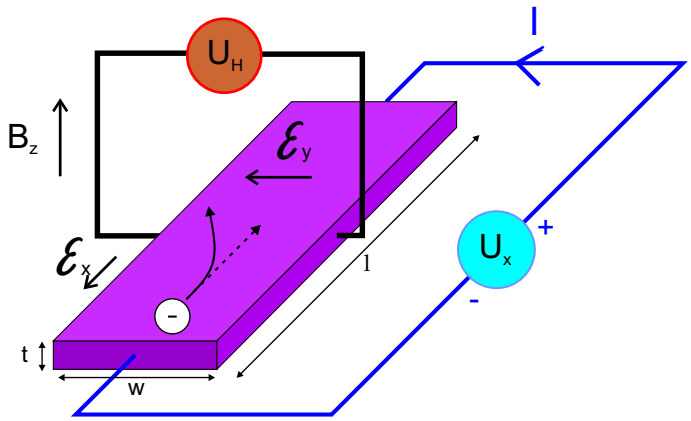

Figure A.1: Schematic of a measurement of the Hall effect.

A current I is driven in x-direction through a Hall bar with the width w, thickness t and length l. A magnetic field B is applied in z-direction and the Hall voltage is measured in y-direction. Electrons, which travel in x-direction with the drift velocity v_x, are affected by the Lorentz force. Since the Hall voltage V_H is measured without a current flowing, an electric field in y-direction builds up which compensates the Lorentz force on the electrons:

$$F_y = -e(\boldsymbol{v} \times \boldsymbol{B})_y - e\mathcal{E}_y = ev_xB - e\mathcal{E}_y = 0. \tag{A.1}$$

Here $\mathcal{E}_y = U_H/t$ is the Hall field. Assuming that the complete current is provided only by electrons with a charge e and a density n, the current density can be expressed as:

$$j_x = I/(tw) = -nev_x, \tag{A.2}$$

and therefore, using Equations A.1 and A.2:

$$\mathcal{E}_y = \frac{U_H}{w} = v_xB = -\frac{1}{ne}j_xB = -\frac{1}{ne}\frac{IB}{tw}. \tag{A.3}$$

The quantity $-1/(ne)$ is called Hall coefficient (A_{H}) and can be determined by the measurements of U_{H}, I and B via

$$U_{\mathrm{H}} = A_{\mathrm{H}} IB/t. \tag{A.4}$$

The sign of the Hall coefficient gives the type of charge carriers, negative for electrons and positive for holes. Note that in case of graphene, the thickness t is not a useful quantity, therefore the charge carrier density is given in per area, not per volume.

Via the relation of the conductivity σ with the charge carrier mobility μ:

$$\sigma = ne\mu, \tag{A.5}$$

μ can be derived from measurements of the Hall constant and the conductivity at zero magnetic field:

$$\mu = \left| \frac{\sigma}{A_{\mathrm{H}}} \right| \tag{A.6}$$

The quantum Hall effect

The following derivation of the quantum Hall effect is adapted from [130].

The quantum Hall effect arises at high magnetic fields and (usually) at low temperatures, when the charge carriers then condense in Landau levels. The number of states per Landau level (in case of no degeneracy) is given by:

$$N_L = eB/h, \tag{A.7}$$

where h is Planck's constant.

If the density of states is zero at the Fermi energy, carriers cannot be scattered and longitudinal resistivity approaches zero. The Hall conductivity is then the inverse of the Hall resistance ($R_H = U_H/I$) and is given by:

$$\sigma_{xy} = -ne/B. \tag{A.8}$$

When a landau level is fully occupied and $n = \nu N_L$ (where ν denotes the filling factor and is an integer), it directly follows from eq. A.7 and A.8 that:

$$-\sigma_{xy} = e^2\nu/h, \tag{A.9}$$

and therefore the quantized Hall resistances can be expressed as

$$R_{\mathrm{H}} = h/(\nu e^2). \tag{A.10}$$

The factor h/e^2 is a constant, usually referred to as *von Klitzing constant* or R_{K}, and possesses a value of $\sim 25.81\,\mathrm{k\Omega}$.

Bibliography

[1] R. W. Keyes. *Physical limits of silicon transistors and circuits*. Reports Prog. Phys., **68** (12): 2701–2746 (2005). doi:10.1088/0034-4885/68/12/R01.

[2] K. S. Novoselov, A. K. Geim, S. V. Morozov, D. Jiang, Y. Zhang, S. V. Dubonos, I. V. Grigorieva, and A. A. Firsov. *Electric field effect in atomically thin carbon films.* Science, **306** (5696): 666–9 (2004). doi:10.1126/science.1102896.

[3] S. Morozov, K. S. Novoselov, M. Katsnelson, F. Schedin, D. Elias, J. Jaszczak, and A. K. Geim. *Giant Intrinsic Carrier Mobilities in Graphene and Its Bilayer*. Phys. Rev. Lett., **100** (1): 11–14 (2008). doi:10.1103/PhysRevLett.100.016602.

[4] L. Vicarelli, M. S. Vitiello, D. Coquillat, A. Lombardo, a. C. Ferrari, W. Knap, M. Polini, V. Pellegrini, and A. Tredicucci. *Graphene field-effect transistors as room-temperature terahertz detectors.* Nat. Mater., **11** (10): 865–71 (2012). doi:10.1038/nmat3417.

[5] S. Bae, H. Kim, Y. Lee, X. Xu, J.-S. Park, Y. Zheng, J. Balakrishnan, T. Lei, H. R. Kim, Y. I. Song, Y.-J. Kim, K. S. Kim, B. Ozyilmaz, J.-H. Ahn, B. H. Hong, and S. Iijima. *Roll-to-roll production of 30-inch graphene films for transparent electrodes.* Nat. Nanotechnol., **5** (8): 574–8 (2010). doi:10.1038/nnano.2010.132.

[6] Y. Shao, J. Wang, H. Wu, J. Liu, I. A. Aksay, and Y. Lin. *Graphene Based Electrochemical Sensors and Biosensors: A Review*. Electroanalysis, **22** (10): 1027–1036 (2010). doi:10.1002/elan.200900571.

[7] F. Xia, T. Mueller, Y.-M. Lin, A. Valdes-Garcia, and P. Avouris. *Ultrafast graphene photodetector.* Nat. Nanotechnol., **4** (12): 839–43 (2009). doi:10.1038/nnano.2009.292.

[8] L. Huang, Y. Huang, J. Liang, X. Wan, and Y. Chen. *Graphene-based conducting inks for direct inkjet printing of flexible conductive patterns and their applications in electric circuits and chemical sensors*. Nano Res., **4** (7): 675–684 (2011). doi:10.1007/s12274-011-0123-z.

[9] J. S. Bunch, A. M. van der Zande, S. S. Verbridge, I. W. Frank, D. M. Tanenbaum, J. M. Parpia, H. G. Craighead, and P. L. McEuen. *Electromechanical resonators from graphene sheets.* Science, **315** (5811): 490–3 (2007). doi:10.1126/science.1136836.

[10] C. Berger, Z. Song, T. Li, X. Li, A. Y. Ogbazghi, R. Feng, Z. Dai, A. N. Marchenkov, E. H. Conrad, P. N. First, and W. A. de Heer. *Ultrathin Epitaxial Graphite: 2D Electron Gas Properties and a Route toward Graphene-based Nanoelectronics*. J. Phys. Chem. B, **108** (52): 19912–19916 (2004). doi:10.1021/jp040650f.

[11] K. V. Emtsev, A. Bostwick, K. Horn, J. Jobst, G. L. Kellogg, L. Ley, J. L. McChesney, T. Ohta, S. A. Reshanov, J. Röhrl, E. Rotenberg, A. K. Schmid, D. Waldmann, H. B. Weber, and T. Seyller. *Towards wafer-size graphene layers by atmo-*

spheric pressure graphitization of silicon carbide. Nat. Mater., **8** (3): 203–7 (2009). doi: 10.1038/nmat2382.

[12] Wikimedia Commons. *https://en.wikipedia.org/wiki/File:Graphen.jpg* (accessed 03 February 2014).

[13] P. R. Wallace. *The Band Theory of Graphite*. Phys. Rev., **71** (9): 622–634 (1947). doi: 10.1103/PhysRev.71.622.

[14] H. P. Boehm, A. Clauss, and U. Hofmann. *Dünnste Kohlenstoff-Folien*. Zeitschrift für Naturforsch., **70** (b): 150–153 (1962).

[15] K. S. Novoselov, A. K. Geim, S. V. Morozov, D. Jiang, M. I. Katsnelson, I. V. Grigorieva, S. V. Dubonos, and A. A. Firsov. *Two-dimensional gas of massless Dirac fermions in graphene.* Nature, **438** (7065): 197–200 (2005). doi:10.1038/nature04233.

[16] Thomas Reuters *Web of science*. *http://isiknowledge.com* (2013).

[17] J. C. Charlier, J. P. Michenaud, and X. Gonze. *First-principles study of the electronic properties of simple hexagonal graphite*. Phys. Rev. B, **46** (8): 4531–4539 (1992). doi: 10.1103/PhysRevB.46.4531.

[18] A. H. Castro Neto, F. Guinea, N. Peres, K. S. Novoselov, and A. K. Geim. *The electronic properties of graphene*. Rev. Mod. Phys., **81** (1): 109–162 (2009). doi:10. 1103/RevModPhys.81.109.

[19] S. Reich, J. Maultzsch, C. Thomsen, and P. Ordejón. *Tight-binding description of graphene*. Phys. Rev. B, **66** (3): 035412 (2002). doi:10.1103/PhysRevB.66.035412.

[20] H. Hattab, A. T. N'Diaye, D. Wall, C. Klein, G. Jnawali, J. Coraux, C. Busse, R. van Gastel, B. Poelsema, T. Michely, F.-J. Meyer zu Heringdorf, and M. Horn-von Hoegen. *Interplay of wrinkles, strain, and lattice parameter in graphene on iridium.* Nano Lett., **12** (2): 678–82 (2012). doi:10.1021/nl203530t.

[21] J. W. Anthony, R. A. Bideaux, K. W. Bladh, and M. C. Nichols. *Handbook of Mineralogy, Elements, Sulfides and Sulfosalts*. Mineral Data Pub (1990).

[22] D. W. Brenner, O. A. Shenderova, J. A. Harrison, S. J. Stuart, B. Ni, and S. B. Sinnott. *A second-generation reactive empirical bond order (REBO) potential energy expression for hydrocarbons*. J. Phys. Condens. Matter, **14** (4): 783–802 (2002). doi:10.1088/ 0953-8984/14/4/312.

[23] C. Lee, X. Wei, J. W. Kysar, and J. Hone. *Measurement of the elastic properties and intrinsic strength of monolayer graphene.* Science, **321** (5887): 385–8 (2008). doi:10. 1126/science.1157996.

[24] *http://personal.monm.edu/gebauer_peter/chem_230/Lect_pages/Bruice_jpgs &pgs/sp2_hybrids.htm, accessed 31. October 2013.*

[25] Y. H. Wu, T. Yu, and Z. X. Shen. *Two-dimensional carbon nanostructures: Fundamental properties, synthesis, characterization, and potential applications*. J. Appl. Phys., **108** (7): 071301 (2010). doi:10.1063/1.3460809.

[26] R. Deacon, K.-C. Chuang, R. Nicholas, K. Novoselov, and A. Geim. *Cyclotron resonance study of the electron and hole velocity in graphene monolayers*. Phys. Rev. B, **76** (8): 081406 (2007). doi:10.1103/PhysRevB.76.081406.

[27] G. Li and E. Y. Andrei. *Observation of Landau levels of Dirac fermions in graphite*. Nat. Phys., **3** (9): 623–627 (2007). doi:10.1038/nphys653.

[28] M. Orlita, C. Faugeras, P. Plochocka, P. Neugebauer, G. Martinez, D. K. Maude, A.-L. Barra, M. Sprinkle, C. Berger, W. a. de Heer, and M. Potemski. *Approaching the Dirac Point in High-Mobility Multilayer Epitaxial Graphene*. Phys. Rev. Lett., **101** (26): 1–4 (2008).

[29] Y. Zhang, Y.-W. Tan, H. L. Stormer, and P. Kim. *Experimental observation of the quantum Hall effect and Berry's phase in graphene.* Nature, **438** (7065): 201–4 (2005). doi:10.1038/nature04235.

[30] X. Wu, Y. Hu, M. Ruan, N. K. Madiomanana, J. Hankinson, M. Sprinkle, C. Berger, and W. A. de Heer. *Half integer quantum Hall effect in high mobility single layer epitaxial graphene*. Appl. Phys. Lett., **95** (22): 223108 (2009). doi:10.1063/1.3266524.

[31] P. J. Zomer, M. H. D. Guimarães, N. Tombros, and B. J. van Wees. *Long-distance spin transport in high-mobility graphene on hexagonal boron nitride*. Phys. Rev. B, **86** (16): 161416 (2012). doi:10.1103/PhysRevB.86.161416.

[32] A. K. Geim and K. S. Novoselov. *The rise of graphene.* Nat. Mater., **6** (3): 183–91 (2007). doi:10.1038/nmat1849.

[33] K. S. Novoselov. *Nobel Lecture: Graphene: Materials in the Flatland*. Rev. Mod. Phys., **83** (3): 837–849 (2011). doi:10.1103/RevModPhys.83.837.

[34] V. Singh, D. Joung, L. Zhai, S. Das, S. I. Khondaker, and S. Seal. *Graphene based materials: Past, present and future*. Prog. Mater. Sci., **56** (8): 1178–1271 (2011). doi:10.1016/j.pmatsci.2011.03.003.

[35] M. Tamagnone, J. S. Go´mez-Di´az, J. R. Mosig, and J. Perruisseau-Carrier. *Reconfigurable terahertz plasmonic antenna concept using a graphene stack*. Appl. Phys. Lett., **101** (21): 214102 (2012). doi:10.1063/1.4767338.

[36] Y. Zhang, T.-T. Tang, C. Girit, Z. Hao, M. C. Martin, A. Zettl, M. F. Crommie, Y. R. Shen, and F. Wang. *Direct observation of a widely tunable bandgap in bilayer graphene.* Nature, **459** (7248): 820–3 (2009). doi:10.1038/nature08105.

[37] T. Ohta, A. Bostwick, T. Seyller, K. Horn, and E. Rotenberg. *Controlling the electronic structure of bilayer graphene.* Science (80-.)., **313** (5789): 951–4 (2006). doi:10.1126/science.1130681.

[38] J. B. Oostinga, H. B. Heersche, X. Liu, A. F. Morpurgo, and L. M. K. Vandersypen. *Gate-induced insulating state in bilayer graphene devices.* Nat. Mater., **7** (2): 151–7 (2008). doi:10.1038/nmat2082.

[39] E. V. Castro, K. S. Novoselov, S. V. Morozov, N. M. R. Peres, J. M. B. Lopes dos Santos, J. Nilsson, F. Guinea, A. K. Geim, and A. H. Castro Neto. *Biased Bilayer Graphene: Semiconductor with a Gap Tunable by the Electric Field Effect*. Phys. Rev. Lett., **99** (21): 216802 (2007). doi:10.1103/PhysRevLett.99.216802.

[40] M. Ostler, I. Deretzis, S. Mammadov, F. Giannazzo, G. Nicotra, C. Spinella, T. Seyller, and A. La Magna. *Direct growth of quasi-free-standing epitaxial graphene on nonpolar SiC surfaces*. Phys. Rev. B, **88** (8): 085408 (2013). doi:10.1103/PhysRevB.88.085408.

[41] S. Y. Zhou, G.-H. Gweon, A. V. Fedorov, P. N. First, W. A. de Heer, D.-H. Lee, F. Guinea, A. H. Castro Neto, and A. Lanzara. *Substrate-induced bandgap opening in epitaxial graphene.* Nat. Mater., **6** (10): 770–5 (2007). doi:10.1038/nmat2003.

[42] G. Giovannetti, P. Khomyakov, G. Brocks, P. Kelly, and J. van den Brink. *Substrate-induced band gap in graphene on hexagonal boron nitride: Ab initio density functional calculations*. Phys. Rev. B, **76** (7): 073103 (2007). doi:10.1103/PhysRevB.76.073103.

[43] Y.-W. Son, M. Cohen, and S. Louie. *Energy Gaps in Graphene Nanoribbons*. Phys. Rev. Lett., **97** (21): 1–4 (2006). doi:10.1103/PhysRevLett.97.216803.

[44] J. Baringhaus, M. Ruan, F. Edler, A. Tejeda, M. Sicot, A.-P. Li, Z. Jiang, E. H. Conrad, C. Berger, C. Tegenkamp, and W. A. de Heer. *Exceptional ballistic transport in epitaxial graphene nanoribbons*. Nature, **506** (7488): 349–354 (2014). doi:10.1038/nature12952.

[45] P. Ruffieux, J. Cai, N. C. Plumb, L. Patthey, D. Prezzi, A. Ferretti, E. Molinari, X. Feng, K. Müllen, C. A. Pignedoli, and R. Fasel. *Electronic structure of atomically precise graphene nanoribbons.* ACS Nano, **6** (8): 6930–5 (2012). doi:10.1021/nn3021376.

[46] M. Sprinkle, M. Ruan, Y. Hu, J. Hankinson, M. Rubio-Roy, B. Zhang, X. Wu, C. Berger, and W. A. de Heer. *Scalable templated growth of graphene nanoribbons on SiC.* Nat. Nanotechnol., **5** (10): 727–31 (2010). doi:10.1038/nnano.2010.192.

[47] D. V. Kosynkin, A. L. Higginbotham, A. Sinitskii, J. R. Lomeda, A. Dimiev, B. K. Price, and J. M. Tour. *Longitudinal unzipping of carbon nanotubes to form graphene nanoribbons.* Nature, **458** (7240): 872–6 (2009). doi:10.1038/nature07872.

[48] N. M. R. Peres. *The transport properties of graphene.* J. Phys. Condens. Matter, **21** (32): 323201 (2009). doi:10.1088/0953-8984/21/32/323201.

[49] M. I. Katsnelson, K. S. Novoselov, and A. K. Geim. *Chiral tunnelling and the Klein paradox in graphene*. Nat. Phys., **2** (9): 620–625 (2006). doi:10.1038/nphys384.

[50] A. K. Geim. *Graphene: status and prospects.* Science (80-.)., **324** (5934): 1530–4 (2009). doi:10.1126/science.1158877.

[51] M. J. Allen, V. C. Tung, and R. B. Kaner. *Honeycomb carbon: a review of graphene.* Chem. Rev., **110** (1): 132–45 (2010). doi:10.1021/cr900070d.

[52] K. S. Novoselov, V. I. Fal'ko, L. Colombo, P. R. Gellert, M. G. Schwab, and K. Kim. *A roadmap for graphene.* Nature, **490** (7419): 192–200 (2012). doi:10.1038/nature11458.

[53] P. Avouris, Z. Chen, and V. Perebeinos. *Carbon-based electronics.* Nat. Nanotechnol., **2** (10): 605–15 (2007). doi:10.1038/nnano.2007.300.

[54] Youtube. *http://www.youtube.com/watch?v=waO020l25sU, accessed 22. April 2013* (2011).

[55] Y. Zhang, L. Zhang, and C. Zhou. *Review of Chemical Vapor Deposition of Graphene and Related Applications.* Acc. Chem. Res. (2013). doi:10.1021/ar300203n.

[56] X. Li, W. Cai, J. An, S. Kim, J. Nah, D. Yang, R. Piner, A. Velamakanni, I. Jung, E. Tutuc, S. K. Banerjee, L. Colombo, and R. S. Ruoff. *Large-area synthesis of high-quality and uniform graphene films on copper foils.* Science, **324** (5932): 1312–4 (2009). doi:10.1126/science.1171245.

[57] Y. Lee, S. Bae, H. Jang, S. Jang, S.-E. Zhu, S. H. Sim, Y. I. Song, B. H. Hong, and J.-H. Ahn. *Wafer-scale synthesis and transfer of graphene films.* Nano Lett., **10** (2): 490–3 (2010). doi:10.1021/nl903272n.

[58] Y. Gamo, A. Nagashima, M. Wakabayashi, M. Terai, and C. Oshima. *Atomic structure of monolayer graphite formed on Ni(111).* Surf. Sci., **374** (1-3): 61–64 (1997). doi:10.1016/S0039-6028(96)00785-6.

[59] T. A. Land, T. Michely, R. J. Behm, J. C. Hemminger, and G. Comsa. *STM investigation of single layer graphite structures produced on Pt(111) by hydrocarbon decomposition*. Surf. Sci., **264** (3): 261–270 (1992). doi:10.1016/0039-6028(92)90183-7.

[60] C. Oshima and A. Nagashima. *Ultra-thin epitaxial films of graphite and hexagonal boron nitride on solid surfaces*. J. Phys. Condens. Matter, **9** (1): 1–20 (1997). doi:10.1088/0953-8984/9/1/004.

[61] P. W. Sutter, J.-I. Flege, and E. Sutter. *Epitaxial graphene on ruthenium.* Nat. Mater., **7** (5): 406–11 (2008). doi:10.1038/nmat2166.

[62] J. Coraux, A. T. N'Diaye, M. Engler, C. Busse, D. Wall, N. Buckanie, F.-J. Meyer zu Heringdorf, R. van Gastel, B. Poelsema, and T. Michely. *Growth of graphene on Ir(111).* New J. Phys., **11** (2): 023006 (2009). doi:10.1088/1367-2630/11/2/023006.

[63] M. A. Fanton, J. A. Robinson, C. Puls, Y. Liu, M. J. Hollander, B. E. Weiland, M. Labella, K. Trumbull, R. Kasarda, C. Howsare, J. Stitt, and D. W. Snyder. *Characterization of graphene films and transistors grown on sapphire by metal-free chemical vapor deposition.* ACS Nano, **5** (10): 8062–9 (2011). doi:10.1021/nn202643t.

[64] R. M. Tromp and J. B. Hannon. *Thermodynamics and Kinetics of Graphene Growth on SiC(0001).* Phys. Rev. Lett., **102** (10): 106104 (2009). doi:10.1103/PhysRevLett.102.106104.

[65] K. V. Emtsev, T. Seyller, F. Speck, L. Ley, P. Stojanov, J. D. Riley, and R. C. G. Leckey. *Initial Stages of the Graphite-SiC(0001) Interface Formation Studied by Photoelectron Spectroscopy*. Mater. Sci. Forum, **556-557** (0001): 525–528 (2007). doi:10.4028/www.scientific.net/MSF.556-557.525.

[66] F. Fromm, M. H. Oliveira Jr, A. Molina-Sánchez, M. Hundhausen, J. M. J. Lopes, H. Riechert, L. Wirtz, and T. Seyller. *Contribution of the buffer layer to the Raman spectrum of epitaxial graphene on SiC(0001).* New J. Phys., **15** (4): 043031 (2013). doi:10.1088/1367-2630/15/4/043031.

[67] M. Hashimoto, A. Trampert, J. Herfort, and K. H. Ploog. *Atomic ordering and interlayer diffusion of Co_2FeSi films grown on GaAs(001) studied by transmission electron microscopy*. J. Vac. Sci. Technol. B Microelectron. Nanom. Struct., **25** (4): 1453 (2007). doi:10.1116/1.2748413.

[68] L. Qiu, J. Z. Liu, S. L. Y. Chang, Y. Wu, and D. Li. *Biomimetic superelastic graphene-based cellular monoliths.* Nat. Commun., **3**: 1241 (2012). doi:10.1038/ncomms2251.

[69] Y. Kim, J. Lee, M. S. Yeom, J. W. Shin, H. Kim, Y. Cui, J. W. Kysar, J. Hone, Y. Jung, S. Jeon, and S. M. Han. *Strengthening effect of single-atomic-layer graphene in metal-graphene nanolayered composites.* Nat. Commun., **4**: 2114 (2013). doi:10.1038/ncomms3114.

[70] HTM Sport GmbH. *http://head.com/g/eu/graphene/* (accessed 29 January 2014).

[71] A. M. van der Zande, R. A. Barton, J. S. Alden, C. S. Ruiz-Vargas, W. S. Whitney, P. H. Q. Pham, J. Park, J. M. Parpia, H. G. Craighead, and P. L. McEuen. *Large-Scale Arrays of Single-Layer Graphene Resonators*. Nano Lett., p. 101116125413000 (2010). doi:10.1021/nl102713c.

[72] R. R. Nair, P. Blake, A. N. Grigorenko, K. S. Novoselov, T. J. Booth, T. Stauber, N. M. R. Peres, and A. K. Geim. *Fine structure constant defines visual transparency of graphene.* Science, **320** (5881): 1308 (2008). doi:10.1126/science.1156965.

[73] M. Ostler, F. Speck, M. Gick, and T. Seyller. *Automated preparation of high-quality epitaxial graphene on 6H-SiC(0001)*. Phys. Status Solidi, **247** (11-12): 2924–2926 (2010). doi:10.1002/pssb.201000220.

[74] J. R. Arthur. *Molecular beam epitaxy*. Surf. Sci., **500** (1-3): 189–217 (2002). doi:10.1016/S0039-6028(01)01525-4.

[75] M. A. Herman and H. Sitter. *Molecular Beam Epitaxy: Fundamentals and Current Status (Springer Series in Materials Science , Vol 7)*. Springer, Berlin, 2nd ed. (1996).

[76] E. H. C. Parker. *The Technology and Physics of Molecular Beam Epitaxy*. Plenum Press (1985).

[77] CreaTec Fischer & Co. GmbH. *http://www.createc.de/uhv-growth-and-analysis/mbe-uhv-systems/manipulators* (accessed 13 November 2013).

[78] Dr. Eberl MBE-Komponenten GmbH. *http://www.mbe-komponenten.de/products/mbe-components/effusion-cells/suko.php* (accessed 13 November 2013).

[79] R. E. Finnigan. *Quadrupole mass spectrometers*. Anal. Chem., **66** (19): 969A–975A (1994). doi:10.1021/ac00091a002.

[80] R. Loudon. *The Raman effect in crystals*. Adv. Phys., **50** (7): 813–864 (2001). doi:10.1080/00018730110101395.

[81] F. Tuinstra and J. L. Koenig. *Raman Spectrum of Graphite*. J. Chem. Phys., **53** (3): 1126 (1970). doi:10.1063/1.1674108.

[82] A. C. Ferrari, J. Meyer, V. Scardaci, C. Casiraghi, M. Lazzeri, F. Mauri, S. Piscanec, D. Jiang, K. S. Novoselov, S. Roth, and A. K. Geim. *Raman Spectrum of Graphene and Graphene Layers*. Phys. Rev. Lett., **97** (18): 187401 (2006). doi:10.1103/PhysRevLett.97.187401.

[83] A. C. Ferrari. *Raman spectroscopy of graphene and graphite: Disorder, electron–phonon coupling, doping and nonadiabatic effects*. Solid State Commun., **143** (1-2): 47–57 (2007). doi:10.1016/j.ssc.2007.03.052.

[84] L. M. Malard, M. A. Pimenta, G. Dresselhaus, and M. S. Dresselhaus. *Raman spectroscopy in graphene*. Phys. Rep., **473** (5-6): 51–87 (2009). doi:10.1016/j.physrep.2009.02.003.

[85] A. C. Ferrari and D. M. Basko. *Raman spectroscopy as a versatile tool for studying the properties of graphene*. Nat. Nanotechnol., **8** (4): 235–246 (2013). doi:10.1038/nnano.2013.46.

[86] C. V. Raman. *A new radiation*. Indian J. Phys., **398** (March): 368–376 (1928).

[87] A. Eckmann, A. Felten, A. Mishchenko, L. Britnell, R. Krupke, K. S. Novoselov, and C. Casiraghi. *Probing the nature of defects in graphene by Raman spectroscopy.* Nano Lett., **12** (8): 3925–30 (2012). doi:10.1021/nl300901a.

[88] T. M. G. Mohiuddin, A. Lombardo, R. R. Nair, A. Bonetti, G. Savini, R. Jalil, N. Bonini, D. M. Basko, C. Galiotis, N. Marzari, K. S. Novoselov, A. K. Geim, and A. C. Ferrari. *Uniaxial strain in graphene by Raman spectroscopy: G peak splitting, Grüneisen parameters, and sample orientation*. Phys. Rev. B, **79** (20): 205433 (2009). doi:10.1103/PhysRevB.79.205433.

[89] M. Mohr, J. Maultzsch, and C. Thomsen. *Splitting of the Raman 2D band of graphene subjected to strain*. Phys. Rev. B, **82** (20): 1–4 (2010). doi:10.1103/PhysRevB.82.201409.

[90] J. A. Robinson, C. Puls, N. E. Staley, J. Stitt, M. A. Fanton, K. V. Emtsev, T. Seyller, and Y. Liu. *Raman topography and strain uniformity of large-area epitaxial graphene*. Nano Lett., **9** (3): 964–968 (2009). doi:10.1021/nl802852p.

[91] D. M. Basko, S. Piscanec, and A. C. Ferrari. *Electron-electron interactions and doping dependence of the two-phonon Raman intensity in graphene*. Phys. Rev. B, **80** (16): 165413 (2009). doi:10.1103/PhysRevB.80.165413.

[92] L. G. Canc¸ado, K. Takai, T. Enoki, M. Endo, Y. A. Kim, H. Mizusaki, A. Jorio, L. N. Coelho, R. Magalha es Paniago, and M. A. Pimenta. *General equation for the determination of the crystallite size L[sub a] of nanographite by Raman spectroscopy*. Appl. Phys. Lett., **88** (16): 163106 (2006). doi:10.1063/1.2196057.

[93] L. G. Cançado, A. Jorio, and M. Pimenta. *Measuring the absolute Raman cross section of nanographites as a function of laser energy and crystallite size*. Phys. Rev. B, **76** (6): 064304 (2007). doi:10.1103/PhysRevB.76.064304.

[94] M. H. Oliveira Jr., T. Schumann, R. Gargallo-Caballero, F. Fromm, T. Seyller, M. Ramsteiner, A. Trampert, L. Geelhaar, J. M. J. Lopes, and H. Riechert. *Mono- and few-layer nanocrystalline graphene grown on Al2O3(0001) by molecular beam epitaxy*. Carbon, **56**: 339–350 (2013). doi:10.1016/j.carbon.2013.01.032.

[95] P. Venezuela, M. Lazzeri, and F. Mauri. *Theory of double-resonant Raman spectra in graphene: Intensity and line shape of defect-induced and two-phonon bands*. Phys. Rev. B, **84** (3): 035433 (2011). doi:10.1103/PhysRevB.84.035433.

[96] L. J. . Van der Pauw. *A method of measuring the resistivity and Hall coefficient on lamellae of arbitrary shape*. Philips Tech. Rev., **20** (8): 220–224 (1958).

[97] E. H. Hall. *On a New Action of the Magnet on Electric Currents*. Am. J. Math., **2** (3): 287 (1879). doi:10.2307/2369245.

[98] *Synchrotronstrahlung zur Erforschung kondensierter Materie: Vorlesungsmanuskripte des 23. IFF-Ferienkurses vom 23.3. bis 3.4.1992 im Forschungszentrum Jülich (German Edition)*. Forschungszentrum Jülich, Institut für Festkörperforschung (1992).

[99] U. Pietsch, V. Holy, and T. Baumbach. *High-Resolution X-Ray Scattering: From Thin Films to Lateral Nanostructures (Advanced Texts in Physics)*. Springer, 2nd ed. (2004).

[100] Max Planck Institut für Metallforschung, Stuttgart. *http://www.mf.mpg.de/en/abteilungen/dosch/barrena/pictures/org-lab/tr-scattering.gif* (accessed 20 December 2013).

[101] H. Morkoç, S. Strite, G. B. Gao, M. E. Lin, B. Sverdlov, and M. Burns. *Large-band-gap SiC, III-V nitride, and II-VI ZnSe-based semiconductor device technologies*. J. Appl. Phys., **76** (3): 1363 (1994). doi:10.1063/1.358463.

[102] Ioffe Physical Technical Institute. *http://www.ioffe.ru/SVA/NSM/Semicond/SiC* (accessed 13 September 2013).

[103] M. Kumagawa, H. Kuwabara, and S. Yamada. *Hydrogen Etching of Silicon Carbide*. Jpn. J. Appl. Phys., **8** (4): 421–428 (1969).

[104] A. Nakajima, H. Yokoya, Y. Furukawa, and H. Yonezu. *Step control of vicinal 6H–SiC(0001) surface by H[sub 2] etching*. J. Appl. Phys., **97** (10): 104919 (2005). doi:10.1063/1.1901838.

[105] S. Nie, C. Lee, R. M. Feenstra, Y. Ke, R. Devaty, W. Choyke, C. Inoki, T. Kuan, and G. Gu. *Step formation on hydrogen-etched 6H-SiC{0001} surfaces*. Surf. Sci., **602** (17): 2936–2942 (2008). doi:10.1016/j.susc.2008.07.021.

[106] J. Drowart, G. De Maria, and M. G. Inghram. *Thermodynamic Study of SiC Utilizing a Mass Spectrometer*. J. Chem. Phys., **29** (5): 1015 (1958). doi:10.1063/1.1744646.

[107] I. Forbeaux, J.-M. Themlin, and J.-M. Debever. *Heteroepitaxial graphite on 6H-SiC(0001): Interface formation through conduction-band electronic structure*. Phys. Rev. B, **58** (24): 16396–16406 (1998). doi:10.1103/PhysRevB.58.16396.

[108] A. Van Bommel, J. Crombeen, and A. Van Tooren. *LEED and Auger electron observations of the SiC(0001) surface*. Surf. Sci., **48** (2): 463–472 (1975). doi:10.1016/0039-6028(75)90419-7.

[109] K. Heinz, J. Bernhardt, J. Schardt, and U. Starke. *Functional surface reconstructions of hexagonal SiC*. J. Phys. Condens. Matter, **16** (17): S1705–S1720 (2004). doi:10.1088/0953-8984/16/17/013.

[110] S. Goler, C. Coletti, V. Piazza, P. Pingue, F. Colangelo, V. Pellegrini, K. V. Emtsev, S. Forti, U. Starke, F. Beltram, and S. Heun. *Revealing the atomic structure of the buffer layer between SiC(0001) and epitaxial graphene*. Carbon, **51**: 249–254 (2013). doi:10.1016/j.carbon.2012.08.050.

[111] U. Starke and C. Riedl. *Epitaxial graphene on SiC(0001) and SiC(000-1) : from surface reconstructions to carbon electronics*. J. Phys. Condens. Matter, **21** (13): 134016 (2009). doi:10.1088/0953-8984/21/13/134016.

[112] F. Ming and A. Zangwill. *Model and simulations of the epitaxial growth of graphene on non-planar 6H–SiC surfaces*. J. Phys. D. Appl. Phys., **45** (15): 154007 (2012). doi:10.1088/0022-3727/45/15/154007.

[113] K. V. Emtsev, F. Speck, T. Seyller, L. Ley, and J. Riley. *Interaction, growth, and ordering of epitaxial graphene on SiC{0001} surfaces: A comparative photoelectron spectroscopy study*. Phys. Rev. B, **77** (15): 155303 (2008). doi:10.1103/PhysRevB.77.155303.

[114] J. Hass, W. A. de Heer, and E. H. Conrad. *The growth and morphology of epitaxial multilayer graphene*. J. Phys. Condens. Matter, **20** (32): 323202 (2008). doi:10.1088/0953-8984/20/32/323202.

[115] V. Borovikov and A. Zangwill. *Step bunching of vicinal 6H-SiC{0001} surfaces*. Phys. Rev. B, **79** (24): 245413 (2009). doi:10.1103/PhysRevB.79.245413.

[116] M. Bolen, S. Harrison, . Biedermann, and M. Capano. *Graphene formation mechanisms on 4H-SiC(0001)*. Phys. Rev. B, **80** (11): 115433 (2009). doi:10.1103/PhysRevB.80.115433.

[117] G. R. Fonda. *Evaporation of tungsten under various pressures of argon*. Phys. Rev., **343** (1923): 260–266 (1928).

[118] M. H. Oliveira Jr., T. Schumann, F. Fromm, R. Koch, M. Ostler, M. Ramsteiner, T. Seyller, J. M. J. Lopes, and H. Riechert. *Formation of high-quality quasi-free-standing bilayer graphene on SiC(0001) by oxygen intercalation upon annealing in air*. Carbon, **52**: 83–89 (2013). doi:10.1016/j.carbon.2012.09.008.

[119] A. Tiberj, J. R. Huntzinger, N. Camara, P. Godignon, and J. Camassel. *Raman spectrum and optical extinction of graphene buffer layers on the Si-face of 6H-SiC* (2012).

[120] D. Waldmann, J. Jobst, F. Speck, T. Seyller, M. Krieger, and H. B. Weber. *Bottom-gated epitaxial graphene*. Nat. Mater., **10** (5): 357–360 (2011). doi:10.1038/nmat2988.

[121] J. Jobst, D. Waldmann, F. Speck, R. Hirner, D. K. Maude, T. Seyller, and H. B. Weber. *Quantum oscillations and quantum Hall effect in epitaxial graphene*. Phys. Rev. B, **81** (19): 195434 (2010). doi:10.1103/PhysRevB.81.195434.

[122] M. H. Oliveira Jr., T. Schumann, M. Ramsteiner, J. M. J. Lopes, and H. Riechert. *Influence of the silicon carbide surface morphology on the epitaxial graphene formation*. Appl. Phys. Lett., **99** (11): 111901 (2011). doi:10.1063/1.3638058.

[123] NOVASiC. *http://http://www.novasic.com/services/polishing/polishing.php, accessed 24. September 2013*.

[124] H. Nakagawa, S. Tanaka, and I. Suemune. *Self-Ordering of Nanofacets on Vicinal SiC Surfaces*. Phys. Rev. Lett., **91** (22): 226107 (2003). doi:10.1103/PhysRevLett.91.226107.

[125] S. Tanaka, K. Morita, and H. Hibino. *Anisotropic layer-by-layer growth of graphene on vicinal SiC(0001) surfaces*. Phys. Rev. B, **81** (4): 041406(R) (2010). doi:10.1103/PhysRevB.81.041406.

[126] W. Norimatsu and M. Kusunoki. *Formation process of graphene on SiC (0001)*. Phys. E Low-dimensional Syst. Nanostructures, **42** (4): 691–694 (2010). doi:10.1016/j.physe.2009.11.151.

[127] M. Huang, H. Yan, T. F. Heinz, and J. Hone. *Probing strain-induced electronic structure change in graphene by Raman spectroscopy.* Nano Lett., **10** (10): 4074–9 (2010). doi:10.1021/nl102123c.

[128] T. Schumann, K.-J. Friedland, M. H. Oliveira Jr., A. Tahraoui, J. M. J. Lopes, and H. Riechert. *Anisotropic quantum Hall effect in epitaxial graphene on stepped SiC surfaces*. Phys. Rev. B, **85** (23): 23502 (2012). doi:10.1103/PhysRevB.85.235402.

[129] Y. Zhang, Z. Jiang, J. P. Small, M. S. Purewal, Y.-W. Tan, M. Fazlollahi, J. D. Chudow, J. a. Jaszczak, H. L. Stormer, and P. Kim. *Landau-Level Splitting in Graphene in High Magnetic Fields*. Phys. Rev. Lett., **96** (13): 136806 (2006). doi:10.1103/PhysRevLett.96.136806.

[130] K. von Klitzing, G. Dorda, and M. Pepper. *New Method for High-Accuracy Determination of the Fine-Structure Constant Based on Quantized Hall Resistance*. Phys. Rev. Lett., **45** (6): 494–497 (1980). doi:10.1103/PhysRevLett.45.494.

[131] J. L. Tedesco, B. L. VanMil, R. L. Myers-Ward, J. M. McCrate, S. a. Kitt, P. M. Campbell, G. G. Jernigan, J. C. Culbertson, C. R. Eddy, and D. K. Gaskill. *Hall effect mobility of epitaxial graphene grown on silicon carbide*. Appl. Phys. Lett., **95** (12): 122102 (2009). doi:10.1063/1.3224887.

[132] J. Jobst, D. Waldmann, F. Speck, R. Hirner, D. K. Maude, T. Seyller, and H. B. Weber. *Transport properties of high-quality epitaxial graphene on 6H-SiC(0001)*. Solid State Commun., **151** (16): 1061–1064 (2011). doi:10.1016/j.ssc.2011.05.015.

[133] M. K. Yakes, D. Gunlycke, J. L. Tedesco, P. M. Campbell, R. L. Myers-Ward, C. R. Eddy, D. K. Gaskill, P. E. Sheehan, and A. R. Laracuente. *Conductance anisotropy in epitaxial graphene sheets generated by substrate interactions.* Nano Lett., **10** (5): 1559–62 (2010). doi:10.1021/nl9035302.

[134] S.-H. Ji, J. B. Hannon, R. M. Tromp, V. Perebeinos, J. Tersoff, and F. M. Ross. *Atomic-scale transport in epitaxial graphene*. Nat. Mater., **10** (11): 114 (2011). doi:10.1038/nmat3170.

[135] S. Pisana, M. Lazzeri, C. Casiraghi, K. S. Novoselov, A. K. Geim, A. C. Ferrari, and F. Mauri. *Breakdown of the adiabatic Born-Oppenheimer approximation in graphene.* Nat. Mater., **6** (3): 198–201 (2007). doi:10.1038/nmat1846.

[136] A. Das, S. Pisana, B. Chakraborty, S. Piscanec, S. K. Saha, U. V. Waghmare, K. S. Novoselov, H. R. Krishnamurthy, A. K. Geim, A. C. Ferrari, and A. K. Sood. *Monitoring dopants by Raman scattering in an electrochemically top-gated graphene transistor.* Nat. Nanotechnol., **3** (4): 210–215 (2008). doi:10.1038/nnano.2008.67.

[137] D. Schmidt, T. Ohta, and T. Beechem. *Strain and charge carrier coupling in epitaxial graphene*. Phys. Rev. B, **84** (23): 235422 (2011). doi:10.1103/PhysRevB.84.235422.

[138] T. Seyller, K. V. Emtsev, K. Gao, F. Speck, L. Ley, A. Tadich, L. Broekman, J. Riley, R. C. G. Leckey, and O. Rader. *Structural and electronic properties of graphite layers grown on SiC(0001)*. Surf. Sci., **600** (18): 3906–3911 (2006). doi:10.1016/j.susc.2006.01.102.

[139] M. Büttiker. *Absence of backscattering in the quantum Hall effect in multiprobe conductors.* Phys. Rev. B. Condens. Matter, **38** (14): 9375–9389 (1988).

[140] R. van Haren, F. A. P. Blom, W. de Lange, and J. H. Wolter. *Total suppression of the inter-edge-channel scattering in a GaAs/AlGaAs heterostructure*. Surf. Sci., **305** (1-3): 172–175 (1994). doi:10.1016/0039-6028(94)90880-X.

[141] R. Yang, Q. S. Huang, X. L. Chen, G. Y. Zhang, and H.-J. Gao. *Substrate doping effects on Raman spectrum of epitaxial graphene on SiC*. J. Appl. Phys., **107** (3): 034305 (2010). doi:10.1063/1.3283922.

[142] C. Beenakker. *Edge channels for the fractional quantum Hall effect*. Phys. Rev. Lett., **64** (2): 216–219 (1990). doi:10.1103/PhysRevLett.64.216.

[143] D. B. Chklovskii, B. I. Shklovskii, and L. I. Glazman. *Electrostatics of edge channels*. Phys. Rev. B, **46** (7): 4026–4034 (1992). doi:10.1103/PhysRevB.46.4026.

[144] A. Siddiki and R. Gerhardts. *Incompressible strips in dissipative Hall bars as origin of quantized Hall plateaus*. Phys. Rev. B, **70** (19): 195335 (2004). doi:10.1103/PhysRevB.70.195335.

[145] K.-J. Friedland, A. Siddiki, R. Hey, H. Kostial, A. Riedel, and D. Maude. *Quantum Hall effect in a high-mobility two-dimensional electron gas on the surface of a cylinder*. Phys. Rev. B, **79** (12): 125320 (2009). doi:10.1103/PhysRevB.79.125320.

[146] T. Löfwander, P. San-Jose, and E. Prada. *Quantum Hall effect in graphene with twisted bilayer stripe defects*. Phys. Rev. B, **87** (20): 205429 (2013). doi:10.1103/PhysRevB.87.205429.

[147] J. Zabel, R. R. Nair, A. Ott, T. Georgiou, A. K. Geim, K. S. Novoselov, and C. Casiraghi. *Raman spectroscopy of graphene and bilayer under biaxial strain: bubbles and balloons.* Nano Lett., **12** (2): 617–21 (2012). doi:10.1021/nl203359n.

[148] Sergey Stepanov. *http://sergey.gmca.aps.anl.gov/* (accessed 17 December 2013).

[149] D. Yoon, Y.-W. Son, and H. Cheong. *Negative thermal expansion coefficient of graphene measured by Raman spectroscopy.* Nano Lett., **11** (8): 3227–31 (2011). doi:10.1021/nl201488g.

[150] Z. Li and R. C. Bradt. *Thermal Expansion and Thermal Expansion Anisotropy of SiC Polytypes*. J. Am. Ceram. Soc., **70** (7): 445–448 (1987). doi:10.1111/j.1151-2916.1987.tb05673.x.

[151] X. Weng, J. A. Robinson, K. Trumbull, R. Cavalero, M. A. Fanton, and D. Snyder. *Structure of few-layer epitaxial graphene on 6H-SiC(0001) at atomic resolution*. Appl. Phys. Lett., **97** (20): 201905 (2010). doi:10.1063/1.3517505.

[152] J. Hass, F. Varchon, J. Millán-Otoya, M. Sprinkle, N. Sharma, W. A. de Heer, C. Berger, P. First, L. Magaud, and E. Conrad. *Why Multilayer Graphene on 4H-SiC(000$\bar{1}$) Behaves Like a Single Sheet of Graphene*. Phys. Rev. Lett., **100** (12): 3–6 (2008). doi:10.1103/PhysRevLett.100.125504.

[153] W. A. De Heer, C. Berger, M. Ruan, M. Sprinkle, X. Li, Y. Hu, B. Zhang, J. Hankinson, and E. Conrad. *Large area and structured epitaxial graphene produced by confinement controlled sublimation of silicon carbide.* Proc. Natl. Acad. Sci. U. S. A., **108** (41): 16900–5 (2011). doi:10.1073/pnas.1105113108.

[154] J. L. Tedesco, G. G. Jernigan, J. C. Culbertson, J. K. Hite, Y. Yang, K. M. Daniels, R. L. Myers-Ward, C. R. Eddy, J. A. Robinson, K. A. Trumbull, M. T. Wetherington, P. M. Campbell, and D. K. Gaskill. *Morphology characterization of argon-mediated epitaxial graphene on C-face SiC*. Appl. Phys. Lett., **96** (22): 222103 (2010). doi:10.1063/1.3442903.

[155] N. Luxmi, N. Srivastava, G. He, R. M. Feenstra, and P. Fisher. *Comparison of graphene formation on C-face and Si-face SiC {0001} surfaces*. Phys. Rev. B, **82** (23): 235406 (2010). doi:10.1103/PhysRevB.82.235406.

[156] C. Çelebi, C. Yanik, A. G. Demirkol, and I. I. Kaya. *Control of the graphene growth rate on capped SiC surface under strong Si confinement*. Appl. Surf. Sci., **264**: 56–60 (2013). doi:10.1016/j.apsusc.2012.09.103.

[157] G. K. H. Pang, K. Z. Baba-Kishi, and A. Patel. *Topographic and phase-contrast imaging in atomic force microscopy*. Ultramicroscopy, **81** (2): 35–40 (2000). doi:10.1016/S0304-3991(99)00164-3.

[158] P. N. First, W. A. de Heer, T. Seyller, C. Berger, J. A. Stroscio, and J. Moon. *Epitaxial Graphenes on Silicon Carbide*. MRS Bull., **35** (04): 296–305 (2011). doi:10.1557/mrs2010.552.

[159] C. Berger, Z. Song, X. Li, X. Wu, N. Brown, C. Naud, D. Mayou, T. Li, J. Hass, A. N. Marchenkov, E. H. Conrad, P. N. First, and W. a. de Heer. *Electronic confinement and coherence in patterned epitaxial graphene.* Science, **312** (5777): 1191–6 (2006). doi:10.1126/science.1125925.

[160] A. Koma. *Van der Waals epitaxy – a new epitaxial growth method for a highly lattice–mismatched system*. Thin Solid Films, **216** (1): 72–76 (1992). doi:10.1016/0040-6090(92)90872-9.

[161] F. Maeda and H. Hibino. *Molecular beam epitaxial growth of graphene and ridge-structure networks of graphene*. J. Phys. D. Appl. Phys., **44** (43): 435305 (2011). doi:10.1088/0022-3727/44/43/435305.

[162] F. Maeda and H. Hibino. *Thin Graphitic Structure Formation on Various Substrates by Gas-Source Molecular Beam Epitaxy Using Cracked Ethanol*. Jpn. J. Appl. Phys., **49** (4): 04DH13 (2010). doi:10.1143/JJAP.49.04DH13.

[163] S. K. Jerng, D. S. Yu, Y. S. Kim, J. Ryou, S. Hong, C. Kim, S. Yoon, D. K. Efetov, P. Kim, and S. H. Chun. *Nanocrystalline Graphite Growth on Sapphire by Carbon Molecular Beam Epitaxy*. J. Phys. Chem. C, **115** (11): 4491–4494 (2011). doi:10.1021/jp110650d.

[164] U. Wurstbauer, T. Schiros, C. Jaye, A. S. Plaut, R. He, A. Rigosi, C. Gutiérrez, D. Fischer, L. N. Pfeiffer, A. N. Pasupathy, A. Pinczuk, and J. M. Garcia. *Molecular beam growth of graphene nanocrystals on dielectric substrates*. Carbon, **50** (13): 4822–4829 (2012). doi:10.1016/j.carbon.2012.06.008.

[165] N. Ferralis, R. Maboudian, and C. Carraro. *Evidence of Structural Strain in Epitaxial Graphene Layers on 6H-SiC(0001)*. Phys. Rev. Lett., **101** (15): 156801 (2008). doi:10.1103/PhysRevLett.101.156801.

[166] G. A. Slack and S. F. Bartram. *Thermal expansion of some diamondlike crystals*. J. Appl. Phys., **46** (1): 89 (1975). doi:10.1063/1.321373.

[167] N. Mounet and N. Marzari. *First-principles determination of the structural, vibrational and thermodynamic properties of diamond, graphite, and derivatives*. Phys. Rev. B, **71** (20): 205214 (2005). doi:10.1103/PhysRevB.71.205214.

[168] L. Nemec, V. Blum, P. Rinke, and M. Scheffler. *Thermodynamic Equilibrium Conditions of Graphene Films on SiC*. Phys. Rev. Lett., **111** (6): 065502 (2013). doi:10.1103/PhysRevLett.111.065502.

[169] V. Blum, R. Gehrke, F. Hanke, P. Havu, V. Havu, X. Ren, K. Reuter, and M. Scheffler. *Ab initio molecular simulations with numeric atom-centered orbitals*. Comput. Phys. Commun., **180** (11): 2175–2196 (2009). doi:10.1016/j.cpc.2009.06.022.

[170] J. P. Perdew, K. Burke, and M. Ernzerhof. *Generalized Gradient Approximation Made Simple*. Phys. Rev. Lett., **77** (18): 3865–3868 (1996). doi:10.1103/PhysRevLett.77.3865.

[171] A. Tkatchenko and M. Scheffler. *Accurate Molecular Van Der Waals Interactions from Ground-State Electron Density and Free-Atom Reference Data*. Phys. Rev. Lett., **102** (7): 073005 (2009). doi:10.1103/PhysRevLett.102.073005.

[172] J. M. Carlsson. *Simulations of the Structural and Chemical Properties of nanoporous Carbon*. In L. Colombo and A. Fasolino, eds., *Computer-Based Modeling of Novel Carbon Systems and Their Properties*, pp. 79–128. Springer Science + Business Media B.V. (2010).

[173] E. J. G. Santos, S. Riikonen, D. Sánchez-Portal, and A. Ayuela. *Magnetism of Single Vacancies in Rippled Graphene*. J. Phys. Chem. C, **116** (13): 7602–7606 (2012). doi:10.1021/jp300861m.

[174] A. W. Robertson, B. Montanari, K. He, C. S. Allen, Y. A. Wu, N. M. Harrison, A. I. Kirkland, and J. H. Warner. *Structural reconstruction of the graphene monovacancy.* ACS Nano, **7** (5): 4495–502 (2013). doi:10.1021/nn401113r.

[175] J. Carlsson and M. Scheffler. *Structural, Electronic, and Chemical Properties of Nanoporous Carbon*. Phys. Rev. Lett., **96** (4): 046806 (2006). doi:10.1103/PhysRevLett.96.046806.

[176] M. M. Lucchese, F. Stavale, E. H. artins Ferreira, C. Vilani, M. V. O. Moutinho, R. B. Capaz, C. A. Achete, and A. Jorio. *Quantifying ion-induced defects and Raman relaxation length in graphene*. Carbon, **48** (5): 1592–1597 (2010). doi:10.1016/j.carbon.2009.12.057.

[177] W. J. Borer and H. H. Günthard. *Lattice Energy, Lattice Constant, and Thermodynamic Properties of γ-Al_2O_3*. Helv. Chim. Acta, **53** (5): 1043–1050 (1970). doi:10.1002/hlca.19700530518.

[178] A. C. Ferrari and J. Robertson. *Interpretation of Raman spectra of disordered and amorphous carbon*. Phys. Rev. B, **61** (20): 14095 (2000). doi:10.1103/PhysRevB.61.14095.

[179] Y. Baskin and L. Meyer. *Lattice Constants of Graphite at Low Temperatures*. Phys. Rev., **100** (2): 544–544 (1955). doi:10.1103/PhysRev.100.544.

[180] J. Borysiuk, R. Bożek, W. Strupiński, A. Wysmołek, K. Grodecki, R. Stępniewski, and J. M. Baranowski. *Transmission electron microscopy and scanning tunneling microscopy investigations of graphene on 4H-SiC(0001)*. J. Appl. Phys., **105** (2): 023503 (2009). doi:10.1063/1.3065481.

[181] J. Hass, R. Feng, J. Millán-Otoya, X. Li, M. Sprinkle, P. First, W. de Heer, E. Conrad, and C. Berger. *Structural properties of the multilayer graphene/4H-SiC(000$\bar{1}$) system as determined by surface x-ray diffraction*. Phys. Rev. B, **75** (21): 214109 (2007). doi:10.1103/PhysRevB.75.214109.

[182] F. Varchon, P. Mallet, J.-Y. Veuillen, and L. Magaud. *Ripples in epitaxial graphene on the Si-terminated SiC(0001) surface*. Phys. Rev. B, **77** (23): 235412 (2008). doi:10.1103/PhysRevB.77.235412.

[183] E. Lampin, C. Priester, C. Krzeminski, and L. Magaud. *Graphene buffer layer on Si-terminated SiC studied with an empirical interatomic potential*. J. Appl. Phys., **107** (10): 103514 (2010). doi:10.1063/1.3357297.

[184] N. Camara, B. Jouault, A. Caboni, B. Jabakhanji, W. Desrat, E. Pausas, C. Consejo, N. Mestres, P. Godignon, and J. Camassel. *Growth of monolayer graphene on 8° off-axis 4G-SiC (000-1) substrates with application to quantum transport devices*. Appl. Phys. Lett., **97** (9): 093107 (2010). doi:10.1063/1.3480610.

[185] F. Speck, J. Jobst, F. Fromm, M. Ostler, D. Waldmann, M. Hundhausen, H. B. Weber, and T. Seyller. *The quasi-free-standing nature of graphene on H-saturated SiC(0001)*. Appl. Phys. Lett., **99** (12): 122106 (2011). doi:10.1063/1.3643034.

[186] A. Mzerd, D. Sayah, G. Brun, J. C. Tedenac, and A. Boyer. *Crystal growth and sticking coefficient of Bi_2Te_3 thin films on Si (111) substrate*. J. Mater. Sci. Lett., **14**: 194–197 (1995).

[187] J. Zhao, Y. Zeng, C. Liu, and Y. Li. *Substrate temperature dependence of ZnTe epilayers grown on GaAs(001) by molecular beam epitaxy*. J. Cryst. Growth, **312** (9): 1491–1495 (2010). doi:10.1016/j.jcrysgro.2010.01.032.

[188] Y. Kangawa, T. Ito, A. Taguchi, K. Shiraishi, T. Irisawa, and T. Ohachi. *Monte Carlo simulation for temperature dependence of Ga diffusion length on GaAs(0 0 1)*. Appl. Surf. Sci., **190** (1-4): 517–520 (2002). doi:10.1016/S0169-4332(01)00930-8.

[189] H. Dürr, J. F. Wendelken, and J.-K. Zuo. *Island morphology and adatom energy barriers during homoepitaxy on Cu(001)*. Surf. Sci., **328** (1-2): L527–L532 (1995). doi:10.1016/0039-6028(95)00087-9.

[190] G. Haas, A. Menck, H. Brune, J. V. Barth, J. A. Venables, and K. Kern. *Nucleation and growth of supported clusters at defect sites: Pd/MgO(001)*. Phys. Rev. B, **61** (16): 11105–11108 (2000). doi:10.1103/PhysRevB.61.11105.

[191] J. A. Venables, G. D. T. Spiller, and M. Manbücken. *Nucleation and growth of thin films*. Reports Prog. Phys., **47**: 399–459 (1984).

[192] G. Lippert, J. Dabrowski, Y. Yamamoto, F. Herziger, J. Maultzsch, M. C. Lemme, W. Mehr, and G. Lupina. *Molecular beam growth of micrometer-size graphene on mica*. Carbon, **52**: 40–48 (2013). doi:10.1016/j.carbon.2012.09.001.

[193] H. Ibach and H. Lüth. In *Festkörperphysik*, chap. Hall-Effekt, pp. 450–451. Springer, Berlin, 6th ed. (2001).

List of Figures

List of Tables

Acknowledgments

The work for this thesis has been performed in the Department of Epitaxy at the Paul-Drude-Institut für Festkörperelektronik in Berlin.

I would like to express my gratitude to all the people who supported and guided me during the course of this thesis. In particular, I would like to thank:

Prof. Dr. Henning Riechert for giving me the opportunity to perform this work at the PDI.

Dr. J. Marcelo J. Lopes for receiving me in his team, the guidance he provided, the careful reading of the thesis draft, and for creating such a positive and productive working atmosphere.

Dr. Lutz Geelhaar for welcoming me in the epitaxy department.

Dr. Myriano H. Oliveira and Dr. Joseph M. Wofford for the great work we conducted together, for the corrections of my thesis draft, and for being friends.

Dr. Klaus-Jürgen Friedland for his assistance for conducting electrical transport measurements. He not only thought me how to operate the equipment, but only helped me to gain a deeper understanding of the quantum Hall effect.

Dr. Michael Hanke and Dr. Martin Dubslaff for the support during the measurements performed at the ESRF, and analyzing the results.

Dr. Manfred Ramsteiner for the help and introduction for Raman spectroscopy measurements.

Prof. Dr. Thomas Seyller and Felix Fromm (Technical University Chemnitz) for providing XPS measurements.

Prof. Dr. Volker Blum, Dr. Patrick Rincke, and Lydia Nemenc (Fritz-Haber-Institut Berlin) for providing DFT calculations and patiently explaining what these meant.

All my fellow students for the great atmosphere I got to enjoy, and the many scientific and non-scientific discussions during lunch and drinking espresso.

Claudia Herrmann, Michael Höricke, and Hans-Peter Schönherr for the technical support with the MBE machine.

Walid Anders, Bernd Drescher, Sander Rauwerdink, Angela Riedel, Werner Seidel, and Dr. Abbes Tahraoui for technical support with processing of my samples.

The administration of the PDI, who helped dealing with all the complicated bureaucracy.

All the colleagues who have not been named directly but helped me in different ways during my work at PDI.

Meine Familie, die mich immer unterstützt hat.

Selbständigkeitserklärung

Ich erkläre, dass ich die vorliegende Arbeit selbständig und nur unter Verwendung der angegebenen Literatur und Hilfsmittel angefertigt habe.

Berlin, den 28.02.2014 Timo Schumann